



All Theses and Dissertations

2011-07-15

Design and Analysis of a Flapping Wing Mechanism for Optimization

Ryan Brandon George
Brigham Young University - Provo

Follow this and additional works at: <https://scholarsarchive.byu.edu/etd>

 Part of the [Mechanical Engineering Commons](#)

BYU ScholarsArchive Citation

George, Ryan Brandon, "Design and Analysis of a Flapping Wing Mechanism for Optimization" (2011). *All Theses and Dissertations*. 2737.

<https://scholarsarchive.byu.edu/etd/2737>

This Thesis is brought to you for free and open access by BYU ScholarsArchive. It has been accepted for inclusion in All Theses and Dissertations by an authorized administrator of BYU ScholarsArchive. For more information, please contact scholarsarchive@byu.edu, ellen_amatangelo@byu.edu.

Design and Analysis of a Flapping Wing
Mechanism for Optimization

Ryan B. George

A thesis submitted to the faculty of
Brigham Young University
in partial fulfillment of the requirements for the degree of
Master of Science

Scott L. Thomson, Chair
Mark B. Colton
Christopher A. Mattson

Department of Mechanical Engineering
Brigham Young University
August 2011

Copyright © 2011 Ryan B. George
All Rights Reserved

ABSTRACT

Design and Analysis of a Flapping Wing Mechanism for Optimization

Ryan B. George
Department of Mechanical Engineering
Master of Science

Furthering our understanding of the physics of flapping flight has the potential to benefit the field of micro air vehicles. Advancements in micro air vehicles can benefit applications such as surveillance, reconnaissance, and search and rescue. In this research, flapping kinematics of a ladybug was explored using a direct linear transformation. A flapping mechanism design is presented that was capable of executing ladybug or other species-specific kinematics. The mechanism was based on a differential gear design, had two wings, and could flap in harsh environments. This mechanism served as a test bed for force analysis and optimization studies. The first study was based on a Box-Behnken screening design to explore wing kinematic parameter design space and manually search in the direction of flapping kinematics that optimized the objective of maximum combined lift and thrust. The second study used a Box-Behnken screening design to build a response surface. Using gradient-based techniques, this surface was optimized for maximum combined lift and thrust. Box-Behnken design coupled with response surface methodology was an efficient method for exploring the mechanism force response. Both methods for optimization were capable of successfully improving lift and thrust force outputs. The incorporation of the results of these studies will aid in the design of more efficient micro air vehicles and with the ultimate goal of leading to a better understanding of flapping wing aerodynamics and the development of aerodynamic models.

Keywords: flapping flight, flapping mechanism, ladybug, direct linear transformation, Box-Behnken, response surface optimization, flight, micro-air vehicle, biologically-inspired flight

ACKNOWLEDGMENTS

It was Dr. Scott Thomson who encouraged me to attend graduate school during my undergraduate career in an instrumentation class. I would not be capable of this work were it not for his hard work, knowledge, guidance, and support. He has worked hard for the success of this project and helped me every step of the way. I am a better person because of his example.

I wish to thank my graduate committee members, Dr. Mark Colton and Dr. Christopher Mattson. These members have given invaluable assistance and direction throughout the course of this research.

I also wish to thank Kevin Cole for his wealth of knowledge and help throughout the duration of this thesis in LabVIEW programming, and Mike Tree for his patience, skill, and assistance in solid modeling and manufacturing.

This work would not have been possible without the funding from the Air Force Office of Scientific Research, the support of the BYU department of Mechanical Engineering, the Rocky Mountain NASA Space Grant Consortium, and the Office of Research and Creative Activities (ORCA).

Lastly, I wish to thank my parents for being a pillar of light to me throughout my life, my Heavenly Father who provided comfort when I needed it most, but most importantly my wife, Katie, and son, Lucas, for their love and smiles throughout it all.

TABLE OF CONTENTS

LIST OF TABLES ix

LIST OF FIGURES xi

1 Introduction 1

1.1 Background and Motivation 2

1.1.1 Flapping Flight Aerodynamics..... 2

1.1.2 Previous Flapping Flight Research 2

1.1.3 Motivation..... 4

1.2 Thesis Overview 5

1.3 Thesis Outline 5

1.3.1 High-Speed Kinematic Quantification of Ladybugs (*Hippodamia Convergens*)
During Takeoff (Chapter 2) 5

1.3.2 Design of a Differential-Driven Flapping-Wing Mechanism for Force Analysis
and Optimization (Chapter 3) 6

1.3.3 Kinematic Optimization of a Flapping-Wing Model Using Box-Behnken
Screening Design and Response Surface Methodology (Chapter 4) 6

**2 High-Speed Kinematic Quantification of Ladybugs (*Hippodamia Convergens*)
During Takeoff 9**

2.1 Introduction..... 9

2.2 Methods 10

2.2.1 Overview..... 10

2.2.2 Data Acquisition 10

2.2.3 Data Analysis 12

2.3 Results..... 16

2.3.1 Ladybug Kinematic Results 16

2.3.2 Uncertainty of Measurements 21

2.4	Conclusion	23
3	Design of a Differential-Driven Flapping-Wing Mechanism for Force Analysis and Optimization	25
3.1	Introduction.....	25
3.1.1	Background.....	25
3.1.2	Related Work	26
3.2	System Design	28
3.2.1	Mechanism Design.....	29
3.2.2	Actuation and Control.....	32
3.2.3	Instrumentation	33
3.3	Methods	35
3.3.1	Wing Trajectories.....	35
3.3.2	Optimization Approach.....	38
3.4	Results.....	39
3.4.1	Mechanism Response.....	39
3.4.2	Lift and Thrust Production.....	40
3.4.3	Force Uncertainty.....	47
3.5	Conclusions.....	48
4	Kinematic Optimization of a Flapping Wing Model Using Box-Behnken Screening Design and Response Surface Methodology	51
4.1	Introduction.....	51
4.2	Methods	52
4.2.1	Box-Behnken Screening Design.....	52
4.2.2	Response Surface Optimization	54
4.3	Results.....	57
4.3.1	Box-Behnken Screening Design.....	57

4.3.2	Response Surface Optimization	63
4.4	Conclusion	71
5	Conclusions	73
5.1	High-Speed Kinematic Quantification of Ladybugs (<i>Hippodamia Convergens</i>) During Takeoff	73
5.1.1	Conclusions	73
5.1.2	Future Work	74
5.2	Design of a Differential-Driven Flapping-Wing Mechanism for Force Analysis and Optimization	74
5.2.1	Conclusions	74
5.2.2	Future Work	75
5.3	Kinematic Optimization of a Flapping Wing Model Using Box-Behnken Screening Design and Response Surface Methodology	75
5.3.1	Conclusions	75
5.3.2	Future Work	76
5.4	Additional Work	76
	References	79
	Appendix A. Ladybug DLT Files - MATLAB	87
A.1	Calibration	88
A.2	Tracking Analysis	92
	Appendix B. Flapping Mechanism Drawing Package	95
B.1	Drawing Package	96
B.2	Tolerance Analysis	119
	Appendix C. Flapping Mechanism Force Analysis – MATLAB	123
C.1	Box-Behnken Analysis	124
C.2	Mathscript Node for Generating Trajectories	127

C.3 Transform Forces	130
C.4 Response Surface Optimization	131
C.5 Response Surface Constraints	133
C.6 Response Surface Fitness Function.....	135
C.6 Response Surface Creation	136

LIST OF TABLES

Table 2-1. Frequency of ladybug flapping.....	18
Table 2-2. Uncertainty table due to mis-selection of key-points.	23
Table 3-1. List of flapping flight mechanisms and their function. List is organized chronologically, by date, and then alphabetically, by author.	26
Table 3-2. Step size for Box-Behnken testing and trajectories for runs labeled in Figure 3-9. Bolded values indicate a deviation from the starting trajectory (A).	41
Table 4-1. Kinematic coefficients for the starting point and the best runs of each iteration using arbitrary starting point kinematics. Bolded numbers represent an update in the kinematic coefficient from the optimization.	59
Table 4-2. Step size progression of the Box-Behnken optimization for each iteration.	59
Table 4-3. Kinematic coefficients for the starting point and best runs of each iteration using zebra finch starting point kinematics. Bolded numbers represent an update in the kinematic coefficient from the optimization.	62
Table 4-4. Kinematic coefficients for the starting trajectory and best runs from gradient-based optimization using an arbitrary starting point.	66
Table 4-5. Kinematic coefficients for the starting trajectory and best runs from gradient-based optimization using simplified zebra finch kinematics.	69
Table 4-6. Resulting forces summary for all four optimizations.	70

LIST OF FIGURES

Figure 2-1. High-speed imaging setup.....	11
Figure 2-2. Calibration target as viewed using setup shown in Figure 2-1.	12
Figure 2-3. Image sequence showing first (top) and last (bottom) frame with coordinate system.	16
Figure 2-4. Symbols showing three-dimensional paths of six ladybug anatomical landmarks. The dashed black lines connect the front and rear body points, illustrating the approximate ladybug body attitude, at select times.	17
Figure 2-5. Hindwing elevation (z) vs. time.	17
Figure 2-6. Body distance from origin vs. time, along with linear curve fit to estimate average velocity.....	18
Figure 2-7. Image sequence showing hindwing deformation.....	19
Figure 2-8. Ladybug hindwing amplitude.	19
Figure 2-9. Vertical (z) position of forewing and hindwing.	20
Figure 2-10. Ladybug forewing path during opening.....	20
Figure 2-11. Image sequence showing ladybug leg extension.	21
Figure 2-12. Actual location of calibration points plotted with their calculated location using DLT analysis.....	22
Figure 3-1. Coordinate definitions of the flapping wing mechanism.	29
Figure 3-2. Differential housed inside of a frame. The frame is supported from above and the wing attaches to the output of the differential.	30
Figure 3-3. Worm gears located directly behind the two differential inputs for compact design.....	31
Figure 3-4. Motors mounted to the top of the mechanism about a turntable for θ_1 rotation.	31
Figure 3-5. Strain gages fixed to a wing mounting bracket.....	35
Figure 3-6. Mechanism response for all DOFs using a swept sine (0-5 Hz) input.....	39
Figure 3-7. Tracking results of an arbitrary flapping trajectory.	40
Figure 3-8. Ladybug wing and outline used for acrylic wing fabrication.	41

Figure 3-9. Lift and thrust values averaged from two identical Box-Behnken iterations (432 runs performed twice). The dashed line represents the direction of the desired force.	42
Figure 3-10. Force and trajectory history for (A) starting trajectory.....	42
Figure 3-11. Force and trajectory history for (B) max thrust, no lift.....	43
Figure 3-12. Force and trajectory history for (C) max lift, no thrust.....	43
Figure 3-13. Force and trajectory history for (D) best run.	44
Figure 3-14. Force magnitude outputs compared over two iterations.	45
Figure 3-15. Force output for an arbitrary flapping trajectory performed 24 times.	46
Figure 3-16. Ensemble-averaged force output, along with standard deviation, of 24 runs.	46
Figure 3-17. Filtered and unfiltered force output for an arbitrary flapping trajectory.....	47
Figure 4-1. A central composite design tests the extremes of the system where a Box-Behnken design only tests the edges.....	52
Figure 4-2. Flowchart describing the Box-Behnken design optimization strategy.	54
Figure 4-3. Flowchart of the Box-Behnken response surface optimization method.	56
Figure 4-4. Box-Behnken design iteration performed five times starting from an arbitrary flapping trajectory.....	58
Figure 4-5. Progression of Box-Behnken design optimization starting from an arbitrary flapping trajectory.....	58
Figure 4-6. Force history of best run from Box-Behnken design starting from an arbitrary flapping trajectory.....	60
Figure 4-7. Box-Behnken design iteration performed four times starting from simplified zebra finch flapping kinematics.....	61
Figure 4-8. Progression of Box-Behnken design optimization starting from simplified zebra finch flapping kinematics.....	62
Figure 4-9. Force history of best run from Box-Behnken design starting from simplified zebra finch kinematics.	63
Figure 4-10. Lift and thrust forces for all runs from the response surface optimization using an arbitrary starting trajectory. Dashed line indicates search direction.	64
Figure 4-11. Experimental and analytical Pareto front shown for (a) iteration 1 and (b) iteration 2. Dashed line indicates search direction.....	65

Figure 4-12. Best runs from gradient-based optimization starting from an arbitrary flapping trajectory. Dashed line indicates search direction.....65

Figure 4-13. Force history from best run of response surface optimization starting from arbitrary flapping kinematics.67

Figure 4-14. Lift and thrust forces for all runs from the response surface optimization using simplified zebra finch kinematics. Dashed line indicates the search direction.....68

Figure 4-15. Experimental and analytical Pareto front shown for (a) iteration 1, (b) iteration 2, and (c) iteration 3. Dashed line indicates search direction.68

Figure 4-16. Best runs from gradient-based optimization starting from simplified zebra finch kinematics. Dashed line indicates search direction.....69

Figure 4-17. Force history from best run of response surface optimization using simplified zebra finch kinematics.70

1 INTRODUCTION

With almost a million different species of winged insects and over 10,000 flying birds and bats, nature's fliers are found all around us [1]. According to classical predictions based on steady-state aerodynamic analysis used for conventional fixed-wing flight, these species should not be able to produce sufficient lift to fly [2], [3]; rather, unsteady aerodynamic flapping-generated forces provide the necessary lift enhancement.

Until recently, research in the field of flapping flight has been somewhat hindered due to a lack of investigative tools (e.g. particle image velocimetry, computational fluid dynamics, real-time operating systems, etc.) [4]. With the introduction of these investigative tools and the associated advances in understanding of flapping flight physics, interest has emerged in the development of flapping aerial robots capable of navigating inside buildings or in confined spaces. Aerial robots of this type are classified as micro-air vehicles (MAVs) [5].

MAVs are generally defined as flying vehicles approximately 15 cm or less in height, length, and width [6], [7]. Flapping wing MAVs offer the potential for decreased detectability (due to reduced size and possibly reduced noise) and the ability to hover. Because of this, applications for MAVs are wide-ranging and include surveillance, reconnaissance [6], or even search and rescue [2].

This thesis aims to contribute to improved understanding of flapping flight through the development of a flapping wing mechanism and experimental-based optimization of the wing kinematics for optimal aerodynamic forces produced.

1.1 Background and Motivation

1.1.1 Flapping Flight Aerodynamics

Flapping flight has the potential to benefit MAV technology as it may provide improved aerodynamic performance over that of flight using conventional wings or rotors [8]. Two particular lift-generating mechanisms of flapping flight have been identified in nature that hold promise for MAV design. The first is the clap-and-fling mechanism at the top (and sometimes bottom) of the flapping stroke. During the clap-and-fling the two wings clap together and fling apart, creating a strong low-pressure zone between wings [5]. The second is the leading-edge vortex (LEV) created by dynamic stall during flapping [5]. These lift generating mechanisms are the basis for augmented lift and thrust production in flapping flight.

1.1.2 Previous Flapping Flight Research

Many areas of flapping flight research are currently being explored. Specific areas of interest include flight performance of various species, kinematic wing and body motion quantification of various species, lift and thrust estimates, wing-wing interactions, wing-wake interactions, the role of LEV attachment, biological considerations for MAV design, computational flapping models, experimental flapping model design, flow visualization, and computational and experimental model force optimization. In this thesis, the areas of kinematic quantification of wing and body motion, experimental flapping model design, and experimental force optimization are explored. The following is a brief overview of these areas of research. More in-depth discussions of previous work are provided in each of Chapters 2 through 4.

Kinematic Quantification of Wing and Body Motion

Large flapping variability exists among both insects and birds. Due to the large range of wing kinematics and other flapping variables, relatively few models (graphical, mathematical, etc.) describing wing motion exist. Although several models exist for such species as the fruit fly [9], [10], hoverfly [11], dragonfly [12], [13], and bat [14], [15], there still remains a large number of species yet to be explored. These models have brought to light complex kinematics involved in free flight and hovering. Further, these models have aided in the development of experimental and computational aerodynamic models of flapping flight [16], [17], [18], and yielded insight into physical phenomena such as wing-wing and wing-wake interactions [19], [20].

Flapping Mechanism Design

Flapping-wing mechanism design is fundamental in providing a test bed for wing kinematic optimization and force analysis. It is often difficult to emulate common flapping frequencies found in nature (25-200 Hz) [1]. Reynolds and Strouhal numbers (two non-dimensional numbers used for scaling, see Section 3.3.1) are commonly used to non-dimensionalize flapping aerodynamics and adjust the flapping frequency. In general, these flapping systems are fixed and are used to measure lift and drag forces or perform flow visualization. Several models do exist that are capable of untethered flight. These models can be classified into two main categories: adjustable and non-adjustable wing kinematics. A thorough summary of flapping wing models is given in Section 3.1.2.

Flapping Force Optimization

Research has been performed to optimize the design of a flapping wing mechanism used to match a predetermined kinematic trajectory. Bai et al. [21] optimized a MAV's flapping motion based on a fruit fly. This study matched the fruit fly kinematics while weakening the aerodynamic disadvantages during the upstroke. Few studies, however, have involved optimization using adjustable kinematics. Thomson et al. [22] used hardware-in-the-loop methodology to optimize the flapping kinematics of a 3-DOF flapping mechanism. This study used a single wing and only observed lift. Measurements from this study were subject to noise, causing uncertainty in gradient predictions when performing optimization. Boria et al. [23] used hardware-in-the-loop coupled with a genetic algorithm to overcome some of the difficulties observed in experimental measurements. Although less sensitive to noise, the genetic algorithm still had complications seeking convergence. Bandyopadhyay et al. [24] used hardware-in-the-loop methodology to optimize forces of a flapping fin. A simulated annealing term with a gradually reducing 'temperature' was used to prevent the algorithm from converging on anomalous local minima due to noise in the measurements.

1.1.3 Motivation

Many aspects of flapping flight aerodynamics, both in natural and man-made systems, are yet to be fully understood. Such aspects include: (1) phenomena due to deformable and/or adjustable wings and wing kinematics, (2) the wide variability in wing size, wing shape, and wing and body kinematics, (3) the optimization of wing kinematics for use in man-made systems, and (4) the use of LEV and clap-and-fling in a flapping mechanism. The study of these

and other similar understudied phenomena associated with flapping flight has the potential to benefit the development of MAV technology.

1.2 Thesis Overview

The purpose of this work was to contribute to the field of flapping flight research by studying wing kinematics of ladybugs during takeoff and then fabricating and testing an analogous flapping wing mechanism for force analysis and optimization. The mechanism included two wings, each with three independent rotational degrees of freedom (DOF) and fully adjustable kinematics. Optimization approaches included a Box-Behnken screening design and a response surface model coupled with a gradient-based approach.

1.3 Thesis Outline

This thesis is divided into three sections:

- 1) Kinematic quantification of ladybugs during takeoff (Chapter 2).
- 2) Design and modeling of an adjustable kinematic flapping-wing mechanism (Chapter 3).
- 3) Optimization of wing kinematics for maximum lift and thrust production using experimental, gradient-based optimization methods (Chapter 4).

1.3.1 High-Speed Kinematic Quantification of Ladybugs (*Hippodamia Convergens*) During Takeoff (Chapter 2)

The flapping-wing kinematics of ladybugs (*Hippodamia convergens*) during takeoff were analyzed using high-speed, stereoscopic imaging. A direct linear transformation was applied to transform two-dimensional stereoscopic image coordinates of key-point locations into three-

dimensional, Cartesian, spatial coordinates [25], [26]. These key-point locations included both forewing and hindwing wing-tips, the head, and the rear of the ladybug. A graphical kinematic representation of the ladybugs was created using the Cartesian coordinates acquired from the key-point locations of the ladybug. A graphical representation of the forewing endpoints during opening (before takeoff) was also created using the same procedure.

1.3.2 Design of a Differential-Driven Flapping-Wing Mechanism for Force Analysis and Optimization (Chapter 3)

The design of a robotic flapping-wing mechanism is discussed. The design allowed for dynamic adjustment of flapping trajectory with three rotational degrees of freedom, while keeping all motors and encoders out of the liquid (i.e., water or oil) to protect critical equipment from potential failure and increase reliability. Mechanism control is discussed. Preliminary exploration using a Box-Behnken design approach was used and showed successful parameter exploration of lift and thrust. Mechanism limitations are addressed.

1.3.3 Kinematic Optimization of a Flapping-Wing Model Using Box-Behnken Screening Design and Response Surface Methodology (Chapter 4)

Although kinematic models for flapping flight may be an optimal solution for nature's fliers, they may not necessarily be optimal for micro air vehicles. In this chapter, the kinematics of the flapping-wing mechanism were optimized with the objective of producing maximum combined lift and thrust. This was performed using two approaches. This first was by using a Box-Behnken screening design as an iterative technique in optimization (similar to a brute force method). The second used the Box-Behnken design to build a response surface. Then, using gradient-based optimization techniques, an optimal flapping trajectory from the surface was

found. This response surface methodology was repeated similarly to the former method optimization, but converged more quickly to an optimal solution.

2 HIGH-SPEED KINEMATIC QUANTIFICATION OF LADYBUGS (*HIPPODAMIA CONVERGENS*) DURING TAKEOFF

Ladybug wing and body kinematics during takeoff were explored using high-speed stereoscopic images acquired at a rate of 3000 frames per second. A direct linear transformation algorithm was used to quantify positions of selected locations on the body, forewings, and hindwings. In this chapter, design and setup of instrumentation and analysis procedures are explained. Other findings such as ladybug flapping frequency and motion of the forewing are also discussed.

2.1 Introduction

The use of flapping flight is ubiquitous among the animal and insect kingdom [1]. Flapping flight, which features an aerodynamic flight regime characterized by a relatively low Reynolds number, yields lift-generating mechanisms. It introduces several advantages such as increased agility and ability to navigate in confined spaces (such as indoors). It also offers the potential for decreased detectability, due to reduced size and possible reduced noise, and the ability to hover.

Many aspects of insect flight are not yet fully understood. Several of these aspects include lift generation associated with deformable or adjustable wings and wing kinematics, and the large variation found in wing size and shape. One particular aspect of interest is the influence of the forewings found in beetles (*Coleoptera*). Flying beetles such as ladybugs

(*Hippodamia convergens*) have two stiff, protective forewings and two flapping hindwings. The forewings cover the hindwings when not in flight, but move upward and forward during flight. They also perform other functions such as trapping moisture and providing protection [27]. The role of the forewing during flight has not been thoroughly explored, nor have the wing kinematics and aerodynamics of the forewing-hindwing combination.

The goal of this research was to analyze beetle flapping wing kinematics using ladybugs as subjects. A series of high-speed images of a ladybug during takeoff was analyzed to quantify the time-dependent, three-dimensional position of points on the body, forewings, and hindwings. This was done to quantify forewing opening, hindwing motion during flapping, and body motion during takeoff.

2.2 Methods

2.2.1 Overview

The approach used in this research was to analyze flapping wing kinematics of ladybugs using high-speed stereoscopic imaging. A direct linear transformation (DLT) was applied in order to convert the two-dimensional stereoscopic image coordinates into three-dimensional Cartesian spatial coordinates. These data were displayed using appropriate graphical kinematic representations for use in investigating the motion of the forewing in flapping flight and to study the deformable wing kinematics of ladybugs.

2.2.2 Data Acquisition

As illustrated in Figure 2-1, the experimental setup involved a Photron APX-RS high-speed digital camera, a mirror arrangement for projecting two views of an object onto a single

camera image, and a combination of LED (Visual Instrumentation Corporation 900415) and incandescent lighting (Lowel Light Photo Engineering Quartz D). The frame rate of the camera was set to 3000 frames per second while the shutter speed was $1/6000^{\text{th}}$ of a second. This higher shutter speed ensured a relatively complete freeze of the wing motion. A Nikon 105 mm Nikkor lens was used with an aperture of F11.

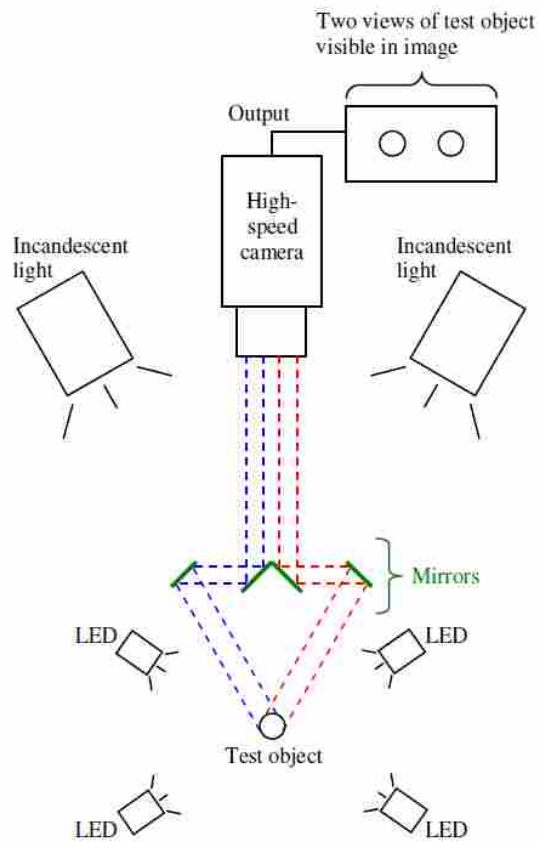


Figure 2-1. High-speed imaging setup.

Prior to image acquisition, a calibration target was created using 1.5 mm diameter extruded wire soldered together to form a grid pattern. The target consisted of 5 tiers with 25 white dots painted on each tier, providing a total of 125 calibration points. The target was placed

in the camera's field of view, so that two views of the target were visible in the camera image (see Figure 2-2).

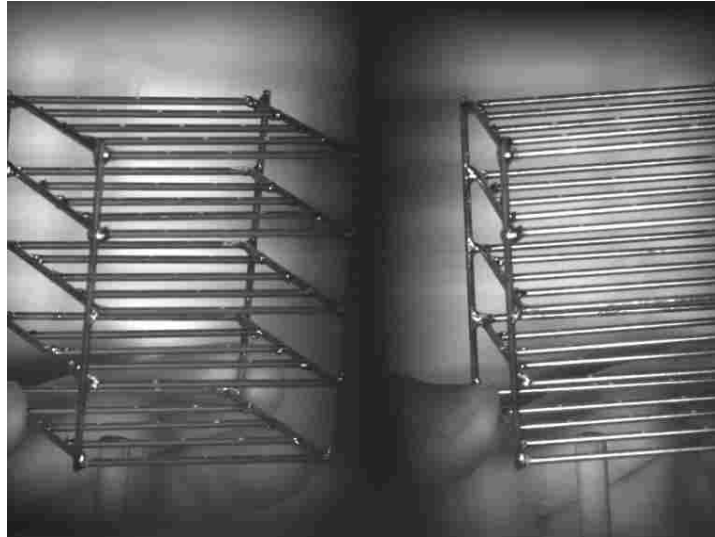


Figure 2-2. Calibration target as viewed using setup shown in Figure 2-1.

2.2.3 Data Analysis

A DLT implementation, custom coded in MATLAB, was used to analyze high-speed images. The DLT is here briefly described; further details can be found elsewhere [25], [26].

DLT is a method of determining the three-dimensional location of an object (or points on an object) in space using two different views of the object. There are a variety of ways of attaining multiple images; however, the approach used here was one camera and an arrangement of mirrors. This allowed for the relative distances between the camera, mirrors, and object to be varied over a sufficiently wide range. This method was also beneficial since it required only a single camera and required no temporal synchronization between sets of images.

Calibration was found using 100 visible calibration points on the aforementioned calibration target. Calibration consisted of finding vectors \mathbf{L} and \mathbf{R} using the following series of equations. First, \mathbf{L} (L_1 through L_{11}) was calculated using the system of equations

$$\begin{bmatrix} x_1 & y_1 & z_1 & 1 & 0 & 0 & 0 & 0 & -u_{L1}x_1 & -u_{L1}y_1 & -u_{L1}z_1 \\ 0 & 0 & 0 & 0 & x_1 & y_1 & z_1 & 1 & -v_{L1}x_1 & -v_{L1}y_1 & -v_{L1}z_1 \\ x_2 & y_2 & z_2 & 1 & 0 & 0 & 0 & 0 & -u_{L2}x_2 & -u_{L2}y_2 & -u_{L2}z_2 \\ 0 & 0 & 0 & 0 & x_2 & y_2 & z_2 & 1 & -v_{L2}x_2 & -v_{L2}y_2 & -v_{L2}z_2 \\ & & & & & & \vdots & & & & & \\ x_N & y_N & z_N & 1 & 0 & 0 & 0 & 0 & -u_{LN}x_N & -u_{LN}y_N & -u_{LN}z_N \\ 0 & 0 & 0 & 0 & x_N & y_N & z_N & 1 & -v_{LN}x_N & -v_{LN}y_N & -v_{LN}z_N \end{bmatrix} \begin{bmatrix} L_1 \\ L_2 \\ L_3 \\ L_4 \\ L_5 \\ L_6 \\ L_7 \\ L_8 \\ L_9 \\ L_{10} \\ L_{11} \end{bmatrix} = \begin{bmatrix} u_{L1} \\ v_{L1} \\ u_{L2} \\ v_{L2} \\ \vdots \\ u_{LN} \\ v_{LN} \end{bmatrix}, \quad (2-1)$$

where N is the number of calibration points, x_i , y_i , and z_i ($i = 1$ to N) are the known positions of the calibration points, u_{Li} and v_{Li} are the horizontal and vertical pixel locations, respectively, of the points in the images, and L_i through L_{11} are the calibration constants. Similarly, \mathbf{R} (R_1 through R_{11}) was found by replacing u_{Li} , v_{Li} , and L with u_{Ri} , v_{Ri} , and \mathbf{R} . If the first matrix on the left-hand side of Equation (2-1) is denoted as \mathbf{F}_L and the right-hand side matrix as \mathbf{g}_L , then using the Moore-Penrose pseudo-inverse method,

$$\mathbf{L} = (\mathbf{F}_L^T \mathbf{F}_L)^{-1} \mathbf{F}_L^T \mathbf{g}_L, \quad (2-2)$$

and similarly for \mathbf{R}

$$\mathbf{R} = (\mathbf{F}_R^T \mathbf{F}_R)^{-1} \mathbf{F}_R^T \mathbf{g}_R. \quad (2-3)$$

The position of any point visible from two perspectives in the image was then found using the equation

$$\begin{bmatrix} L_1 - L_9 u_L & L_2 - L_{10} u_L & L_3 - L_{11} u_L \\ L_5 - L_9 v_L & L_6 - L_{10} v_L & L_7 - L_{11} v_L \\ R_1 - R_9 u_R & R_2 - R_{10} u_R & R_3 - R_{11} u_R \\ R_5 - R_9 v_R & R_6 - R_{10} v_R & R_7 - R_{11} v_R \end{bmatrix} \begin{bmatrix} x \\ y \\ z \end{bmatrix} = \begin{bmatrix} u_L - L_4 \\ v_L - L_8 \\ u_R - R_4 \\ v_R - R_8 \end{bmatrix}. \quad (2-4)$$

Denoting the first matrix on the left-hand side as \mathbf{Q} and the right-hand side matrix as \mathbf{q} ,

Equation (2-4) can be written as

$$\mathbf{Q} \begin{bmatrix} x \\ y \\ z \end{bmatrix} = \mathbf{q}, \quad (2-5)$$

from which the Moore-Penrose pseudo-inverse method can be applied to find the position of the unknown Cartesian coordinates x , y , and z :

$$\begin{bmatrix} x \\ y \\ z \end{bmatrix} = (\mathbf{Q}^T \mathbf{Q})^{-1} \mathbf{Q}^T \mathbf{q}. \quad (2-6)$$

The \mathbf{L} and \mathbf{R} calibration matrices were found using the calibration target. A ladybug was then placed in the field of view and images of the ladybug were acquired during takeoff. The x , y , and z locations of six points on the ladybug were then tracked. The points include a point near the front of the body, a point near the rear of the body, and the tip of both forewings and hindwings.

Once 3D Cartesian spatial coordinates were found, the coordinates were rotated and translated to align with the x , y , and z axes. This was accomplished via use of a transformation matrix (\mathbf{H}) which defines both an x , y , z translation (\mathbf{p}) and a 3-2-1 Euler angle rotation (\mathbf{T}). A rotation by θ_z in the z -axis, a rotation by θ_y in the y -axis and a rotation by θ_x in the x -axis, respectively, was represented by

$$\mathbf{T}(\theta_z, \theta_y, \theta_x) = \begin{bmatrix} 1 & 0 & 0 \\ 0 & \cos \theta_x & \sin \theta_x \\ 0 & -\sin \theta_x & \cos \theta_x \end{bmatrix} \begin{bmatrix} \cos \theta_y & 0 & -\sin \theta_y \\ 0 & 1 & 0 \\ \sin \theta_y & 0 & \cos \theta_y \end{bmatrix} \begin{bmatrix} \cos \theta_z & \sin \theta_z & 0 \\ -\sin \theta_z & \cos \theta_z & 0 \\ 0 & 0 & 1 \end{bmatrix}. \quad (2-7)$$

The translation was represented by

$$\mathbf{p} = \begin{bmatrix} x_{trans} \\ y_{trans} \\ z_{trans} \end{bmatrix}, \quad (2-8)$$

where x_{trans} , y_{trans} , z_{trans} is the vector representing the translation from the origin of the initial frame to the origin of the new relative frame. The combined transformation matrix is represented by

$$\mathbf{H} = \begin{bmatrix} \mathbf{T}^T & \mathbf{p} \\ (3 \times 3) & (3 \times 1) \\ 0 & 0 & 0 & 1 \end{bmatrix}. \quad (2-9)$$

Transformation matrix \mathbf{H} when matrix multiplied with the 3D Cartesian coordinate, results in the new resolved Cartesian coordinate

$$[x_{new}, y_{new}, z_{new}, 1] = \mathbf{H} \begin{bmatrix} x_{old} \\ y_{old} \\ z_{old} \\ 1 \end{bmatrix}. \quad (2-10)$$

Each data set was rotated manually using its own transformation matrix to allow analysis of flapping wing and body kinematics relative to an inertial frame.

2.3 Results

2.3.1 Ladybug Kinematic Results

DLT analysis was performed on 298 frames of data. In each data frame, both forewings, both hindwings, the front body, and rear body were quantified. Figure 2-3 shows two images of the ladybug; one shortly after takeoff initiation, and another a short time later. These images show the coordinate system used.

Figure 2-4 shows the time history of the positions of the six points on the ladybug during takeoff. This demonstrates successful implementation of image analysis on the ladybug specimen. The forewing can be seen to have moved in unison with the hindwing and with a relatively large amplitude. This may be a passive reflex, although further investigation will be required to determine this.

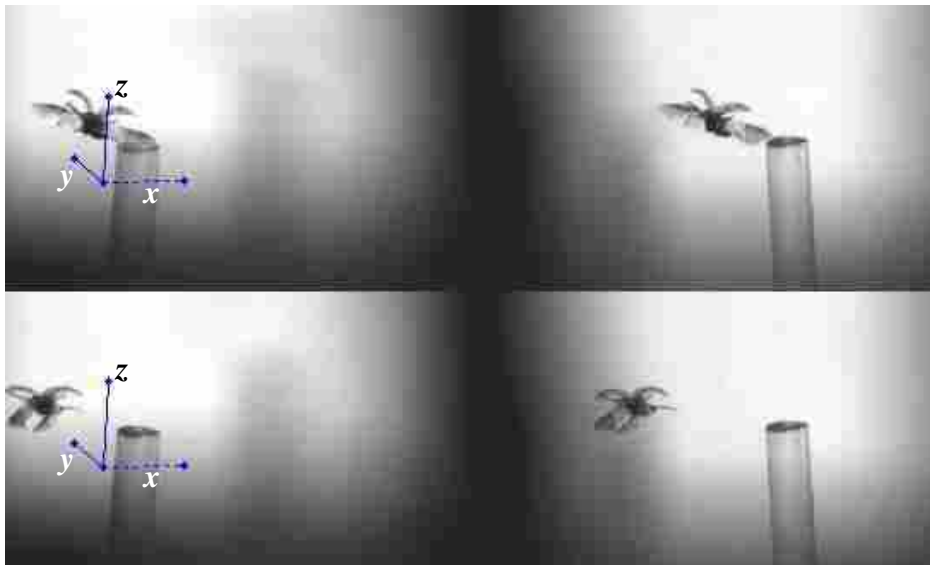


Figure 2-3. Image sequence showing first (top) and last (bottom) frame with coordinate system.

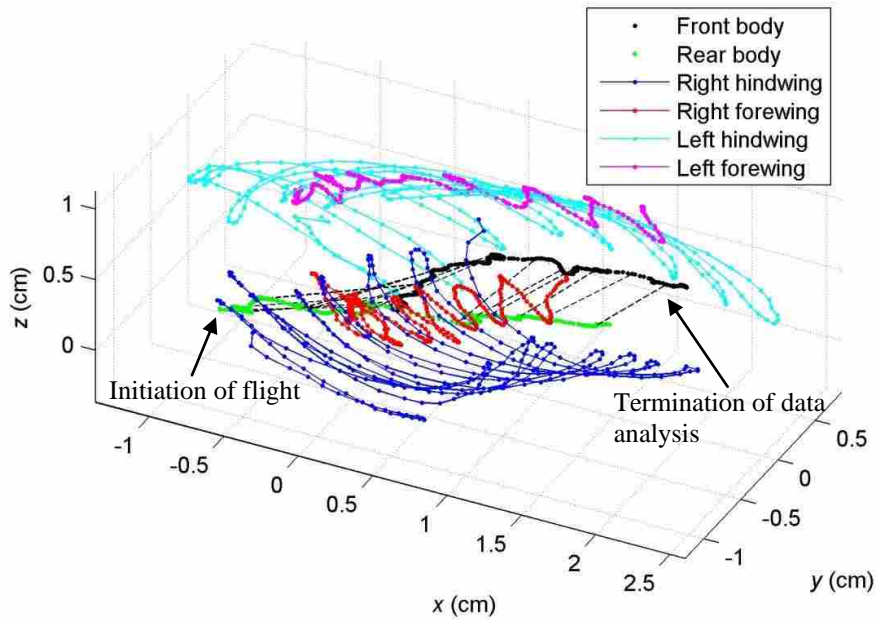


Figure 2-4. Symbols showing three-dimensional paths of six ladybug anatomical landmarks. The dashed black lines connect the front and rear body points, illustrating the approximate ladybug body attitude, at select times.

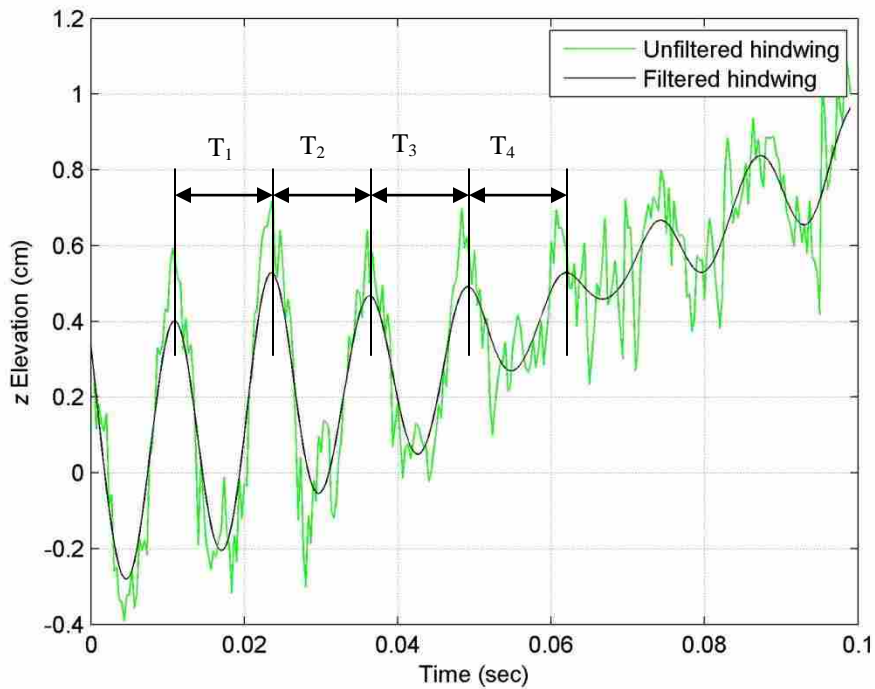


Figure 2-5. Hindwing elevation (z) vs. time.

Table 2-1. Frequency of ladybug flapping.

Period	Time (Seconds)	Frequency (Hz)
T ₁	0.01267	78.9
T ₂	0.01233	81.1
T ₃	0.01367	73.2
T ₄	0.01233	81.1
Average Frequency		78.6

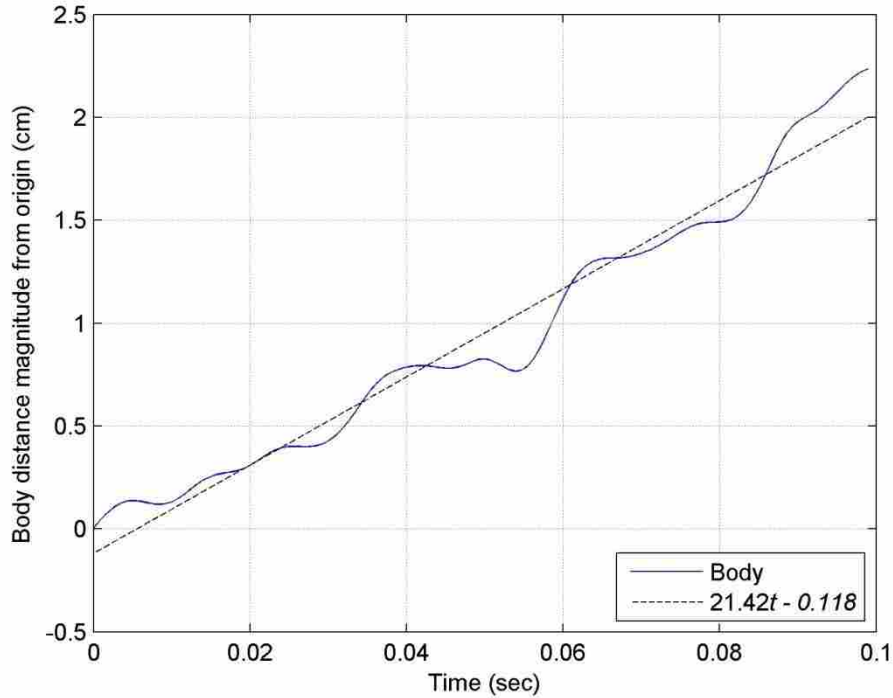


Figure 2-6. Body distance from origin vs. time, along with linear curve fit to estimate average velocity.

Figure 2-5 shows the hindwing elevation (z -position) vs. time. The average flapping frequency was 78.6 Hz (see Table 2-1). Figure 2-6 shows results from an analytical analysis of body velocity. Results indicate that the specimen was traveling at an average velocity of about 21.4 cm/s.

Figure 2-7 displays a sequence of images which help visualize the flexible nature of the hindwing. Wing rotation and deformation is evident, as has been observed elsewhere [10], [28];

this allows the airfoil shape of the wing to produce lift over the bulk of the insect's flapping period and contributes to other lift-enhancing phenomena.

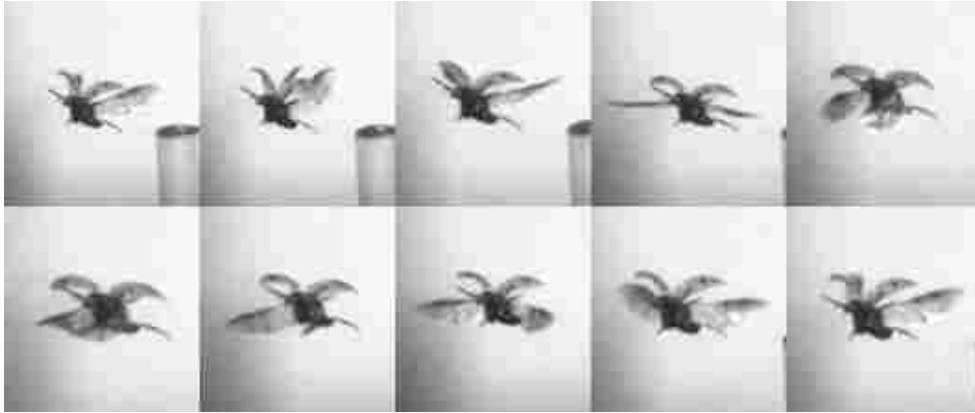


Figure 2-7. Image sequence showing hindwing deformation.

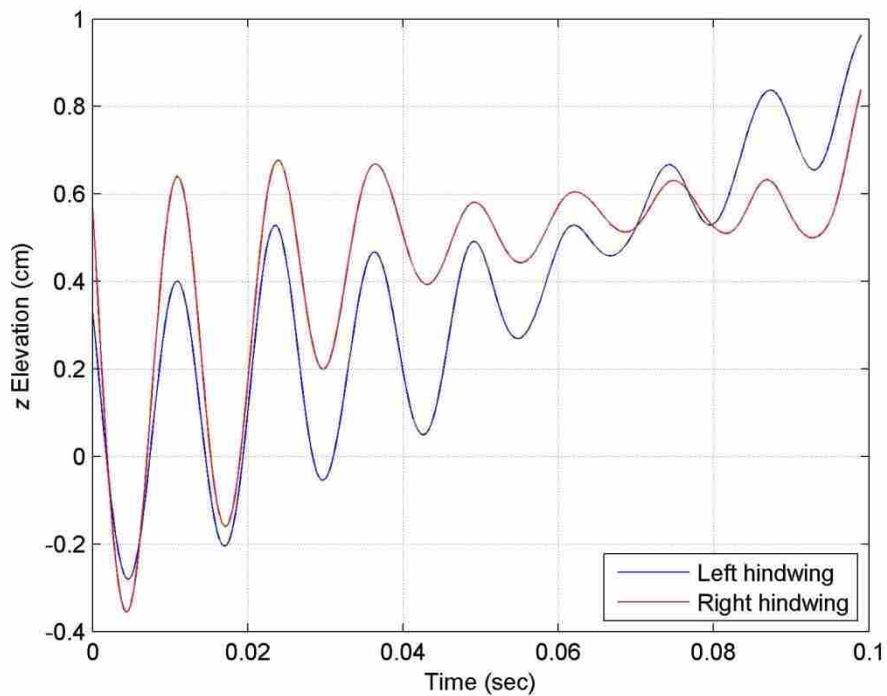


Figure 2-8. Ladybug hindwing amplitude.

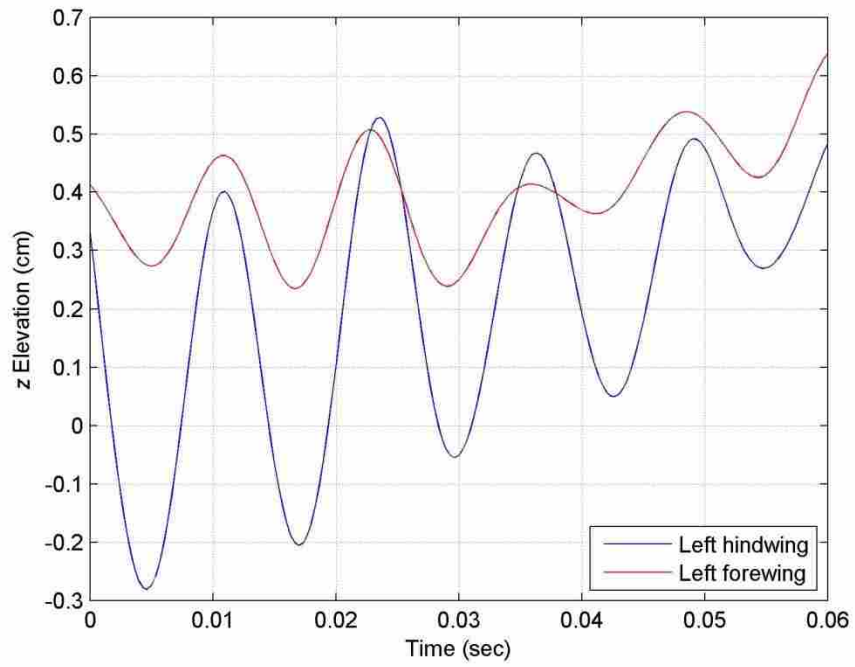


Figure 2-9. Vertical (z) position of forewing and hindwing.

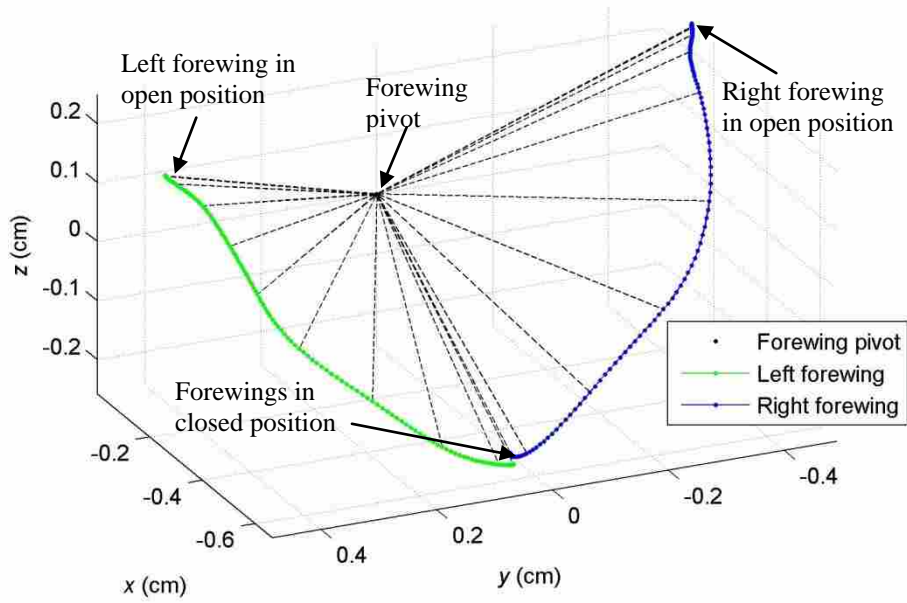


Figure 2-10. Ladybug forewing path during opening.

Figure 2-8 shows a ladybug hindwing path during takeoff and transitioning into horizontal flight. It is observed that the amplitude of the stroke elevation is large and contains steady strokes. Figure 2-9 shows an exploration of vertical displacement of both forewing and hindwing.

Figure 2-10 shows a quantification of both forewings of a ladybug specimen during opening. This kinematic identification shows that these forewings do not simply follow a straight line approach to their takeoff position, but follow a curved path.

Finally, in Figure 2-11, a unique behavior of the legs can be seen. The 2nd image in the sequence show the legs moving outward and the 3rd image in the sequence show the legs in an almost fully-extended position. This phenomenon in ladybugs was consistently observed in different ladybug videos. The purpose for this behavior is currently unknown.

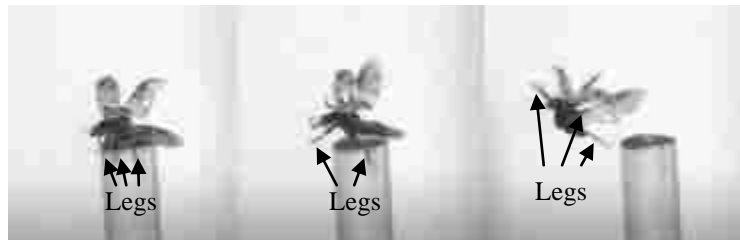


Figure 2-11. Image sequence showing ladybug leg extension.

2.3.2 Uncertainty of Measurements

Uncertainty due to the resolution of the high-speed camera was calculated by taking half the smallest area the camera could measure:

$$u_0 = \pm \frac{1}{2} \left[\frac{0.0657 \text{ cm}}{\text{pixel}} \right]. \quad (2-11)$$

Uncertainty due to the calibration of \mathbf{L} and \mathbf{R} vectors using the calibration target was measured by averaging the distance between the measured and calculated calibration coordinate. The calculated calibration coordinate was found by returning the pixel locations of the calibration points into Equation 2-6. The uncertainty was calculated by

$$u_{\text{calibration}} = \frac{1}{N} \sum_{j=1}^N \sqrt{(\Delta x^2 + \Delta y^2 + \Delta z^2)}, \quad (2-12)$$

where N is the total number of calibration points. This yielded an average coordinate error of 0.147 cm. Figure 2-12 shows the known positions of the calibration points of the calibration target compared to their calculated locations.

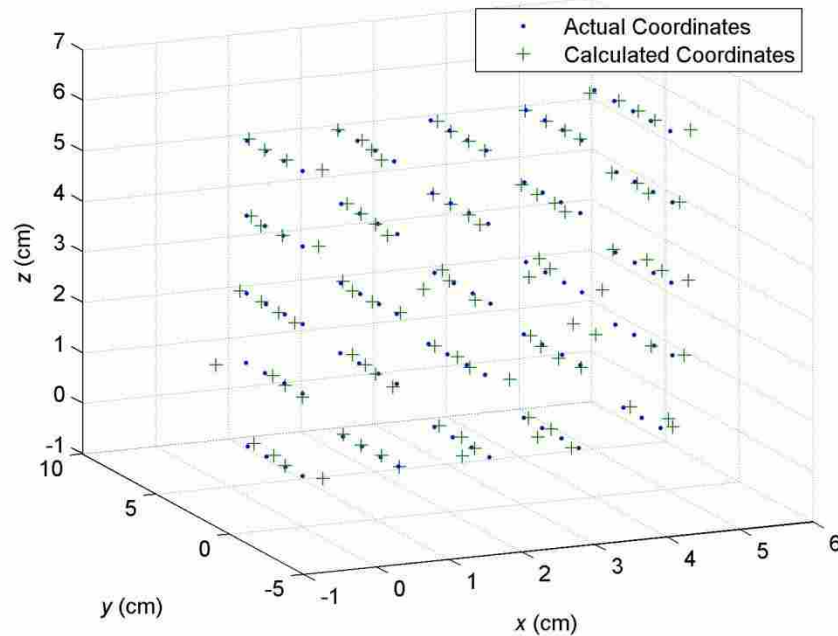


Figure 2-12. Actual location of calibration points plotted with their calculated location using DLT analysis.

The uncertainty in choosing the true pixel location was estimated to be ± 3 pixels (the approximate size of the key-point locations of the ladybug). The effect of mis-selecting a key-

point on the ladybug was quantified by moving the left pixel location, $[u_L \ v_L]$, up, down, left, and right and finding the maximum error, as shown in Table 2-2.

Table 2-2. Uncertainty table due to mis-selection of key-points.

Direction	Error (cm)
<i>x</i>	0.1838
<i>y</i>	0.0235
<i>z</i>	0.0503
Error Magnitude	0.192

The total uncertainty was then found by combining zero order (u_0), calibration ($u_{\text{calibration}}$), and mis-selection ($u_{\text{selection}}$) errors as defined by

$$u_{\text{total}} = \pm \sqrt{(u_0^2 + u_{\text{calibration}}^2 + u_{\text{selection}}^2)}, \quad (2-13)$$

where the total uncertainty, u_{total} , is ± 0.244 cm. The total error made up about 25% of the total flapping amplitude. This error was not ideal and in future research, the use of a more accurate calibration target would be beneficial in improving the quality of the calibration and consequently reducing the total error. Additionally, the use of multiple high-speed cameras would help improve image resolution.

2.4 Conclusion

The work presented represents results from data acquired from a series of high-speed images of a ladybug during takeoff. These results illustrated the functionality of the DLT implementation and calibration technique, the successful data acquisition of a ladybug in takeoff and free flight, and showed analysis of several sequences of video image data. A complete graphical representation of a ladybug during takeoff was presented. The average flapping

frequency was 78.6 Hz. The average takeoff velocity was 21.4 cm/s. The flapping amplitude of the forewing was observed to be relatively large in comparison to the amplitude of the hindwing. The extension of the ladybug's legs during takeoff was consistently observed between ladybugs. A graphical representation of the forewing opening before takeoff was also presented.

Data of this type may be useful in investigating the aerodynamics of insect flight, including the development and analysis of computational and experimental models. Of particular interest will be the aerodynamic interaction of the relatively stiff (but clearly not static) forewing-generated vortices with those generated by the much larger hindwings.

3 DESIGN OF A DIFFERENTIAL-DRIVEN FLAPPING-WING MECHANISM FOR FORCE ANALYSIS AND OPTIMIZATION

3.1 Introduction

In Chapter 2, the importance of understanding flapping flight in nature was discussed and the kinematics of a ladybug during takeoff were explored. In this chapter, the design of a flapping-wing mechanism capable of simulating wing motion of ladybugs and of other species is discussed. The way in which this mechanism can be used for both force analysis and optimization of the wing kinematics is addressed. The mechanism response is characterized and force measurements from the mechanism are demonstrated.

3.1.1 Background

The study of flapping flight from an experimental standpoint can bring insight into the lift-generating mechanisms produced during flapping. Developing our understanding of flapping-wing kinematics will enable the advancement of MAVs and MAV technology.

Although there currently exist many flapping wing mechanisms, there is a need for a dual-wing flapping mechanism which allows input of any user-specified trajectory, can be controlled from a remote location, has a wide range of motion, and is capable of measuring lift and thrust from the mechanism. This mechanism will serve as a test bed for flapping kinematic optimization and will provide insight into flapping flight for potential use in MAVs.

In this chapter the theory and design of such a flapping mechanism is presented and preliminary force measurements are discussed.

3.1.2 Related Work

Much has been learned from previous experiments using flapping-wing mechanisms. Prior mechanisms that are wide-ranging in terms of function, appearance, and design have been tested. Although these mechanisms do not have the complete functionality desired for the optimization methods discussed in Chapter 4, they are worth mentioning and have helped influence the design of this research and the research of others. Table 3-1 lists these mechanisms.

Table 3-1. List of flapping flight mechanisms and their function. List is organized chronologically, by date, and then alphabetically, by author.

Name	Adjustable kinematics		Operating Medium		Device Fixment		Purpose		
	Yes	No	Air	Liquid	Fixed	Un-tethered	Flow viz/PIV	Force Analysis	Flight
Smith (1996)[29], Smith (2001)[30]	✓		✓		✓	✓		✓	✓
Van den Berg (1997)[8], Ellington (1999)[5]	✓		✓		✓		✓		
Dickinson (1999)[31]	✓			✓	✓			✓	
Fearing (2000)[32], Sitti (2001)[33]	✓		✓		✓			✓	
Frampton (2000)[34]		✓	✓		✓			✓	
Pornsiri-Sisirak (2000)[35]		✓	✓			✓			✓
Yan (2001)[36]	✓		✓			✓		✓	✓
Cox (2002)[37]	✓		✓		✓			✓	
Avadhanula (2003)[38], Yan (2003)[39]	✓		✓			✓		✓	✓
Raney (2003)[40]	✓		✓		✓			✓	
Tarascio (2003)[41], Singh (2008)[42]		✓	✓		✓			✓	
Burgess (2004)[43]		✓	✓		✓			✓	

Table 3-1. Continued.

Name	Adjustable kinematics		Operating Medium		Device Fixment		Purpose		
	Yes	No	Air	Liquid	Fixed	Un-tethered	Flow-viz/PIV	Force Analysis	Flight
Mankame (2004)[44]		✓	✓		✓	✓		✓	✓
Maybury (2004)[45]	✓		✓		✓			✓	
Thomas (2004)[46]		✓	✓		✓		✓		
Banala (2005)[47]		✓	✓		✓			✓	
Galinski (2005)[48], Zbikowski (2005)[49]		✓	✓		✓		✓	✓	
Lai (2005)[50]	✓			✓	✓			✓	
Madangopal (2005, 2006)[51],[52]		✓	✓		✓	✓		✓	✓
McIntosh (2005)[53], Agrawal (2010)[54]		✓	✓			✓		✓	
Tanaka (2005)[55]		✓	✓		✓	✓	✓		✓
Yamamoto (2005)[56]		✓	✓		✓			✓	
Conn (2006, 2007)[57], [58]	✓		✓		✓			✓	
Issac (2006)[59]	✓			✓	✓			✓	
Syaifuddin (2006)[60], Nguyen (2008)[61]	✓		✓			✓	✓	✓	✓
DiLeo (2007)[62]	✓			✓	✓			✓	
Khan (2007)[63]		✓	✓		✓			✓	
Wood (2007)[64]	✓		✓		✓	✓		✓	✓
Yang (2007)[65]		✓	✓			✓		✓	✓
Bunget (2008)[66]		✓	✓		✓		✓		
Grand (2008)[67]		✓	✓			✓			✓
Lentink (2008)[68]		✓		✓	✓		✓		
Maglasang (2008)[69]		✓	✓		✓		✓	✓	
Nagai (2008)[70]	✓			✓	✓			✓	
Park (2008)[71]		✓	✓			✓			✓
Bejgerowski (2009)[72]		✓	✓			✓		✓	✓
Bolsman (2009)[73]	✓		✓		✓			✓	
Finio (2009)[74]	✓		✓			✓			✓
Hubel (2009)[75]		✓	✓		✓		✓	✓	
Krashanitsa (2009)[76]		✓	✓			✓		✓	✓
Massey (2009)[77]		✓	✓		✓		✓	✓	
Thomson (2009)[22]	✓			✓	✓			✓	
Tsai (2009)[78]		✓	✓			✓		✓	✓
Fenelon (2010)[79]	✓		✓		✓			✓	
Han (2010)[80]		✓		✓	✓		✓	✓	
Mukherjee (2010)[81]	✓		✓		✓	✓		✓	✓

Several of the above mechanisms are similar in design to the mechanism presented in this chapter. Van den Berg and Ellington [8] created a flapping mechanism based on a differential design called “The Flapper.” This mechanism was designed for use in air and although this mechanism is capable of adjustable kinematics, both wings cannot flap independently. Dickinson and Sane [31] and DiLeo and Deng [62] both built mechanisms based on a robotic wrist mechanism. This design allowed a large range of motion while still keeping critical components out of the water. Lai et al. [50] introduced a mechanism also based on a differential gear design and used timing belts to drive each of the two inputs of the differential. The *rotation angle* used a rather cumbersome turntable which did not allow for two wings.

The mechanism design discussed in this chapter has adjustable kinematics, can operate in water, oil, or air, is fixed, and can be used for flow visualization, particle image velocimetry (PIV), and force analysis. Although certain of the above mechanisms do meet these same functional criteria, they either do not have precision control using encoder feedback or do not have two wings to enable simulation of clap-and-fling.

3.2 System Design

A six-degree-of-freedom (6-DOF) flapping mechanism capable of executing arbitrary flapping trajectories was developed to explore the relationship between flapping trajectory, resulting wing forces, and flow patterns. Each wing was designed to have 3 DOFs, as shown in Figure 3-1. Rotation by θ_1 about the z -axis is referred to as the *rotation angle*; rotation by θ_2 about the y -axis is referred to as the *elevation angle*; and rotation by θ_3 about the x -axis is referred to as the *feathering angle*. To enable exploration of a wide range of flapping motions, the mechanism was designed to enable motions of $\theta_1 = \pm 90^\circ$, $\theta_2 = +55/-105^\circ$, and $\theta_3 = \pm 180^\circ$

(based on the mechanical limits of mechanism) (see Figure 3-1). The mechanism was designed to flap at a maximum frequency of 0.667 Hz, as defined by the trajectories described in Section 3.2. The design minimized gear backlash. It was also designed for ease of setup and use, interchangeability of wing shapes and materials, and for interfacing with software for convenient implementation of new optimization schemes. The mechanism is capable of measuring lift and thrust and can function in water, oil, or air.

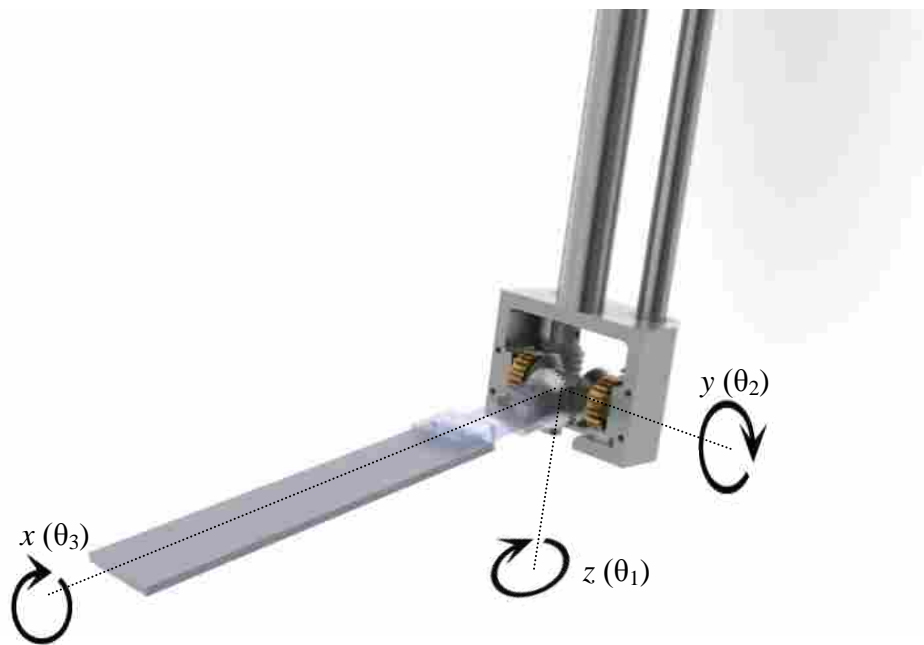


Figure 3-1. Coordinate definitions of the flapping wing mechanism.

3.2.1 Mechanism Design

The design of the flapping mechanism is based on a differential gear model similar to the design by Van den Berg et al. [8] and Lai et al. [50]. Differentials transfer torque and rotational motion and are most commonly used in one of two ways. The first is one input and two outputs;

the second is two inputs that create an output that is the sum, difference, or average of the inputs depending on their speed and direction. Using two inputs allows for two output DOFs. This was the approach taken for the flapping mechanism θ_2 and θ_3 control. The third DOF (θ_1) is achieved by rotating the entire differential about its z -axis.

The mechanism design includes a differential assembly housed inside of a frame (Figure 3-2) (see Appendix B.1). Spur gears are mounted on the two input-differential gears. These spur gears are driven by worm gears mounted directly behind the spur gear to keep the design compact (Figure 3-3). The worm gears are mounted to long shafts which extend upwards out of the working fluid. Motors are directly mounted to the worm gear shaft to drive the two differential inputs (Figure 3-4).

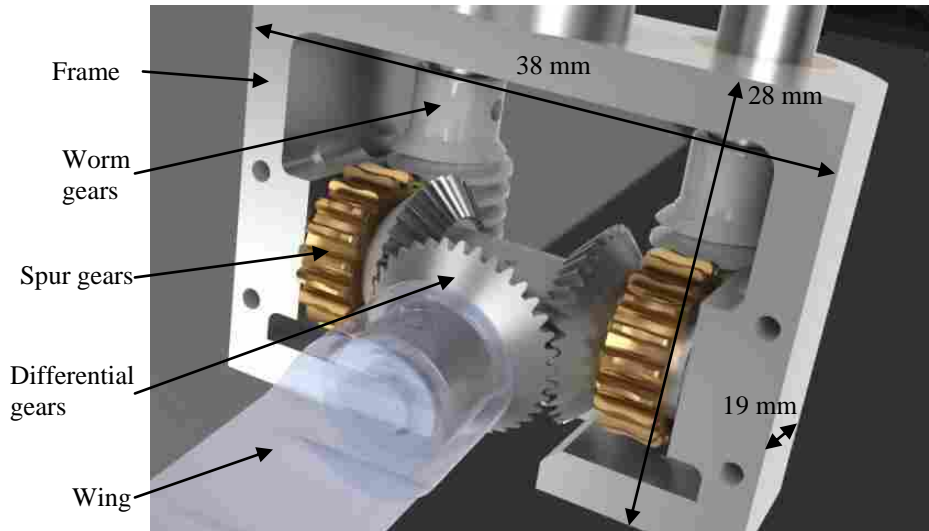


Figure 3-2. Differential housed inside of a frame. The frame is supported from above and the wing attaches to the output of the differential.

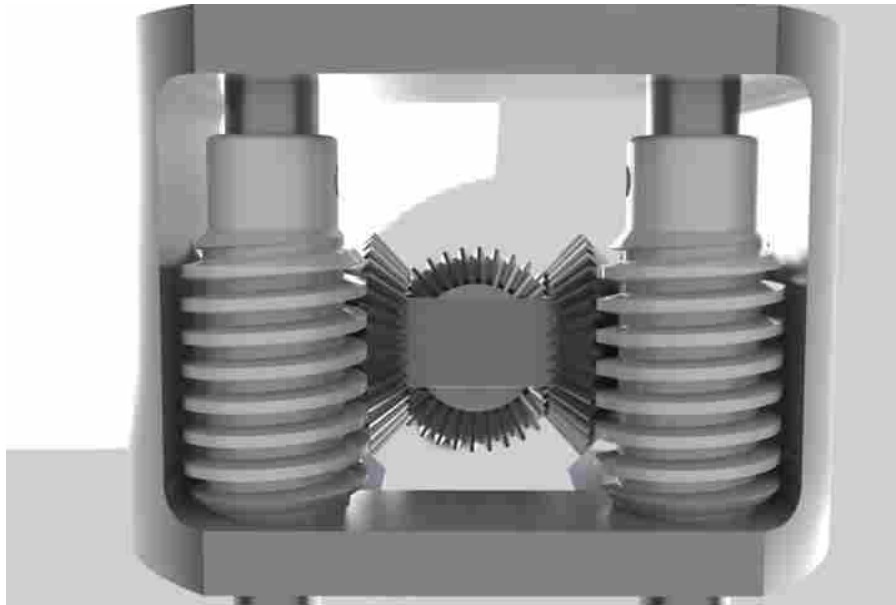


Figure 3-3. Worm gears located directly behind the two differential inputs for compact design.

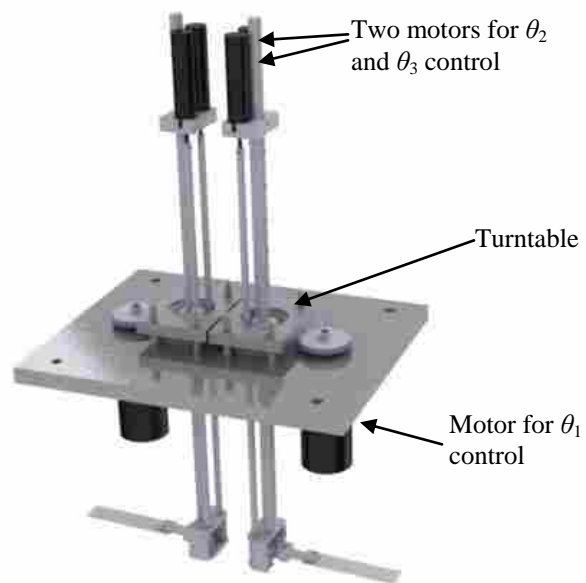


Figure 3-4. Motors mounted to the top of the mechanism about a turntable for θ_1 rotation.

The third DOF sits about a turntable mounted above and directly in line with the longitudinal axis of the mechanism. The turntable contains gear teeth which interface with a motor mounted in the same plane.

Two identical mechanisms are arranged back-to-back on a plate. For the studies mentioned here, the plate was mounted to slotted framing which sits atop a water flume.

This design was chosen after careful consideration of other designs. Other designs either did not provide adjustable kinematics, did not have encoder feedback for trajectory control, or did not meet the design requirements for the desired tests. The proposed model allowed for adjustable kinematics, was capable of being submerged in water, and had two wings which allowed for the exploration of clap and fling.

The system was modeled using SolidWorks. All gears, bearings, pins, and clips were off-the-shelf components (see Appendix B.1 for bill of materials). All other parts were custom designed and toleranced (see Appendix B.2 for tolerancing).

3.2.2 Actuation and Control

Each DOF was actuated by brushless DC motors with integrated incremental encoders for position feedback and force-vector resolution. The θ_1 DOF was driven by a Maxon motor (part number EC 40-118899) with a stall torque of 363 mN·m, no-load speed of 3100 rpm, and integrated 500 count-per-turn encoder. The θ_2 and θ_3 DOFs were driven by identical Maxon motors (part number EC 16-232241) with a stall torque of 184 mN·m, no-load speed of 41400 rpm, and integrated 512 count-per-turn encoders. All six motors were driven by Advanced Motion Controls BE15A8 PWM servo drives that receive analog voltage commands from the controller.

A six-channel controller was developed to enable the flapping mechanism to track the desired angle trajectories $\theta_{1d}(t)$, $\theta_{2d}(t)$, and $\theta_{3d}(t)$ for each wing (where the subscript d denotes the desired angle). The controller was developed in LabVIEW and implemented on a National Instruments (NI) CompactRIO Real-Time Controller (cRIO-9074) augmented with an NI 9263 analog output module (for generating motor command voltages), an NI 9237 bridge module (for reading strain gauge outputs; see Section 3.2.3), and an NI 9411 digital input module (for reading the encoders). Six independent PID controllers running at a rate of 500 Hz were implemented on the FPGA layer of the cRIO. The PID gains were tuned experimentally to ensure stability and satisfactory trajectory tracking in air and water. The FPGA layer also handled all sensor and motor I/O and communication with the PC layer, and the PC layer generated the desired trajectories using MATLAB.

3.2.3 Instrumentation

The objective of the mechanism's instrumentation is to measure the flapping angles ($\theta_1(t)$, $\theta_2(t)$, and $\theta_3(t)$, actual angles of flapping mechanism), the lift force (f_L), and the thrust force (f_T) as the mechanism executes specified flapping trajectories. As mentioned previously, the flapping angles are sensed using encoders attached to the motors and recorded using the digital module of the cRIO. The resultant force vector on the wing is measured using four waterproofed strain gauges [82] affixed to a wing bracket at the base of the wing (see Figure 3-5). The gauges are connected in a full-bridge configuration and its output is conditioned using the bridge module of the cRIO. The force thus obtained is the force vector exerted on the wing and expressed in the wing-fixed coordinate frame. The objective of this work is to find flapping trajectories that maximize lift and thrust forces, which, by definition for a stationary, horizontally

oriented body, are defined in the earth-fixed vertical (z) and forward (y) directions, respectively. It is therefore necessary to transform the force vector measured in the wing-fixed frame into the earth-fixed frame. This is accomplished by a 3-2-1 Euler angle transformation in which the axes are first rotated by angle θ_1 about the vertical axis, followed by a rotation by angle θ_2 about the horizontal shaft axis, followed by a rotation by angle θ_3 about the wing axis. The resulting rotation matrix is given by

$$R(\theta_3, \theta_2, \theta_1) = \begin{bmatrix} 1 & 0 & 0 \\ 0 & \cos \theta_3 & -\sin \theta_3 \\ 0 & \sin \theta_3 & \cos \theta_3 \end{bmatrix} \begin{bmatrix} \cos \theta_2 & 0 & \sin \theta_2 \\ 0 & 1 & 0 \\ -\sin \theta_2 & 0 & \cos \theta_2 \end{bmatrix} \begin{bmatrix} \cos \theta_1 & \sin \theta_1 & 0 \\ -\sin \theta_1 & \cos \theta_1 & 0 \\ 0 & 0 & 1 \end{bmatrix}. \quad (3-1)$$

The force expressed in the earth-fixed frame can then be found from the single component of force measured in the wing-fixed frame using

$$F_{earth} = R(\theta_3, \theta_2, \theta_1)^T F_{wing}. \quad (3-2)$$

The angles used in the transformation, $[\theta_1, \theta_2, \theta_3]$, are measured in real-time using the motor encoders, as described previously. Because the center of pressure is constantly changing throughout the flapping cycle, a bending moment force sensor is not adequate to resolve lift and thrust forces [31]. To eliminate any potential for calibration errors due to the constantly shifting center of pressure, force values are left in arbitrary units (au) to properly compare them against each other.

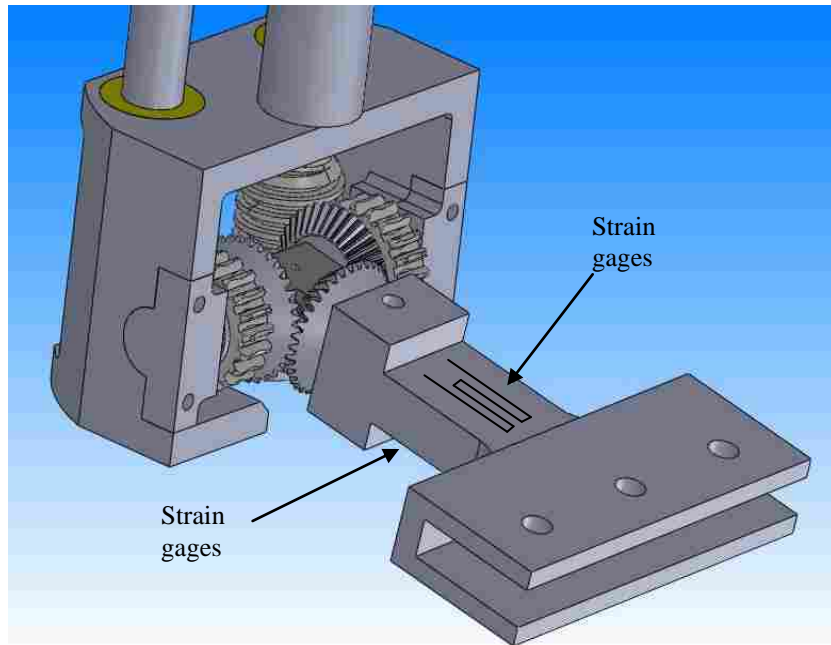


Figure 3-5. Strain gages fixed to a wing mounting bracket.

3.3 Methods

To test the flapping mechanism, a structure was built to place the flapping mechanism in the center of a flume measuring 1.2 m wide, 0.33 m deep, and 10 m long. The structure allowed the flapping mechanism to be placed securely at any position along the flume length. Width and length adjustments could be made to place the mechanism in any position, while the depth adjustment was only allowed in discrete steps of 0.025 m (1 in). Flume water velocity was set to 0.25 m/s.

3.3.1 Wing Trajectories

The desired flapping trajectories were defined using the first five terms of a Fourier series expansion for each degree of freedom,

$$\begin{aligned}
\theta_1(t) &= A_{11} + A_{12} \sin \omega t + A_{13} \cos \omega t + A_{14} \sin 2\omega t + A_{15} \cos 2\omega t \\
\theta_2(t) &= A_{21} + A_{22} \sin \omega t + A_{23} \cos \omega t + A_{24} \sin 2\omega t + A_{25} \cos 2\omega t, \\
\theta_3(t) &= A_{31} + A_{32} \sin \omega t + A_{33} \cos \omega t + A_{34} \sin 2\omega t + A_{35} \cos 2\omega t
\end{aligned} \tag{3-3}$$

where A_{11} through A_{35} are the coefficients for each term, ω is the desired flapping frequency, and t is time. This is similar to the approach employed by Aono et al. [83], [84] but with fewer terms. It is acknowledged that five terms may not be sufficient to accurately represent some highly complex flapping trajectories observed in nature. However, the purpose of this work is not to replicate the flight of a particular insect or bird. The purpose is instead to develop methods to find the optimal instance of a given trajectory structure by assigning numerical values to the trajectory parameters. The number of terms, therefore, was selected (1) to give suitable flexibility to the achievable flapping patterns, and (2) to decrease the parameter space that must be searched by the optimization method. Additional Fourier terms may be added if additional complexity is required.

In each experimental run, high-level MATLAB optimization code running on a PC generates desired flapping trajectories $\theta_{1d}(t)$, $\theta_{2d}(t)$, and $\theta_{3d}(t)$ and sends the trajectories to the controller running on the cRIO. The flapping mechanism executes the trajectories, records the angle and force data from the encoders and strain gauges, resolves the forces into the earth-fixed frame, and sends the data to the MATLAB optimization code. The MATLAB code then uses these data to explore the feasible design space and optimize the wing trajectory. Details of how the optimization software iterates on the measured data to obtain the next set of desired trajectories are explained in Chapter 4.

In general, the final angle of a previous trajectory will not match the initial angle of the current trajectory. This occurs as the optimization algorithm selects new parameters in Equation 3-3. To enable smooth transitions between subsequent trajectories, each DOF is driven from its

zero angle to the initial desired trajectory angle using a quintic polynomial trajectory over a period of one second at the beginning of each run. A quintic polynomial ensures a smooth transition into the desired trajectory by matching the angle, angular velocity, and angular acceleration at the transition point [85]. Similarly, each DOF is driven from its final desired trajectory angle to its zero angle at the end of each run using a quintic polynomial trajectory.

Wing trajectories are converted motor commands to compensate for the additional complexity introduced by the worm gear drive. The gear ratio of the worm to spur gear is 20:1, thus to compensate for the worm gear the trajectory angles must include a factor of 20. Both shafts must be turned in the same direction to achieve θ_2 motion, thus the sign for θ_2 in both motor 2 and 3 is positive. Both shafts must be turned in opposite directions to achieve θ_3 motion, thus the signs for θ_3 in motor 2 and 3 alternate. Resulting motor commands are found by

$$\begin{aligned} Motor_1 &= \theta_1 \\ Motor_2 &= 20\theta_2 + 20\theta_3 . \\ Motor_3 &= 20\theta_2 - 20\theta_3 \end{aligned} \tag{3-4}$$

Each experimental run consists of an initial one-second transition from the zero angle configuration, followed by six cycles of the experimental trajectory defined by Equation 3-3, and a final one-second transition back to the zero angle configuration. To minimize transient effects and to enable signal averaging, the two transition periods and the first period of the desired trajectory are excluded in evaluating the average vertical force [86].

Frequency selection and fluid flow velocity are calculated using Reynolds and Strouhal number scaling. Given a reference length L_{ref} , a reference velocity U_{ref} , and the kinematic viscosity, ν , the Reynolds number is defined as

$$Re = \frac{U_{ref} L_{ref}}{\nu} . \tag{3-5}$$

Given a flapping frequency, f , the Strouhal number is defined as

$$\text{St} = \frac{L_{ref} f}{U_{ref}}. \quad (3-6)$$

Combining Equations 3-5 and 3-6 yields

$$f_{scale} = \left(\frac{v_{scale}}{v_{animal}} \right) \left(\frac{L_{animal}}{L_{scale}} \right)^2 f_{animal}, \quad (3-7)$$

where v_{scale} and L_{scale} depend on the experimental setup. The fundamental frequency is 0.33 Hz (thus approximately two optimization iterations can be completed per minute). For the studies mentioned here, L_{scale} is chosen to be 0.14 m, v_{scale} is $1.12 \times 10^{-6} \text{ m}^2/\text{s}$ (kinematic viscosity of water) and f_{scale} is found to be 0.33 Hz [1]. For the studies mentioned in this chapter, a wing profile resembling a ladybug wing was used [87]. For studies in Chapter 4, a wing profile resembling a zebra finch was used [88], [89]. Both wing profiles are made from acrylic measuring about 3 mm thick (0.125 in).

3.3.2 Optimization Approach

Two schemes were used to optimize wing kinematics of the flapping-wing mechanism. Both schemes were based on the three-level Box-Behnken screening design to vary the model parameters [90], [91]. In this approach, the Box-Behnken varies the coefficients of the Fourier-series expansion that describe the wing trajectories in Equation 3-3. This method is an efficient way of exploring a model which may have a large design space. Although the details of this optimization are not described in this section, they are introduced since trajectories determined using this screening design were repeated twice using the same trajectory (see Section 4.2.1 for

further details). Performing this allows resulting forces to be compared for consistency and for quantifying mechanism uncertainty.

3.4 Results

3.4.1 Mechanism Response

A swept sine wave with an amplitude of 45° and frequency content of 0-5 Hz was input into each DOF of the flapping mechanism using closed-loop control. Each DOF was driven independently with the wing attached. This was performed in both flowing water ($u_y = 0.25$ m/s) and quiescent air. The closed-loop system response indicated the physical capabilities of the system and its ability to track trajectories at different frequencies. Figure 3-6 shows the response of the system.

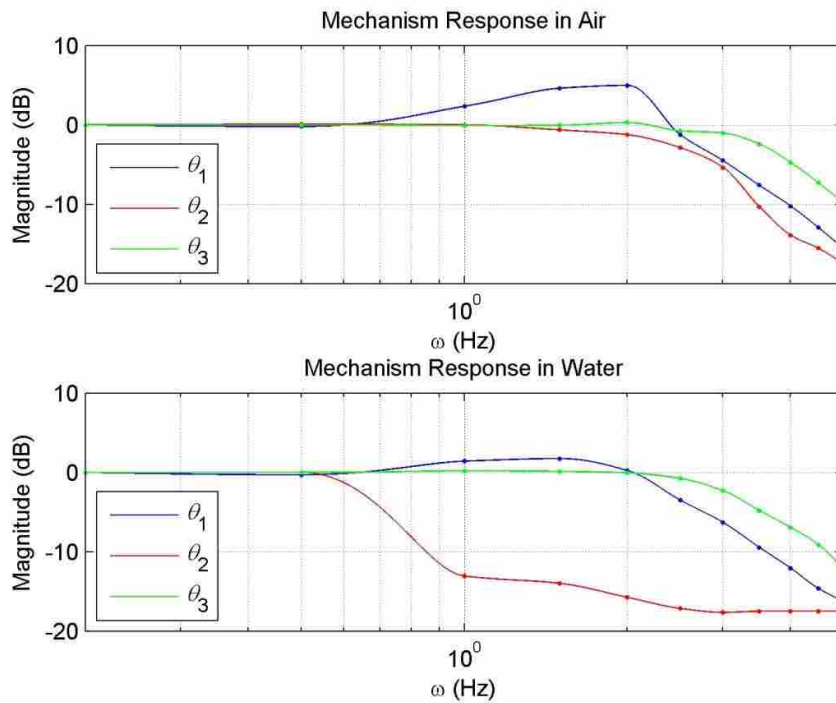


Figure 3-6. Mechanism response for all DOFs using a swept sine (0-5 Hz) input.

The mechanism is capable of tracking all 3 DOFs at low frequencies with little error. Higher frequencies (0.5-1 Hz) did exhibit some trouble tracking in the θ_2 DOF. This response was the cause for some tracking error when the mechanism was attempting to track large-amplitude high-frequency kinematics. Figure 3-7 shows tracking results for an arbitrary flapping pattern for the mechanism flapping in water flowing at 0.25 m/s.

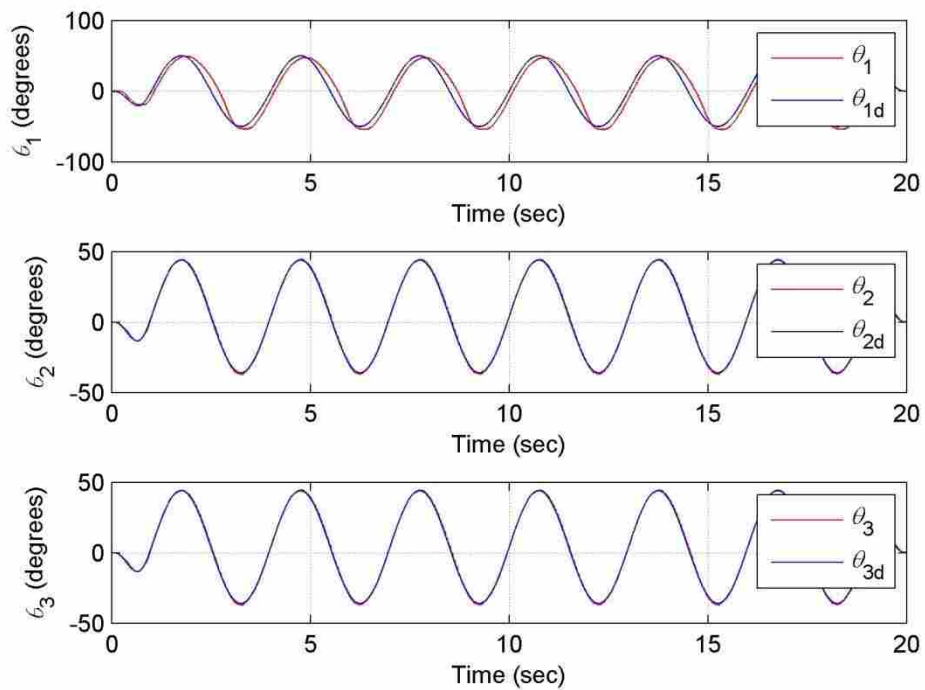


Figure 3-7. Tracking results of an arbitrary flapping trajectory.

3.4.2 Lift and Thrust Production

The Box-Behnken screening design (consisting of 432 runs) was performed twice for the starting point (A) and step sizes defined in Table 3-2. A ladybug wing shape was used for wing design (see Figure 3-8) [87]. Flume water velocity was 0.25 m/s. Figure 3-9 shows averaged lift

vs. averaged thrust for each run. The Box-Behnken design identified trajectories with improved thrust of 4.55 units and lift of 2.64 units relative to the starting trajectories.

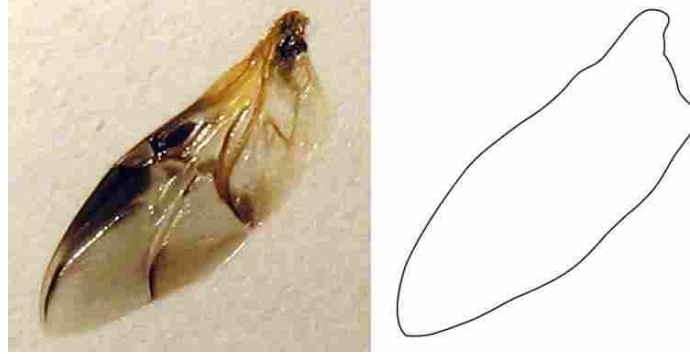


Figure 3-8. Ladybug wing and outline used for acrylic wing fabrication.

Table 3-2. Step size for Box-Behnken testing and trajectories for runs labeled in Figure 3-9. Bolded values indicate a deviation from the starting trajectory (A).

	Step Size (°)	A (°)	B (°)	C (°)	D (°)
A ₁₁	24	0	0	0	0
A ₁₂	32	50	50	50	50
A ₁₃	32	0	0	0	0
A ₁₄	32	0	0	0	0
A ₁₅	32	0	-32	32	-32
A ₂₁	24	-20	-20	4	-20
A ₂₂	32	40	40	40	72
A ₂₃	32	0	0	0	0
A ₂₄	32	0	0	0	0
A ₂₅	32	0	0	0	0
A ₃₁	24	0	24	0	0
A ₃₂	32	0	0	0	0
A ₃₃	32	45	45	45	45
A ₃₄	32	0	0	0	0
A ₃₅	32	0	0	0	0

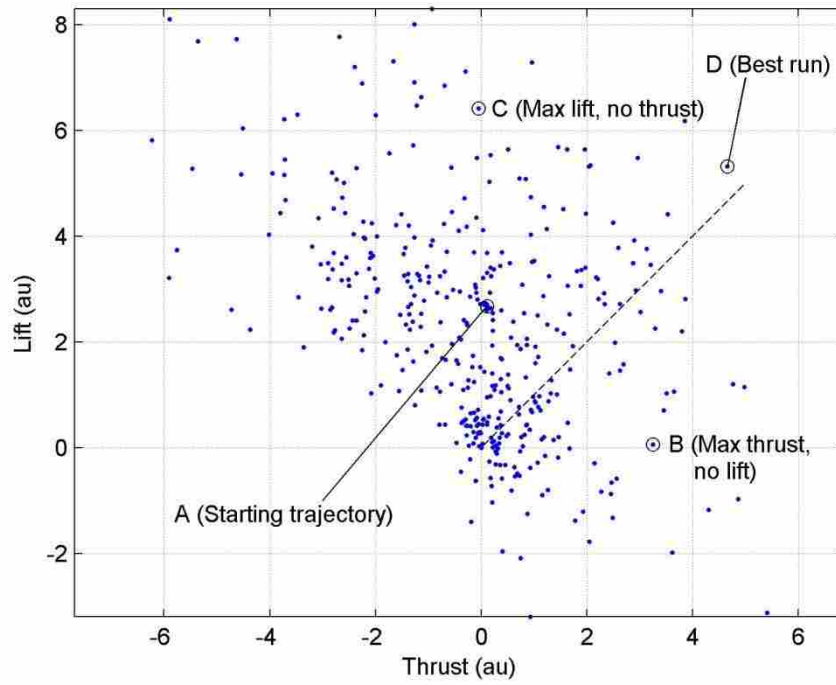


Figure 3-9. Lift and thrust values averaged from two identical Box-Behnken iterations (432 runs performed twice). The dashed line represents the direction of the desired force.

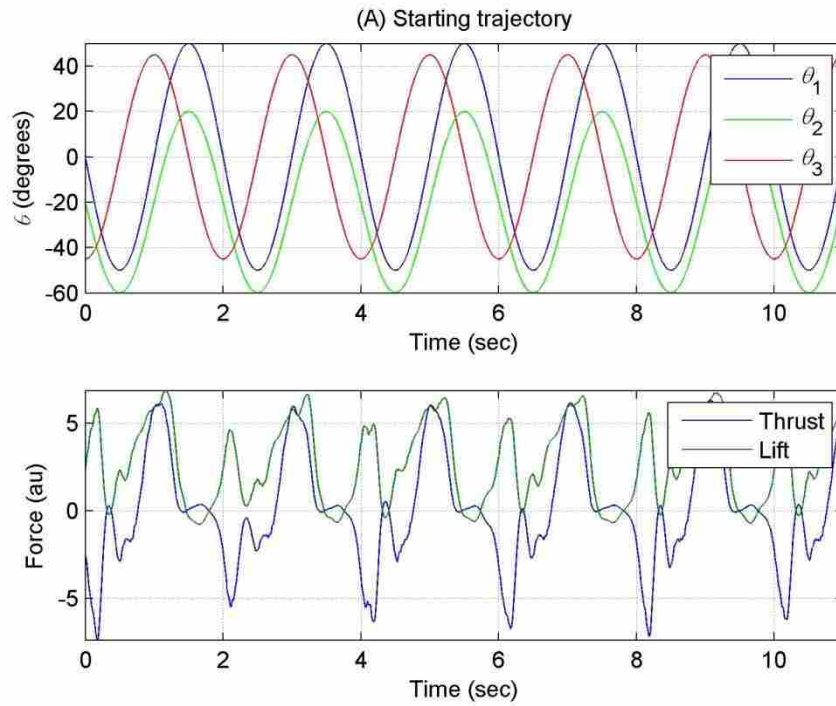


Figure 3-10. Force and trajectory history for (A) starting trajectory.

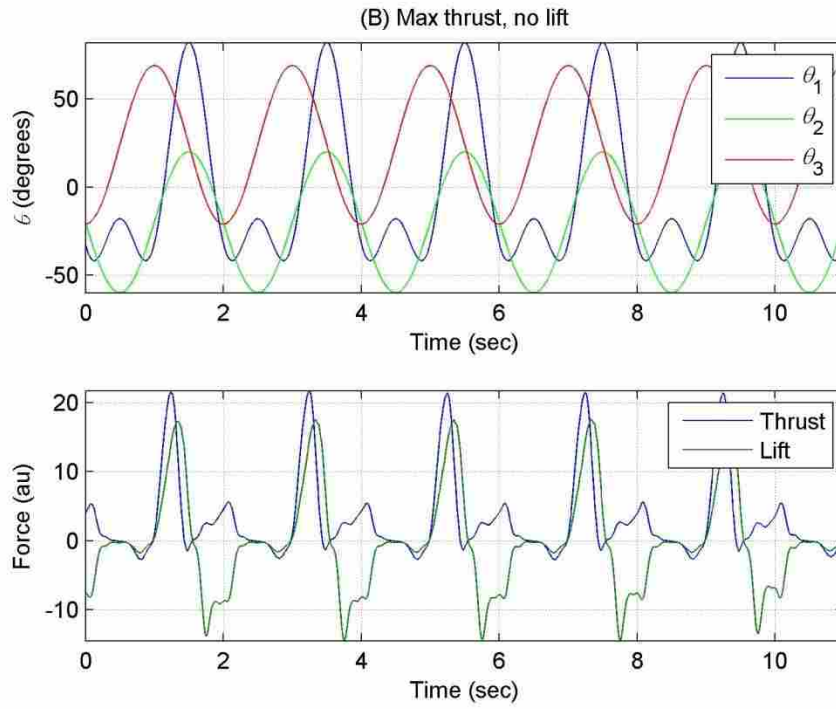


Figure 3-11. Force and trajectory history for (B) max thrust, no lift.

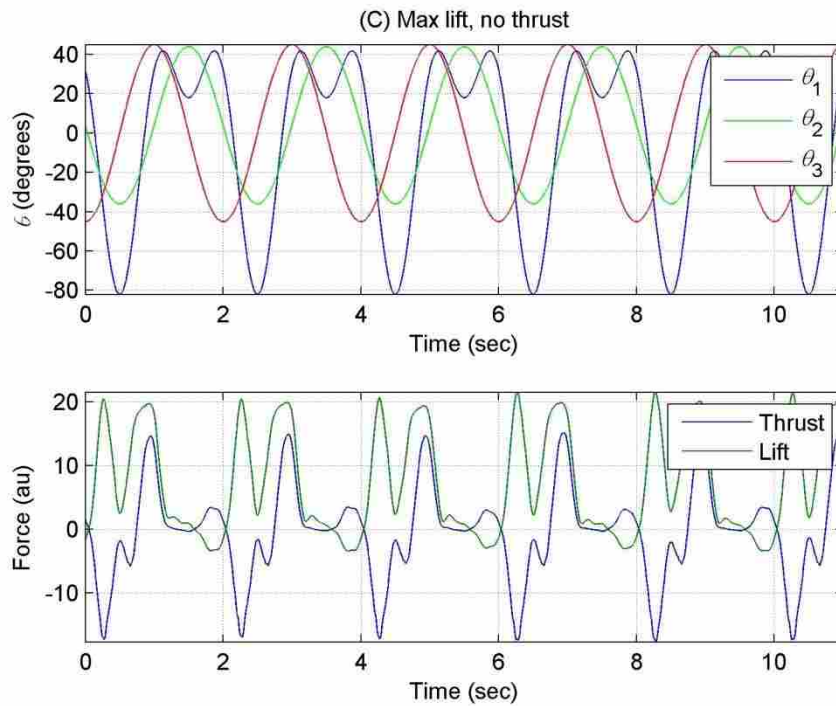


Figure 3-12. Force and trajectory history for (C) max lift, no thrust.

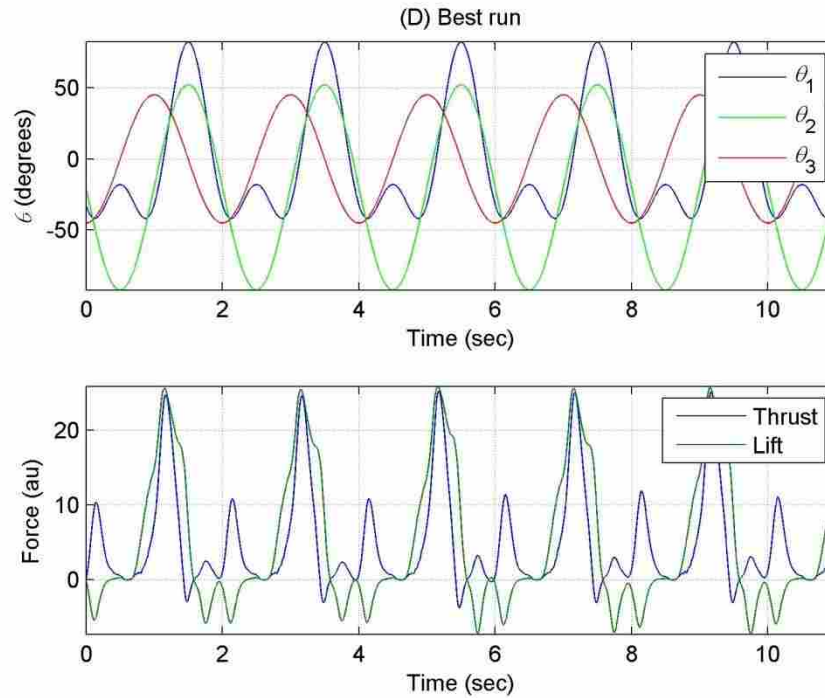


Figure 3-13. Force and trajectory history for (D) best run.

Figure 3-10 represents the starting trajectory (A) identified in Figure 3-9. The force history shows positive lift and neutral thrust. Figure 3-11 represents the trajectory exhibiting the maximum thrust with neutral lift (B). The force history shows wholly positive thrust and neutral lift. Figure 3-12 represents the trajectory exhibiting the maximum lift with neutral thrust (C). The force history shows two strong positive peaks of lift and neutral thrust. Figure 3-13 represents the trajectory considered to be the best run (D). This was chosen by the run that was furthest out in the search direction (dotted line) and within a reasonable tolerance of the line. The force history shows strong lift and thrust peaks generated in phase of each other with small, less significant peaks between.

Figure 3-14 contains force magnitude outputs for both Box-Behnken design runs (432 runs performed two times). The data follow a linear trend showing consistency in the

measurements. Runs that deviate from the dotted line are runs that did not track the commanded trajectory consistently between iterations.

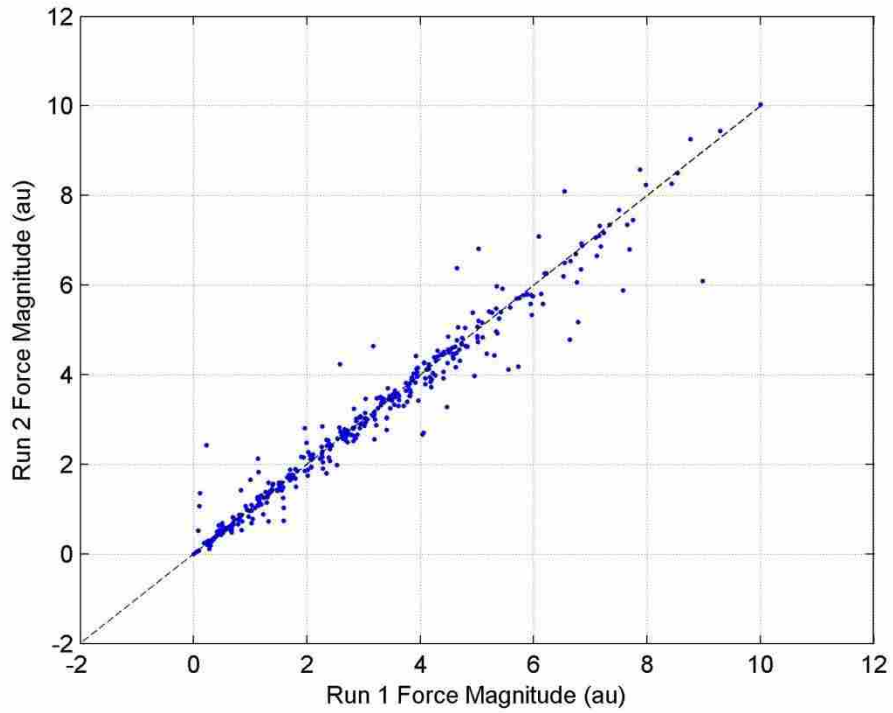


Figure 3-14. Force magnitude outputs compared over two iterations.

Figure 3-15 shows the unresolved force output for a single arbitrary trajectory. This trajectory was run 24 times (12 consecutive runs performed twice). Resulting force output is plotted, again showing consistency in the data. Figure 3-16 shows ensemble averaged force output from 24 runs.

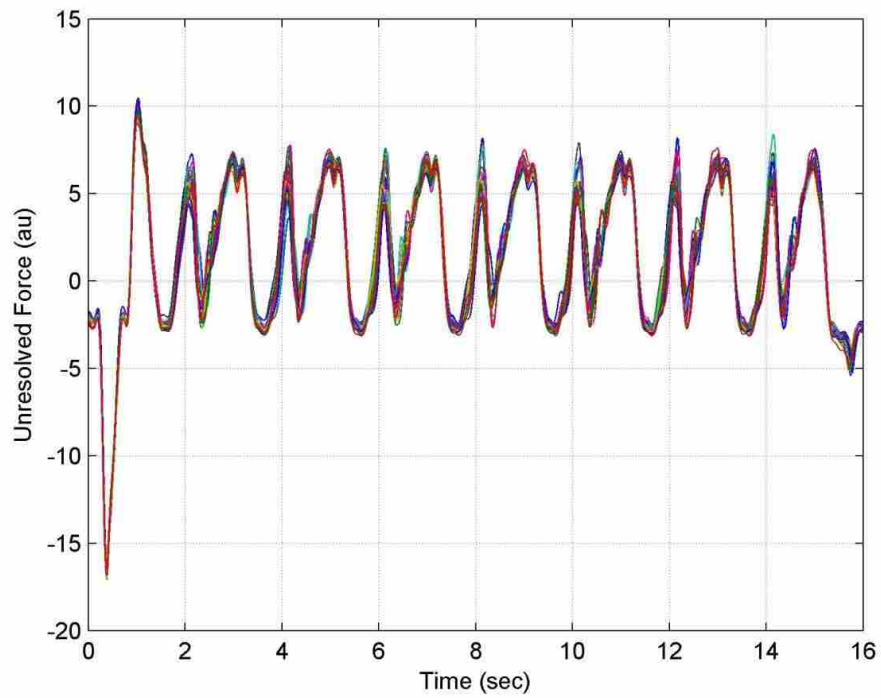


Figure 3-15. Force output for an arbitrary flapping trajectory performed 24 times.

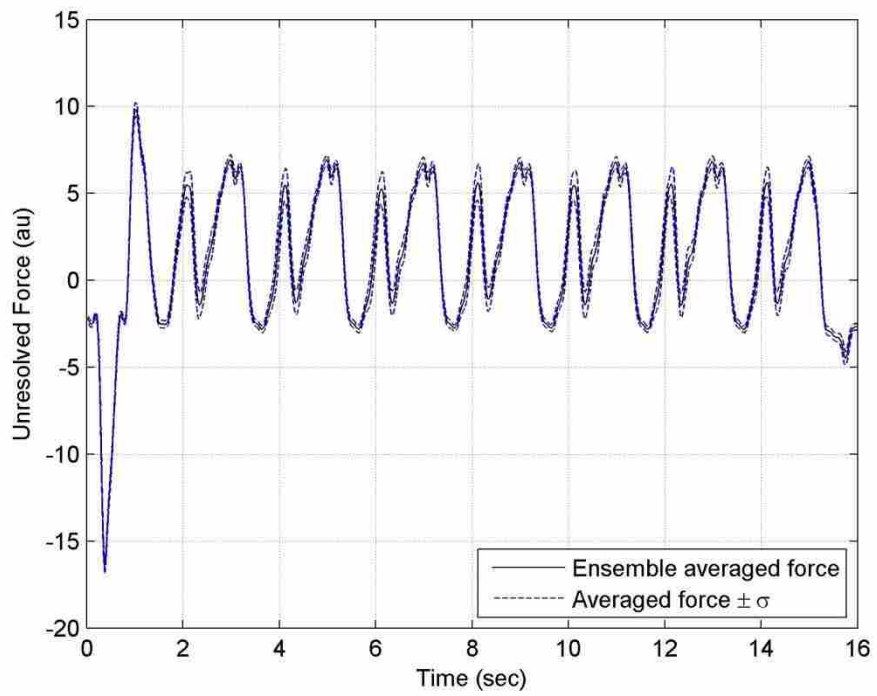


Figure 3-16. Ensemble-averaged force output, along with standard deviation, of 24 runs.

Since measurements from the strain gage contain noise, this noise is filtered post-process in MATLAB using a 3rd-order Butterworth filter with a cutoff frequency of 5 Hz. Figure 3-17 shows a plot of raw, unresolved force data plotted against filtered force data.

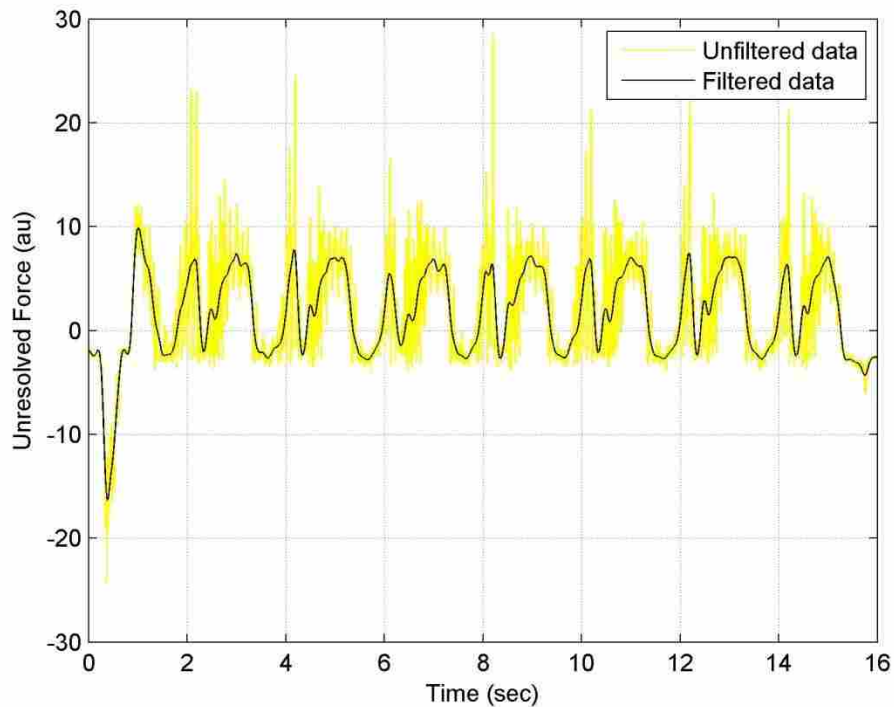


Figure 3-17. Filtered and unfiltered force output for an arbitrary flapping trajectory.

3.4.3 Force Uncertainty

Although force measurements are presented in arbitrary units, there is still a certain degree of uncertainty in the measurements. The main contributing factors to uncertainty are (1) noise in the raw data signal from the strain gages, (2) position error due to encoder resolution,

and (3) position error due to gear backlash. The latter is quantified by comparing differences in force output from identical runs. The error due to noise in the strain gages is estimated by

$$u_{0,noise} = \pm \frac{1}{2} [0.218 \text{ au}]. \quad (3-8)$$

The error due to the resolution of the encoders was estimated by finding the change in force output due to a change in the motor position. This motor position was defined by the minimum change in angle that the encoder is capable of measuring ($\theta_1=0.119^\circ$, $\theta_2=\theta_3=0.176^\circ$). The error, $u_{resolution}$, due to the encoder resolution was 0.0148 au.

The error due to backlash present in the differential gears was estimated by measuring the backlash of each DOF ($\theta_1=0.5^\circ$, $\theta_2=4^\circ$, $\theta_3=2^\circ$) and finding the resulting change in the force output due to the change in position from the gear backlash. The total error due to backlash present in the differential gears was $u_{backlash} = 0.1377$ au.

The total force output uncertainty is estimated by

$$u_{total} = \pm \sqrt{(u_{0,noise}^2 + u_{resolution}^2 + u_{backlash}^2)}. \quad (3-9)$$

The total uncertainty was $u_{total} = \pm 0.176$ au.

3.5 Conclusions

The mechanism described in this chapter used a differential gear design to achieve two DOFs. The third DOF is achieved through a rotating turntable. Each side of the mechanism is driven by three brushless motors and is capable of accurately tracking trajectories from 0-0.5 Hz in water and 0-1 Hz in air. The mechanism has adjustable kinematics, is capable of flapping in harsh environments (e.g., underwater), and can measure flapping force in real time.

Additionally, two wings sit back to back, allowing the experimental investigation of the effects of clap-and-fling.

Resulting forces show that the Box-Behnken design is a meaningful approach to exploring the design space. The Box-Behnken design method found a trajectory that improved lift and thrust by 2.64 and 4.55 units, respectively. The uncertainty of these measurements is ± 0.176 au. This mechanism is a capable test bed for further optimization of kinematic trajectories and force analysis.

4 KINEMATIC OPTIMIZATION OF A FLAPPING WING MODEL USING BOX-BEHNKEN SCREENING DESIGN AND RESPONSE SURFACE METHODOLOGY

A flapping mechanism created as a test bed for force analysis and optimization was described in Chapter 3. In this chapter, the search for optimal flapping trajectories is explored using two methods: (1) using a Box-Behnken screening design as an iterative approach, and (2) using a Box-Behnken design for the construction and gradient-based optimization of a response surface.

4.1 Introduction

Previous studies have been mentioned in which a mechanism was optimized to perform or execute a specific kinematic path (see Section 1.1.2). The optimization performed in this chapter did not aim to execute a specific trajectory but aimed to explore various trajectories and optimize the kinematics for maximum lift and thrust output.

This process of kinematic optimization will allow for more efficient MAVs that are capable of greater amounts of aerodynamic force. Thomson et al. [22], Bandyopadhyay et al. [24], and Boria et al. [23] have used mechanisms for hardware-in-the-loop studies. In these studies they sought to evaluate aerodynamic forces and then intelligently choose new test parameters in real time. The purpose of this chapter is to describe and present data for two similar approaches that could be used for hardware-in-the-loop force optimization.

4.2 Methods

4.2.1 Box-Behnken Screening Design

The Box-Behnken screening design (BBD) is an efficient method for exploring model design space [90]. In this study, the change in 15 parameters was explored. Using conventional factorial design of experiments methodology (such as a central composite design, CCD), a complete exploration would require more than 32,000 tests. The Box-Behnken screening design only requires 432. There are, however, disadvantages to the Box-Behnken design. The Box-Behnken only tests lower order interactions, higher order interactions are not considered. Further, the Box-Behnken design is a *spherical* design and not a *cuboidal* design in that it does not explore the extremes of the system (see Figure 4-1) [92]. Acknowledging these limitations, the Box-Behnken design was chosen based on its relatively low cost (run count).

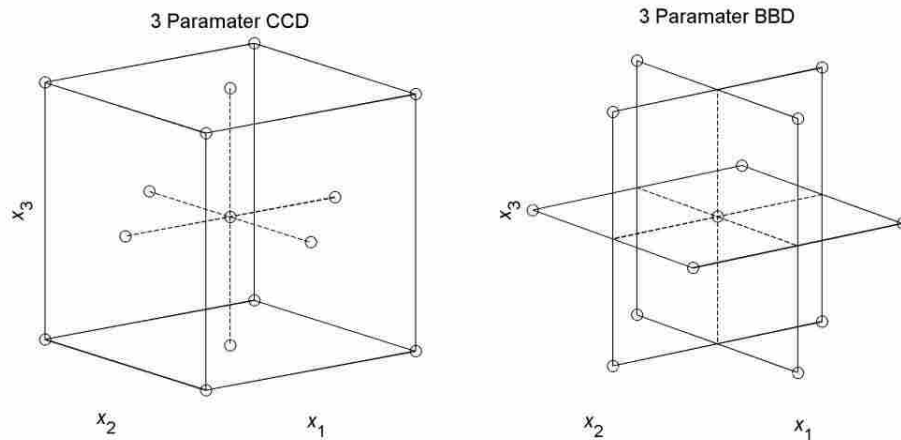


Figure 4-1. A central composite design tests the extremes of the system where a Box-Behnken design only tests the edges.

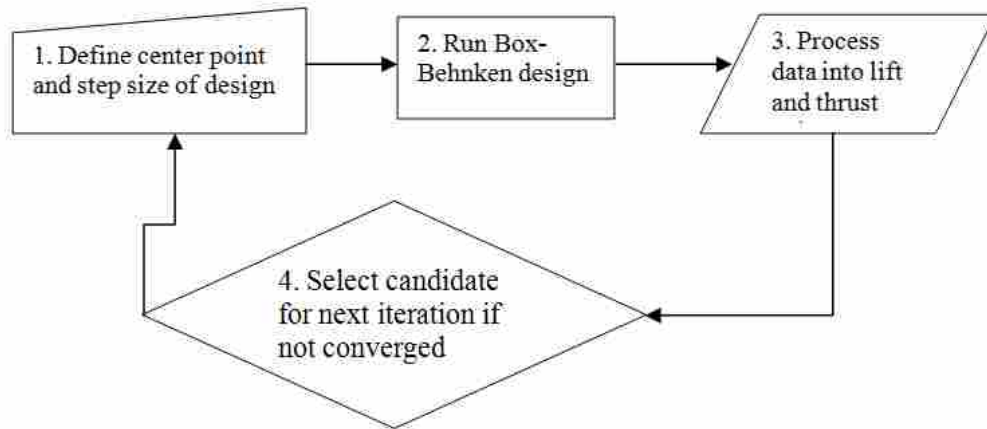


Figure 4-2. Flowchart describing the Box-Behnken design optimization strategy.

4.2.2 Response Surface Optimization

The Box-Behnken design is an efficient design for fitting second-order response surfaces. For the studies presented in this chapter, a 15-dimensional surface based on all 15 input parameters was used. This surface was of the form

$$f(\bar{x}) = A + B\bar{x} + \bar{x}^T C\bar{x}, \quad (4-3)$$

where

$$\bar{x} = [A_{11}, A_{12}, A_{13}, A_{14}, A_{15}, A_{21}, A_{22}, A_{23}, A_{24}, A_{25}, A_{31}, A_{32}, A_{33}, A_{34}, A_{35}], \quad (4-4)$$

$$A = \beta_0, \quad (4-5)$$

$$B = [\beta_1; \beta_2; \beta_3; \beta_4; \beta_5; \beta_6; \beta_7; \beta_8; \beta_9; \beta_{10}; \beta_{11}; \beta_{12}; \beta_{13}; \beta_{14}; \beta_{15}], \quad (4-6)$$

and

$$C = \begin{bmatrix} \beta_{11} & \frac{\beta_{1,2}}{2} & \frac{\beta_{1,3}}{2} & \dots & \frac{\beta_{1,n}}{2} \\ \frac{\beta_{2,1}}{2} & \beta_{22} & \frac{\beta_{2,3}}{2} & \dots & \frac{\beta_{2,n}}{2} \\ \frac{\beta_{3,1}}{2} & \frac{\beta_{3,2}}{2} & \beta_{33} & \dots & \frac{\beta_{3,n}}{2} \\ \vdots & \vdots & \vdots & \ddots & \vdots \\ \frac{\beta_{n,1}}{2} & \frac{\beta_{n,2}}{2} & \frac{\beta_{n,3}}{2} & \dots & \beta_{nn} \end{bmatrix}. \quad (4-7)$$

β values were found by performing regression statistics on the lift and thrust data, independently, and n was the number of system input parameters (15).

Two surfaces describing both lift and thrust were created using this method. Next, a gradient based optimization technique was used to maximize lift and thrust on each surface simultaneously using the function

$$f = \phi f_L(\bar{x}) + (1 - \phi) f_T(\bar{x}), \quad (4-8)$$

where ϕ was varied from 0 to 1 in increments of 0.01. Subject to

$$\max f \text{ such that } \begin{cases} \theta_1(\max) \leq 90^\circ \\ \theta_1(\min) \geq -90^\circ \\ \theta_2(\max) \leq 55^\circ \\ \theta_2(\min) \geq -105^\circ \\ \theta_3(\max) \leq 180^\circ \\ \theta_3(\min) \geq -180^\circ \\ radius \leq \sqrt{2} \end{cases}. \quad (4-9)$$

Care was taken during the optimization to ensure that the search algorithm did not allow the optimization to search outside the feasible design space based on hardware limits. To accomplish this, upper and lower limits for θ_{1d} , θ_{2d} , and θ_{3d} were set. Additionally, since the Box-Behnken does not predict the response at the corners of the design well, a limiting search radius of $\sqrt{2}$ was specified. If the Pareto front of the multi-objective optimization is non-convex, the search algorithm might find a solution which does not equally maximize both lift and thrust.

Adjusting ϕ values from 0 to 1 allowed the Pareto front to populate with feasible solutions and then allowed the user to choose a solution which best fit the optimization criteria. The Pareto frontier was then filtered using an s-Pareto filter [93].

Lift and thrust values from the surface optimization were then validated experimentally by executing their trajectories on the flapping mechanism and recording force output. The optimized path that best maximized lift and thrust was then chosen as the new center-point for the subsequent optimization. This process was repeated, iteratively, until the objective ceased to improve or the mechanism reached some active constraint of the hardware. Figure 4-3 shows a flowchart of this process.

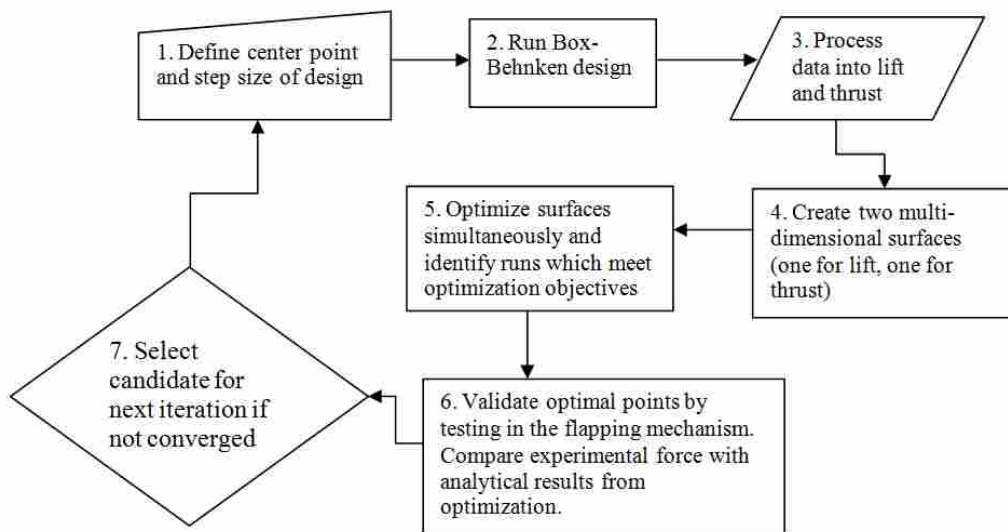


Figure 4-3. Flowchart of the Box-Behnken response surface optimization method.

4.3 Results

4.3.1 Box-Behnken Screening Design

The Box-Behnken screening design was performed using arbitrary Fourier-series coefficients as a starting point. The run of the Box-Behnken design that maximized both lift and thrust of the force output was selected as the new center point. The step size of the Box-Behnken design was cut in half and re-run. This iterative technique was repeated until the objective converged.

Figure 4-4 shows resulting forces for five iterations. Figure 4-5 compares the starting point of the Box-Behnken design with the force output of the best run from each iteration. Lift and thrust values from the best run of each iteration were calculated by identifying the best run and then re-running the trajectory 12 times and averaging the lift and thrust values from all 12 runs. The uncertainty of the force measurements (described in Section 3.4.3) caused some optimal values to deviate from their original value after being re-run 12 times and averaged. This is evident in iteration 4. The lift value was improved from iteration 3 to 4, but the thrust value decreased. This uncertainty was more evident as the improvement in the objective function decreased with each iteration.

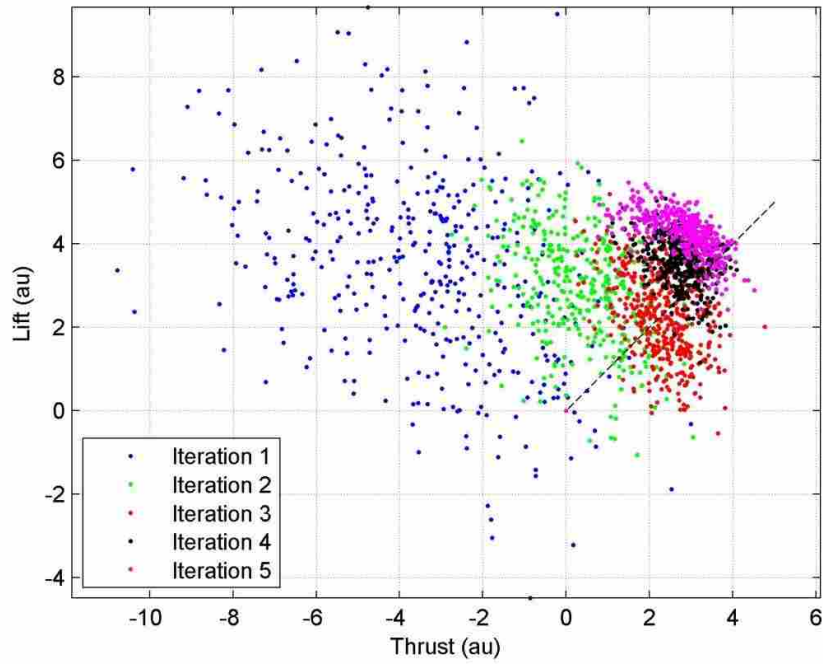


Figure 4-4. Box-Behnken design iteration performed five times starting from an arbitrary flapping trajectory.

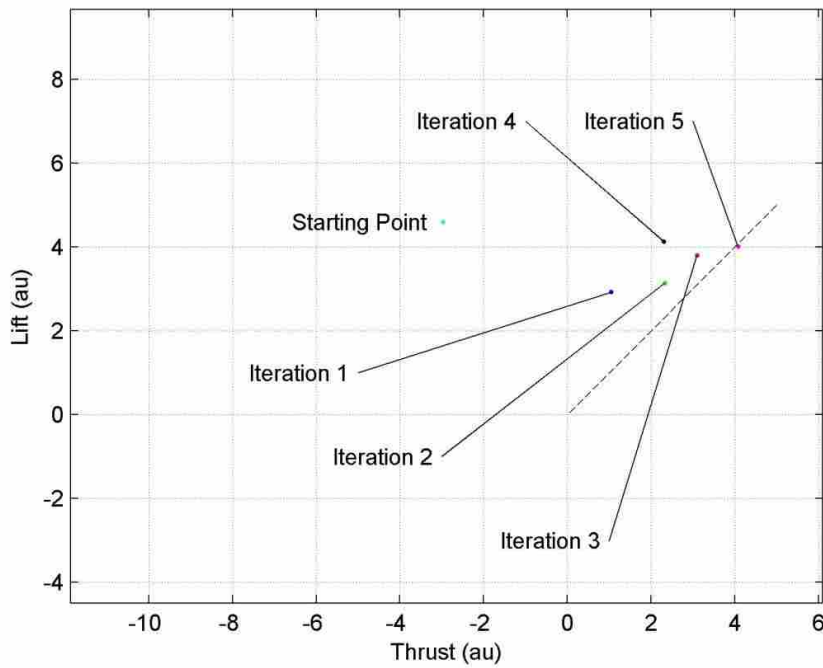


Figure 4-5. Progression of Box-Behnken design optimization starting from an arbitrary flapping trajectory.

Table 4-1. Kinematic coefficients for the starting point and the best runs of each iteration using arbitrary starting point kinematics. Bolded numbers represent an update in the kinematic coefficient from the optimization.

	Starting Point (°)	Iteration 1 (°)	Iteration 2 (°)	Iteration 3 (°)	Iteration 4 (°)	Iteration 5 (°)
A ₁₁	0	24	24	24	24	24
A ₁₂	50	50	50	50	50	50
A ₁₃	0	0	0	0	0	0
A ₁₄	0	0	0	0	0	0
A ₁₅	0	0	0	0	-4	-4
A ₂₁	-20	-20	-20	-20	-20	-20
A ₂₂	40	40	40	48	48	48
A ₂₃	0	0	0	-8	-8	-8
A ₂₄	0	32	32	32	32	34
A ₂₅	0	0	16	16	16	16
A ₃₁	0	0	0	0	0	0
A ₃₂	0	0	0	0	0	0
A ₃₃	45	45	45	45	41	41
A ₃₄	0	0	0	0	0	0
A ₃₅	0	0	16	16	16	18

Table 4-2. Step size progression of the Box-Behnken optimization for each iteration.

	Iteration 1 (°)	Iteration 2 (°)	Iteration 3 (°)	Iteration 4 (°)	Iteration 5 (°)
A ₁₁	24	12	6	3	1.5
A ₁₂	32	16	8	4	2
A ₁₃	32	16	8	4	2
A ₁₄	32	16	8	4	2
A ₁₅	32	16	8	4	2
A ₂₁	24	12	6	3	1.5
A ₂₂	32	16	8	4	2
A ₂₃	32	16	8	4	2
A ₂₄	32	16	8	4	2
A ₂₅	32	16	8	4	2
A ₃₁	24	12	6	3	1.5
A ₃₂	32	16	8	4	2
A ₃₃	32	16	8	4	2
A ₃₄	32	16	8	4	2
A ₃₅	32	16	8	4	2

Table 4-1 lists the Fourier coefficients of the starting point and the best run from each iteration as described in Equation 3-3. Table 4-2 lists the step sizes used throughout this optimization run

It is notable that the flapping trajectory found in iteration 5 was one that allowed the wings to clap together at the top of the flapping stroke and then fling apart, showing similarity to flapping trajectories found in nature. Figure 4-6 shows a time history of the force output of this flapping trajectory overlaid with several snapshots of the mechanism while executing the path.

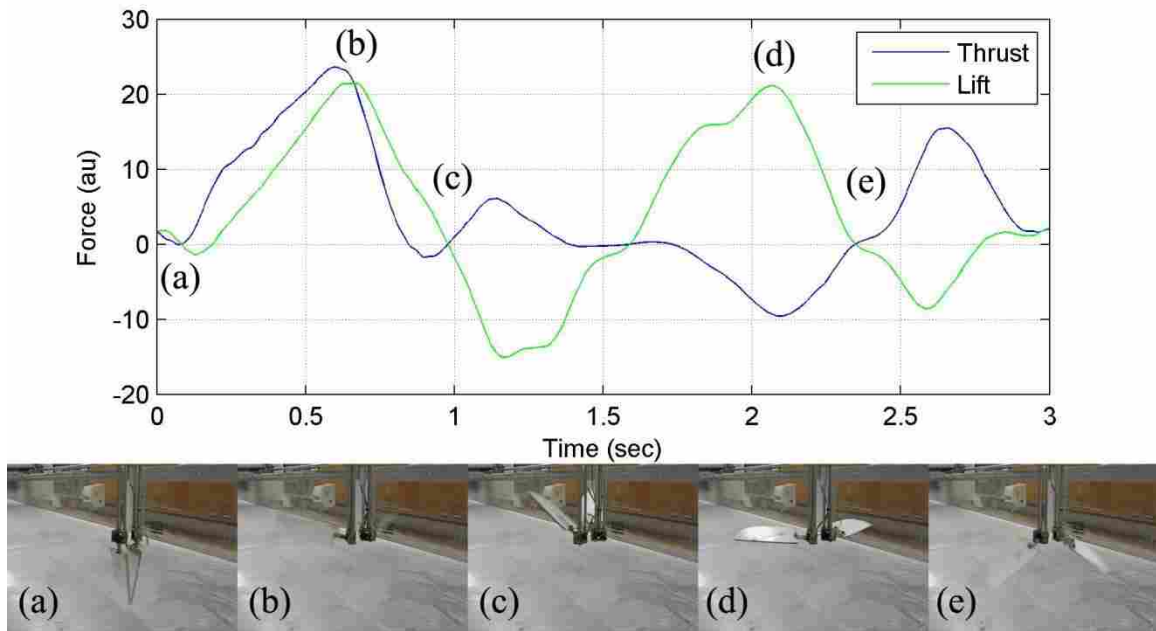


Figure 4-6. Force history of best run from Box-Behnken design starting from an arbitrary flapping trajectory.

The previous test was repeated but using kinematics of a zebra finch, as defined by Tobalske et al. [88], to guide the selection of the starting point. Tobalske [88] defined a relatively large elevation angle of $\approx 90^\circ$. The mechanism was not capable of executing such large amplitudes; therefore, the kinematics were simplified to allow the mechanism to physically be

capable of executing the trajectory and to allow the Box-Behnken design to explore a large range of trajectories without exceeding the mechanism's capabilities.

Figure 4-7 shows resulting forces for four iterations. Figure 4-8 compares the starting point of the Box-Behnken design with the force output of the best run from each iteration. Table 4-3 defines the Fourier coefficients of each iteration as described in Equation 3-3. The same step size was used as defined in Table 4-2. Figure 4-9 shows a time history of the force output of this flapping trajectory overlaid with several snapshots of the mechanism while executing the path.

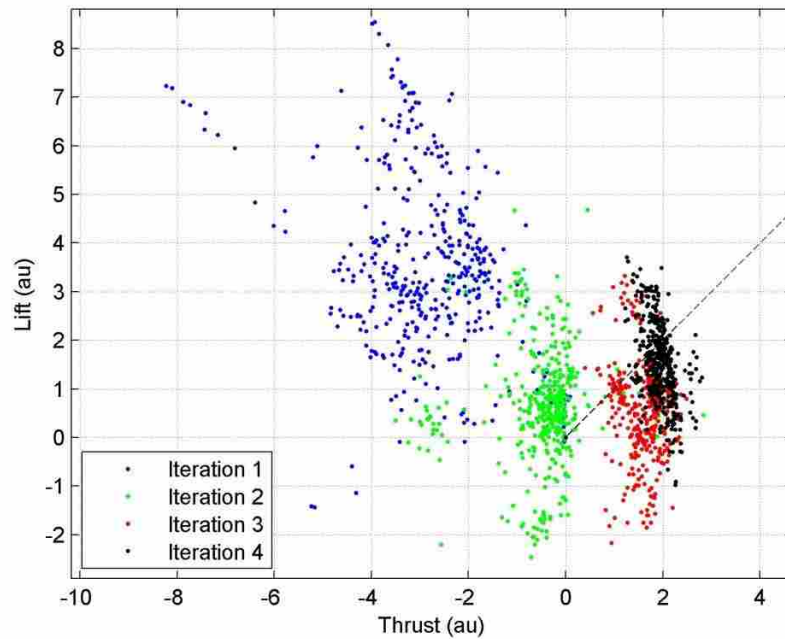


Figure 4-7. Box-Behnken design iteration performed four times starting from simplified zebra finch flapping kinematics.

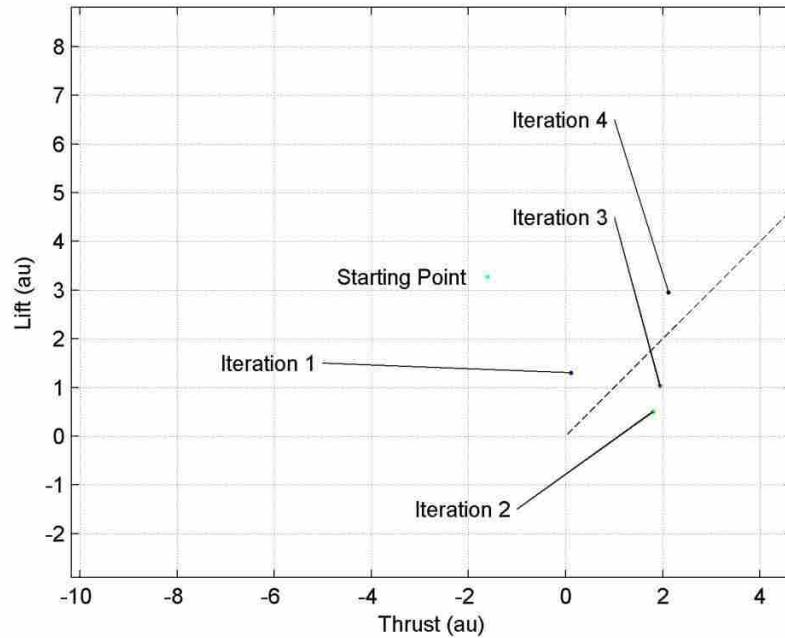


Figure 4-8. Progression of Box-Behnken design optimization starting from simplified zebra finch flapping kinematics.

Table 4-3. Kinematic coefficients for the starting point and best runs of each iteration using zebra finch starting point kinematics. Bolded numbers represent an update in the kinematic coefficient from the optimization.

	Starting Point (°)	Iteration 1 (°)	Iteration 2 (°)	Iteration 3 (°)	Iteration 4 (°)
A_{11}	0	0	0	0	0
A_{12}	0	0	0	0	0
A_{13}	0	0	0	0	0
A_{14}	0	0	0	0	0
A_{15}	0	0	0	0	0
A_{21}	0	0	0	0	0
A_{22}	10	10	10	10	10
A_{23}	0	0	16	16	16
A_{24}	0	0	0	0	4
A_{25}	0	32	32	32	36
A_{31}	-26	-2	-2	-8	-8
A_{32}	0	0	0	0	0
A_{33}	0	0	0	0	0
A_{34}	0	0	-16	-24	-24
A_{35}	0	0	0	0	0

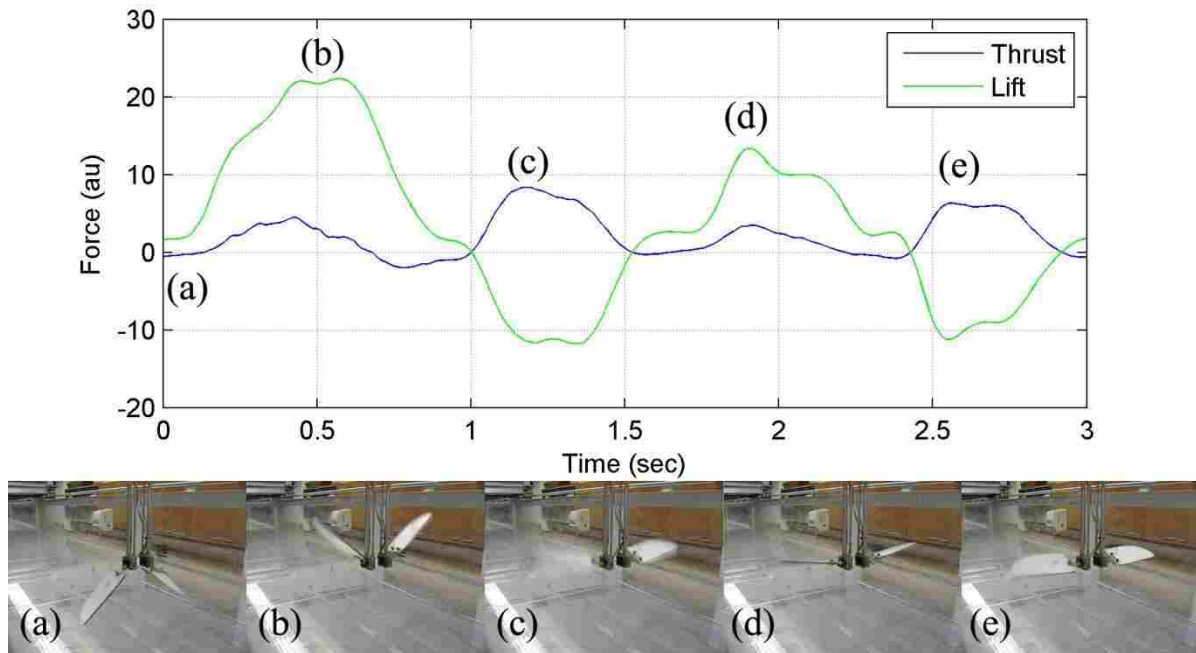


Figure 4-9. Force history of best run from Box-Behnken design starting from simplified zebra finch kinematics.

The lift and thrust output of the mechanism using a zebra finch as a starting point did not reach the same magnitude as the optimization that started from an arbitrary flapping trajectory. The Box-Behnken design optimization was not capable of finding a global maximum as the design is limited to selecting only specific trajectories tested during each iteration. A Box-Behnken design coupled with response surface methodology will allow interpolation and enable gradient-based optimization to search for trajectories within the limits of the mechanism with the goal of maximizing the objectives.

4.3.2 Response Surface Optimization

A response surface was created using the resulting force output from the Box-Behnken design. This was first performed using data from the first iteration of the Box-Behnken design

using an arbitrary flapping trajectory. The surface was optimized to maximize lift and thrust using `fmincon` in MATLAB (see Appendix C.4). The set of optimal coefficients was validated experimentally using the flapping hardware. Figure 4-10 shows resulting forces for two iterations. Figure 4-11 shows each iteration plotted with both its analytical and experimental Pareto front. As the step size decreased, the response surface was more capable of accurately predicting optimal force outputs. The error in the force measurements decreased substantially from iteration 1 to iteration 2 as seen in Figure 4-11.

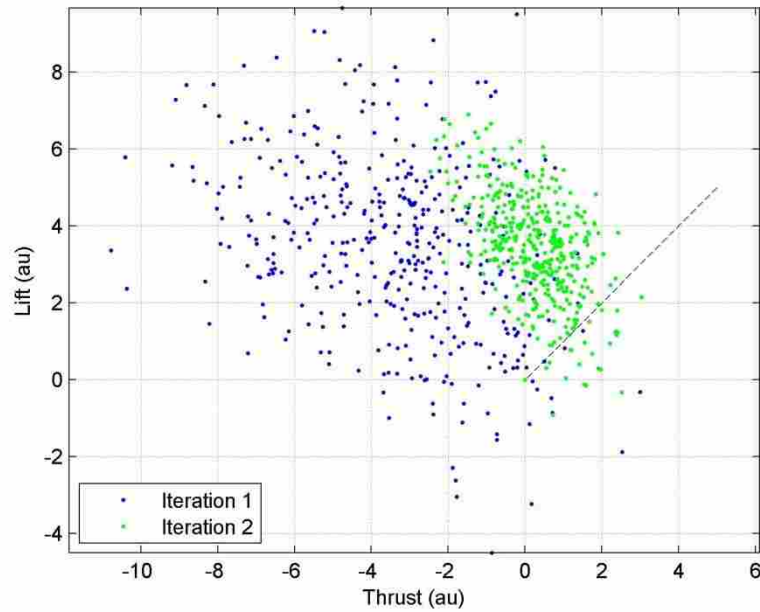


Figure 4-10. Lift and thrust forces for all runs from the response surface optimization using an arbitrary starting trajectory. Dashed line indicates search direction.

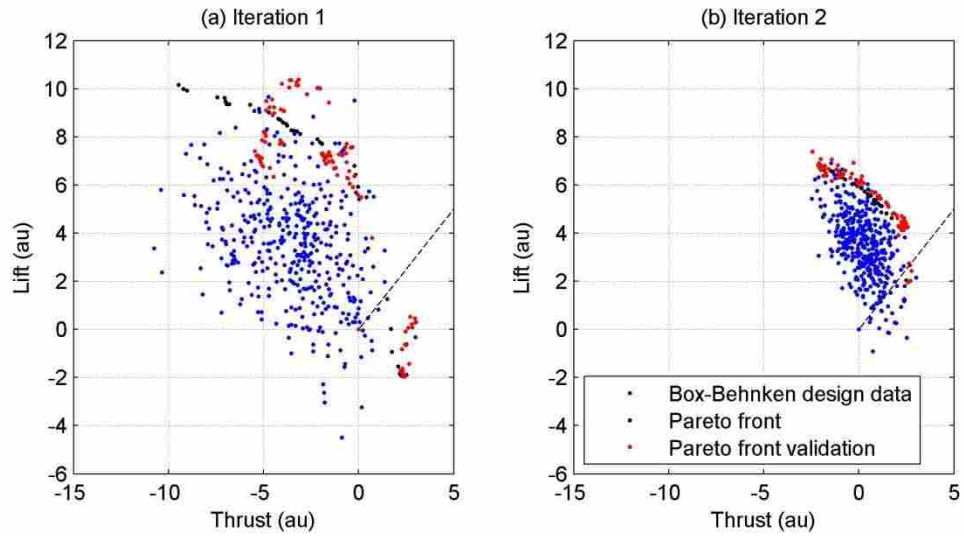


Figure 4-11. Experimental and analytical Pareto front shown for (a) iteration 1 and (b) iteration 2. Dashed line indicates search direction.

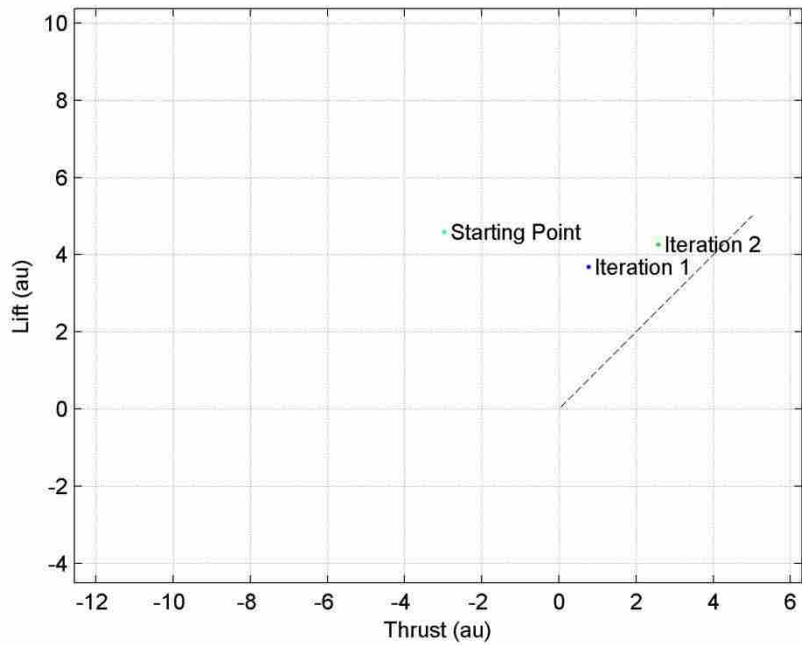


Figure 4-12. Best runs from gradient-based optimization starting from an arbitrary flapping trajectory. Dashed line indicates search direction.

Table 4-4. Kinematic coefficients for the starting trajectory and best runs from gradient-based optimization using an arbitrary starting point.

	Starting Point (°)	Iteration 1 (°)	Iteration 2 (°)
A₁₁	0	23	23
A₁₂	50	49	49
A₁₃	0	0	0
A₁₄	0	16	16
A₁₅	0	0	0
A₂₁	-20	-18	-18
A₂₂	40	39	55
A₂₃	0	0	0
A₂₄	0	11	27
A₂₅	0	0	0
A₃₁	0	1	1
A₃₂	0	0	0
A₃₃	45	44	44
A₃₄	0	0	0
A₃₅	0	0	0

Only two iterations were performed for this optimization. After the second iteration the mechanism reached an active constraint of mechanical limits and further optimization was not possible. Figure 4-12 shows the best runs from the optimization. Table 4-4 indicates the kinematic coefficients for the starting point and best runs of each iteration. Step sizes were the same used as in Table 4-2.

Figure 4-13 shows a time history of the force output of this flapping trajectory overlaid with several snapshots of the mechanism while executing the path.

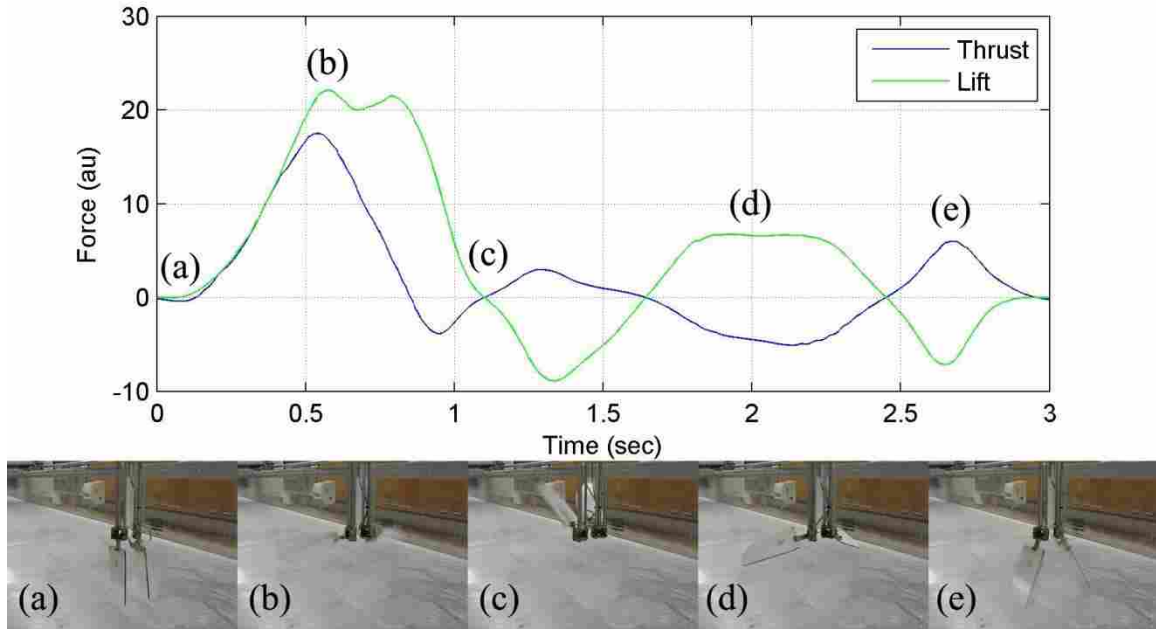


Figure 4-13. Force history from best run of response surface optimization starting from arbitrary flapping kinematics.

The previous optimization was again run using the kinematics of a zebra finch as a starting point. Figure 4-14 shows the resulting forces for three iterations. Figure 4-15 plots each iteration with its experimental and analytical Pareto front. Again in this case, as the size of the design space decreased, the response surface was more capable of accurately modeling the response of the system. Figure 4-16 shows the best runs from each optimization plotted against each other. Table 4-5 shows the updates in kinematic coefficients throughout the optimization. The step sizes used for this optimization were the same as in Table 4-2. Figure 4-17 shows a time history of the force output of this flapping trajectory overlaid with several snapshots of the mechanism while executing the path.

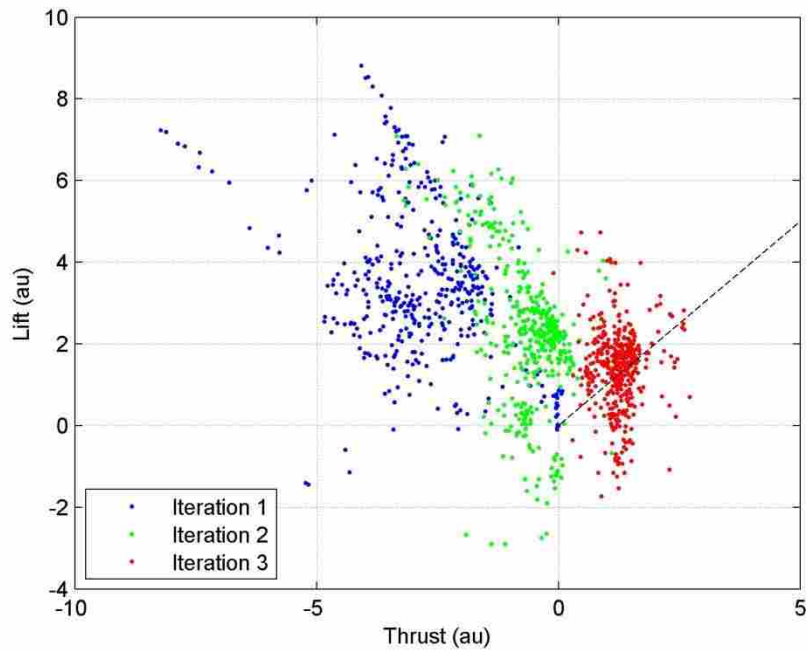


Figure 4-14. Lift and thrust forces for all runs from the response surface optimization using simplified zebra finch kinematics. Dashed line indicates the search direction.

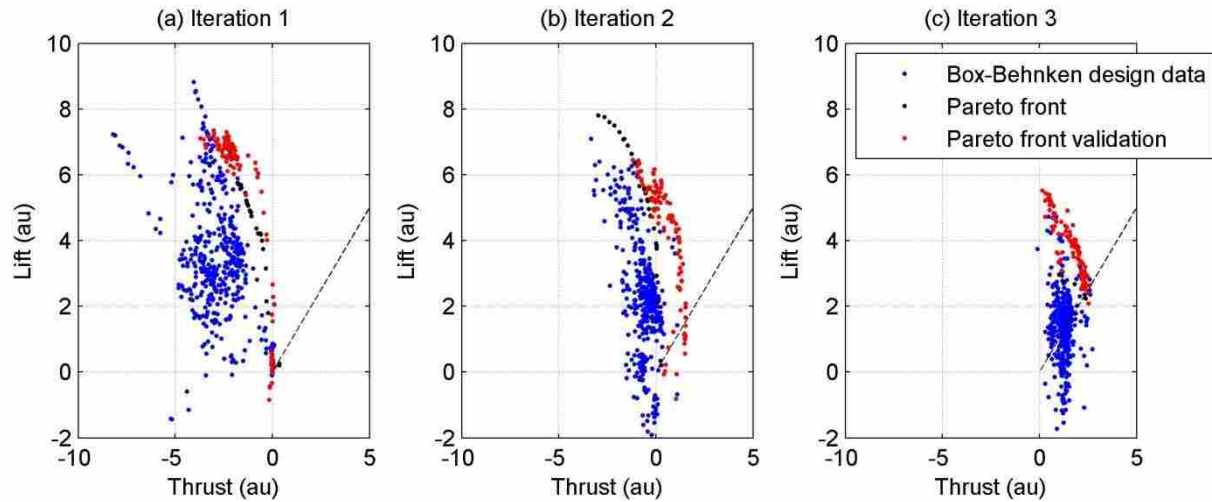


Figure 4-15. Experimental and analytical Pareto front shown for (a) iteration 1, (b) iteration 2, and (c) iteration 3. Dashed line indicates search direction.

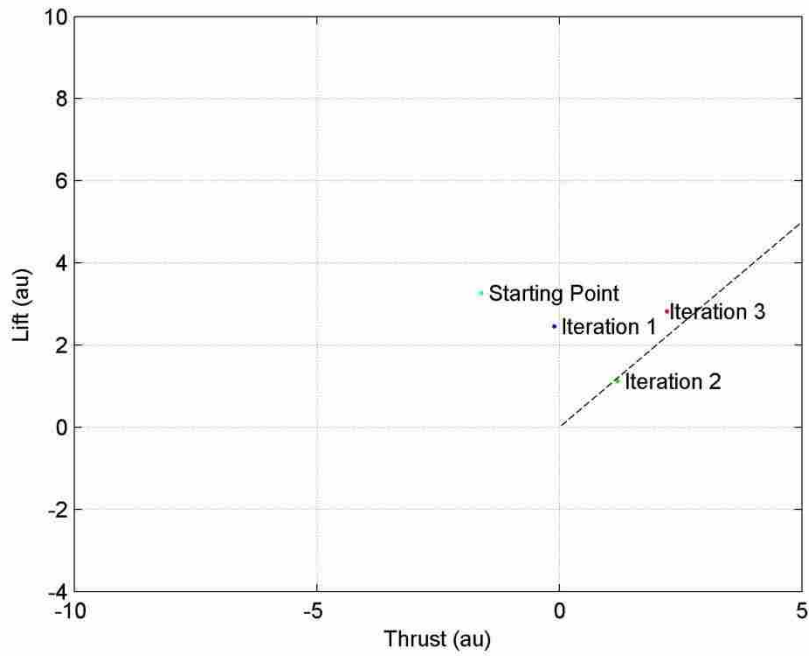


Figure 4-16. Best runs from gradient-based optimization starting from simplified zebra finch kinematics. Dashed line indicates search direction.

Table 4-5. Kinematic coefficients for the starting trajectory and best runs from gradient-based optimization using simplified zebra finch kinematics.

	Starting Point (°)	Iteration 1 (°)	Iteration 2 (°)	Iteration 3 (°)
A_{11}	0	0	0	0
A_{12}	0	0	0	0
A_{13}	0	0	0	0
A_{14}	0	-17	-20	-20
A_{15}	0	0	1	1
A_{21}	0	0	0	0
A_{22}	10	9	8	0
A_{23}	0	0	0	0
A_{24}	0	11	26	34
A_{25}	0	0	0	0
A_{31}	-26	-12	-9	-9
A_{32}	0	0	0	0
A_{33}	0	0	0	0
A_{34}	0	0	0	0
A_{35}	0	17	23	23

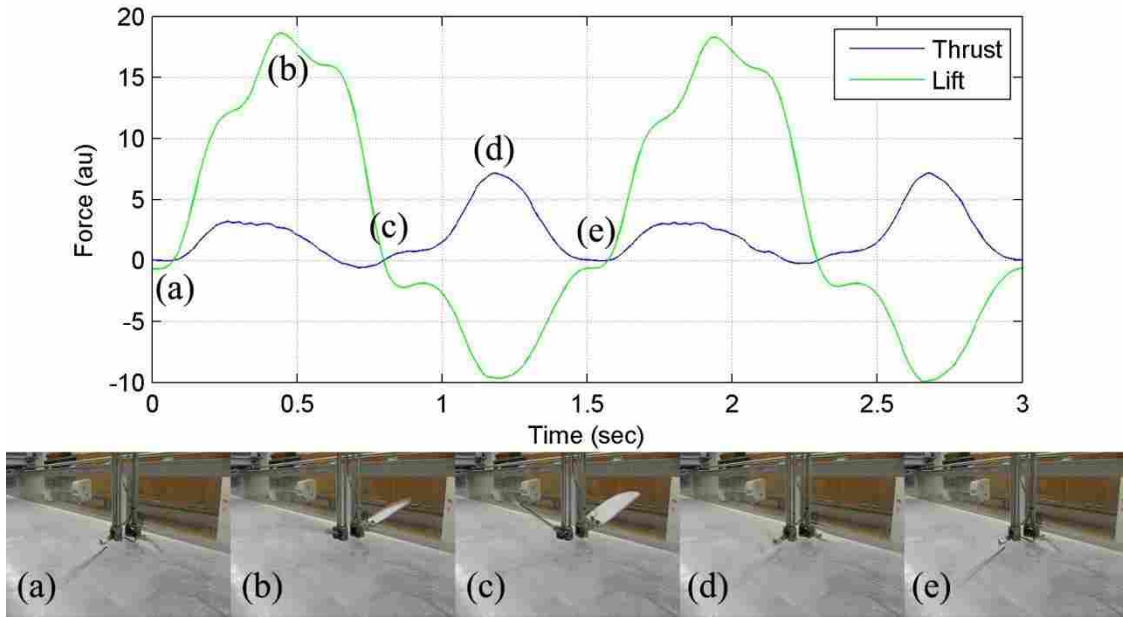


Figure 4-17. Force history from best run of response surface optimization using simplified zebra finch kinematics.

Both Box-Behnken design and response surface optimization methods were very capable of maximizing the objective functions. Table 4-6 shows the final lift and thrust results for all four tests.

Table 4-6. Resulting forces summary for all four optimizations.

	Arbitrary Starting Point			Zebra Finch Starting Point		
	Center Point	Box-Behnken	Box-Behnken with response surface	Center Point	Box-Behnken	Box-Behnken with response surface
Thrust	-2.7929	4.0739	2.5792	-1.6123	2.1197	2.2154
Lift	4.5949	4.0101	4.2693	3.2695	2.957	2.8173

Although the Box-Behnken design method using an arbitrary starting point had the maximum lift and thrust, it was more costly in that it took five iterations to converge on that

value. The response surface using an arbitrary starting point was capable of similar lift and thrust, but only took 2 iterations to complete. Both tests starting from a zebra finch kinematics did not converge to similar values as the tests that started from arbitrary starting points. This indicates that not only is the starting point important for converging on an optimal solution when using any Box-Behnken based optimization methodology, but also that the Box-Behnken methodology is not capable of finding a global optimum from this large, complex design space.

4.4 Conclusion

The methods described in this chapter demonstrated two techniques for optimizing the kinematics of a flapping wing mechanism with the purpose of maximizing both lift and thrust. The Box-Behnken design optimization approach successfully increased both lift and thrust substantially, but this approach was limited as it only tested first-order interactions and only allowed for discrete changes in each variable. The Box-Behnken response surface coupled with a gradient-based optimization proved to be an efficient method, but, again, the design was limited in part because the Box-Behnken was not good at predicting the system response at the variable extremes.

The results showed Box-Behnken design sensitivity to the starting point for optimization. A good starting point allowed the Box-Behnken design to quickly find an improved path, but when a poor starting point was chosen, the Box-Behnken did not lead to similar values.

The response surface had advantages of not being confined to discrete adjustments in the kinematics; however, it was limited in that when active constraints limited the system, the optimization method could not continue. Results, however, from the response surface appeared to be capable of more quickly attaining optimal values. As the size of the response surface

decreased, the correlation of experimental values with predictions based on the response surface improved.

Both Box-Behnken design and response surface methodology were algorithms capable of exploring regions of the parameter space effectively and quickly. Tests of these two methods constitutes a brief exploration into the kinematic optimization of this flapping wing mechanism.

5 CONCLUSIONS

The research described in this thesis has been conducted to further our understanding of insect flight by studying ladybugs during takeoff, to build an analogous mechanism which is capable of simulating wing kinematics of ladybugs and of other species, and to use this mechanism to investigate methods of optimizing wing kinematic trajectories for maximizing lift and thrust.

5.1 High-Speed Kinematic Quantification of Ladybugs (*Hippodamia Convergens*) During Takeoff

5.1.1 Conclusions

Flapping-wing kinematics of a ladybug during takeoff were analyzed using high-speed stereoscopic imaging at 3000 frames per second. Using a direct linear transfer, data in these video images were converted to 3-dimensional Cartesian coordinates for graphical representation of ladybug kinematics. The amplitude of the hindwing was found to be significantly larger than that of the forewing, but the forewing still flaps with significant amplitude. The ladybug flapping frequency was 78.6 Hz and the ladybug traveled at an average velocity of 21.4 cm/s during takeoff. The results presented in this chapter could aid in our understanding of insect flight and help in the development of experimental models for aerodynamics studies.

5.1.2 Future Work

Greater understanding of ladybug flapping flight can be achieved by studying the aerodynamics involved with the associated kinematics found in this chapter. Methods such as smoke wire visualization or particle image velocimetry can assist in understanding the lift-generating mechanisms involved in ladybug flight. Further, a Fourier-series based kinematic representation could be used as a starting point for optimization using a flapping wing mechanism. Lift and thrust estimates of the ladybug would allow comparison of measured ladybug forces with those acquired from experimental studies.

5.2 Design of a Differential-Driven Flapping-Wing Mechanism for Force Analysis and Optimization

5.2.1 Conclusions

A flapping wing mechanism was designed to be capable of flapping with a large range of motion and replicating the flapping wing kinematics of a ladybug or of other species. The design was based on a differential gear design using two gears as the input and one gear as the output. The output gear had 2 DOFs, and the third DOF was achieved by rotation about a turntable. This mechanism was capable of measuring lift and thrust of the wing and could operate in harsh environments such as in water or oil. The kinematics of the system were based on the first five terms of a Fourier-series expansion using the coefficients of the series as variables. Repeated force values measurements from the mechanism were consistent. A Box-Behnken screening design was used as a method of exploring the design space of the mechanism. Measurements showed trajectories with increased lift and thrust over initially selected trajectories.

5.2.2 Future Work

The design of the flapping mechanism is unique in that it provides feedback control via encoders, has two wings which allows for the exploration of phenomena such as clap-and-fling, and can accept a large range of kinematic inputs. It does, however, have its limitations. The θ_2 DOF is limited to 55° in its positive direction. This limits the range of feasible solutions that can be found with the mechanism. Further design of the mechanism to extend the range of motion of θ_2 would remove this limitation.

The force sensor on the mechanism works in bending only. Although the sensor functions properly in both air and water, the bending sensor is not capable of calibration due to the fact that the center of pressure on the wing is always changing as the wing executes its trajectory. The implementation of a shear force sensor instead of a bending moment sensor would enable calibration measurements to be taken and give the ability to directly correlate them with other systems.

5.3 Kinematic Optimization of a Flapping Wing Model Using Box-Behnken Screening Design and Response Surface Methodology

5.3.1 Conclusions

Two methods of optimizing flapping wing kinematics to maximize lift and thrust were presented in this section. The first used a Box-Behnken design to search the design space and select new kinematic coefficients. The method was then repeated using a smaller search size (step size) to narrow the range of valid parameters and converge on an optimal solution. The second method used the same Box-Behnken design, but coupled it with response surface methodology. A response surface was fit to measured data and, using a gradient-based

optimization technique, optimal values of lift and thrust were found. This second optimization technique was not subject to discrete changes in kinematic coefficients and converged more quickly on an optimal solution.

5.3.2 Future Work

The two methods of optimization mentioned in this chapter are possible optimization techniques that could be used with the flapping wing mechanism. Further exploration of other techniques, such as hardware-in-the-loop gradient based methods, genetic algorithms, and simulated annealing are just a few other methods that could be used in kinematic optimization studies.

All studies in this thesis were based on a Fourier-series expansion kinematics. Other methods of representing kinematics could be more successful in optimization or trajectory generation. Further investigation of alternative methods of representing kinematics could result in simple kinematic expressions and consequently less complex optimization.

5.4 Additional Work

The following are a few suggestions for future work related to this research that may be beneficial in understanding flapping flight and the development of MAVs:

- Flow visualization or PIV analysis on an optimal flapping trajectory found in this research could bring greater understanding of lift generating mechanisms and help us understand why the optimization algorithm converged on these kinematic paths.

- The studies in this thesis used adjustable step sizes in the application of the Box-Behnken design. Variations of this design could help in finding more optimal kinematics. Examples include using a smaller step size from the beginning, but keeping the step size constant throughout optimization.
- The current mechanism utilizes a first-in-first-out (FIFO) to send data from the PC to the FPGA. This transfer takes time (around 10 seconds) and hinders the user's ability to quickly test new generated paths. Further research into different control techniques could greatly improve the time required to test a trajectory and determine its feasibility.

REFERENCES

- [1] W Shyy, Y Lian, J Tang, D Viieru, and H Liu, *Aerodynamics of Low Reynolds Number Flyers*. Cambridge: Cambridge University Press, 2008.
- [2] M A Camper, "An Insect's Role in the Development of Micro Air Vehicles," Colorado State University, Fort Collins, CO,.
- [3] C P Ellington, C Van den Berg, A P Willmott, and A L R Thomas, "Leading-edge vortices in insect flight," *Nature*, vol. 384, no. 19, pp. 626-630, December 1996.
- [4] C P Ellington, "The Aerodynamics of Hovering Insect Flight," *Philosophical Transactions of the Royal Society London*, vol. 305, pp. 1-181, 1984.
- [5] C P Ellington, "The Novel Aerodynamics of Insect Flight: Applications to Micro-air Vehicles," *The Journal of Experimental Biology*, vol. 202, pp. 3439-3448, 1999.
- [6] R Zbikowski, "On aerodynamic modeling of an insect-like flapping wing in hover for micro air vehicles," *Philosophical Transactions of the Royal Society London*, vol. 360, pp. 273-290, 2002.
- [7] J M McMichael and Col. M S Francis. (1997, August) Micro Air Vehicles - Toward a New Dimension in Flight. [Online]. http://www.fas.org/irp/program/collect/docs/mav_aupsi.htm
- [8] C Van den Berg and C P Ellington, "The three-dimensional leading-edge vortex of a 'hovering' model hawkmoth," *Philosophical Transactions: Biological Sciences*, vol. 352, no. 1351, pp. 329-340, 1997.
- [9] S N Fry, R Sayaman, and M H Dickinson, "The aerodynamics of hovering flight in *Drosophila*," *The Journal of Experimental Biology*, vol. 208, pp. 2303-2318, 2005.
- [10] E I Fontaine, F Zabala, M H Dickinson, and J W Burdick, "Wing and body motion during flight initiation in *Drosophila* revealed by automated visual tracking," *The Journal of Experimental Biology*, vol. 212, pp. 1307-1323, 2009.

- [11] S M Walker, A L R Thomas, and G K Taylor, "Deformable wing kinematics in free-flying hoverflies," *Journal of the Royal Society Interface*, vol. Published online, pp. 1-12, 2009, Published online.
- [12] A Azuma and T Watanabe, "Flight performance of a dragonfly," *The Journal of Experimental Biology*, vol. 137, pp. 221-252, 1988.
- [13] H Wang, L Zeng, and C Yin, "Measuring the body position, attitude and wing deformation of a free-flight dragonfly by combining a comb fringe pattern with sign points on the wing," *Measurement Science and Technology*, vol. 13, pp. 903-908, 2002.
- [14] X Tian et al., "Direct Measurements of the Kinematics and Dynamics of Bat Flight," in *36th AIAA Fluid Dynamics Conference*, San Francisco, CA, 2006, pp. 1-10.
- [15] T Hubel, N I Hristov, S M Swartz, and K S Breuer, "Time-resolved wake structure and kinematics of bat flight," *Experiments in Fluids*, vol. Published online, 2009.
- [16] S A Ansari et al., "Experimental investigation of some aspects of insect-like flapping flight aerodynamics for application to micro air vehicles," *Experiments in Fluids*, vol. 46, pp. 777-798, 2009.
- [17] S A Ansari, R Zbikowski, and K Knowles, "Aerodynamic modelling of insect-like flapping flight for micro air vehicles," *Progress in Aerospace Sciences*, vol. 42, pp. 129-172, 2006.
- [18] T Q Le, D Byun, Y H Yoo, J H Ko, and H C Park, "Experimental and Numerical Investigation of Beetle Flight," in *International Conference on Robotics and Biomimetics*, Bangkok, Thailand, 2009, pp. 234-239.
- [19] F O Lehmann, S P Sane, and M Dickinson, "The aerodynamic effects of wing-wing interaction in flapping wing insects," *The Journal of Experimental Biology*, vol. 208, pp. 3075-3092, 2005.
- [20] J M Birch and M H Dickinson, "The influence of wing-wake interactions on the production of aerodynamic forces in flapping flight," *The Journal of Experimental Biology*, vol. 206, pp. 2257-2272, 2003.
- [21] P Bai, E Cui, F Li, W Zhou, and B Chen, "A new bionic MAV's flapping motion based on fruit fly hovering at low Reynolds number," *Acta Mechanica Sinica*, vol. 23, pp. 485-493, 2007.
- [22] S L Thomson et al., "Experiment-Based Optimization of Flapping Wing Kinematics," in *47th AIAA Aerospace Sciences Meeting*, Orlando, FL, 2009, pp. 1-8.

- [23] F Boria, B Stanford, W Bowman, and P Ifju, "Evolutionary Optimization of a Morphing Wing with Wind Tunnel Hardware-in-the-Loop," in *47th AIAA Aerospace Sciences Meeting*, Orlando, FL, 2009, pp. 1-17.
- [24] P R Bandyopadhyay, D N Beal, and A Menozzi, "Biorobotic insights into how animals swim," *The Journal of Experimental Biology*, vol. 211, pp. 206-214, 2008.
- [25] Y I Abdel-Azez and H M Karara, "Direct Linear Transformation from Comparator Coordinates into Object Space Coordinates in Close-Range Photogrammetry," in *ASP/US Symposium on Close-Range Photogrammetry*, Falls Church, VA, 1971, pp. 1-18.
- [26] R Hartley and A Zisserman, *Multiple View Geometry in Computer Vision*. Cambridge: Cambridge University Press, 2003.
- [27] L Frantsevich, Z Dai, W Y Wang, and Y Zhang, "Geometry of elytra opening and closing in some beetles (Coleoptera, Polyphaga)," *The Journal of Experimental Biology*, vol. 208, pp. 3145-3158, 2005.
- [28] S A Combes and T L Daniel, "Flexural stiffness in insect wings. I. Scaling and the influence of wing venation," *The Journal of Experimental Biology*, vol. 206, pp. 2979-2997, 2003.
- [29] M J C Smith, "Simulating Moth Wing Aerodynamics: Towards the Development of Flapping-Wing Technology," *AIAA Journal*, vol. 34, pp. 1348-1355, 1996.
- [30] M J C Smith, "Wing-Drive Mechanism, Vehicle Employing Same, and Method for Controlling the Wing-Drive Mechanism and Vehicle Employing Same," Hardware 6206324, March 27, 2001.
- [31] M H Dickinson, F O Lehmann, and S P Sane, "Wing Rotation and the Aerodynamic Basis of Insect Flight," *Science*, vol. 284, pp. 1954-1960, June 1999.
- [32] R S Fearing et al., "Wing Transmission for a Micromechanical Flying Insect," in *International Conference on Robotics and Automation*, San Francisco, CA, 2000, pp. 1509-1516.
- [33] M Sitti, "PZT Actuated Four-Bar Mechanism with Two Flexible Links for Micromechanical Flying Insect Thorax," in *IEEE International Conference on Robotics and Automation*, 2001, pp. 3893-3900.
- [34] K D Frampton and M Goldfarb, "Passive Aeroelastic Tailoring for Optimal Flapping Wings," in *Conference on Fixed, Flapping and Rotary Winged Vehicles for Very Low Reynolds Numbers*, Notre Dame, IN, 2000.

- [35] T Pornsin-Sisirak et al., "MEMS Wing Technology for a Battery-Powered Ornithopter," in *13th IEEE International Conference on Micro Electro Mechanical Systems*, Miyazaki, Japan, 2000, pp. 799-804.
- [36] J Yan, R J Wood, and Z A, Agrawal, S K Khan, "Towards Flapping Wing Control for a Micromechanical Flying Insect," in *IEEE International Conference on Robotics and Automation*, New York, NY, 2001, pp. 3901-3908.
- [37] A Cox, D Monopoli, D Cveticanin, M Goldfarb, and E Garcia, "The Development of Elastodynamic Components for Piezoelectrically Actuated Flapping Micro-air Vehicles," *Journal of Intelligent Material Systems and Structures*, vol. 13, pp. 611-615, September 2002.
- [38] S Avadhanula, R J Wood, E Steltz, J Yan, and R S Fearing, "Lift Force Improvements for the Micromechanical Flying Insect," in *IEEE International Conference on Intelligent Robotics and Systems*, Las Vegas, NV, 2003, pp. 1350-1356.
- [39] J Yan and R S Fearing, "Wing Force Map Characterization and Simulation for the Micromechanical Flying Insect," in *IEEE International Conference on Intelligent Robots and Systems*, Las Vegas, NV, 2003, pp. 1343-1349.
- [40] D L Raney and E C Slominski, "Mechanization and Control Concepts for Biologically Inspired Micro Aerial Vehicles," in *AIAA Guidance, Navigation & Control Conference*, Austin, TX, 2003, pp. 1-11.
- [41] M J Tarascio and I Chopra, "Design and Development of a Thrust Augmented Entomopter: An Advanced Flapping Wing Micro Hovering Air Vehicle," in *59th Annual Forum of the American Helicopter Society*, Phoenix, AZ, 2003.
- [42] B Singh, M Ramasamy, I Chopra, and J G Leishman, "Experimental Studies on Insect-Based Flapping Wings for Micro Hovering Air Vehicles," *AIAA Journal*, vol. 46, pp. 2115-2135, 2008.
- [43] S C Burgess, K Alemzadeh, and L Zhang, "The development of a miniature mechanism for producing insect wing motion," *Design and Nature II*, pp. 237-244, 2004.
- [44] N D Mankame and G K Ananthasuresh, "A Novel Compliant Mechanism for Converting Reciprocating Translation Into Enclosing Curved Paths," *Journal of Mechanical Design*, vol. 126, pp. 667-672, July 2004.
- [45] W J Maybury and F O Lehmann, "The fluid dynamics of flight control by kinematic phase lag variation between two robotic insect wings," *The Journal of Experimental Biology*, vol. 207, pp. 4707-4726, 2004.

- [46] A L R Thomas, G K Taylor, R B Srygley, R L Nudds, and R J Bomphrey, "Dragonfly flight: free-flight and tethered flow visualizations reveal a diverse array of unsteady lift-generating mechanisms, controlled primarily via angle of attack," *The Journal of Experimental Biology*, vol. 207, pp. 4299-4323, 2004.
- [47] S K Banala and S K Agrawal, "Design and Optimization of a Mechanism for Out-of-Plane Insect Winglike Motion With Twist," *Journal of Mechanical Design*, vol. 127, no. 4, pp. 841-844, 2005.
- [48] C Galinski and R Zbikowski, "Insect-like flapping wing mechanism based on a double spherical Scotch yoke," *J. R. Soc. Interface*, vol. 2, pp. 223-235, 2005.
- [49] R Zbikowski, C Galinski, and C B Pedersen, "Four-Bar Linkage Mechanism for Insectlike Flapping Wings in Hover: Concept and an Outline of Its Realization," *Journal of Mechanical Design*, vol. 127, pp. 817-824, July 2005.
- [50] W Lai, J Yan, M Motamed, and S Green, "Force Measurements on a Scaled Mechanical Model of Dragonfly in Forward Flight," in *International Conference on Advanced Robotics*, 2005, pp. 595-600.
- [51] R Madangopal, Z A Khan, and S K Agrawal, "Biologically Inspired Design of Small Flapping Wing Air Vehicles Using Four-Bar Mechanisms and Quasi-steady Aerodynamics," *Journal of Mechanical Design*, vol. 127, pp. 809-816, July 2005.
- [52] R Madangopal, Z A Khan, and S K Agrawal, "Energetics-Based Design of Small Flapping-Wing Micro Air Vehicles," *IEEE/ASME Transactions on Mechatronics*, vol. 11, no. 4, pp. 433-438, 2006.
- [53] S H McIntosh, S K Agrawal, and Z Khan, "Design of a Mechanism for Biaxial Rotation of a Wing for a Hovering Vehicle," in *IEEE/ASME Transaction of Mechatronics*, 2006, pp. 145-153.
- [54] S K Agrawal, S H McIntosh, and Z Khan, "Mechanism for Biaxial Rotation of a Wing and Vehicle Containing Such Mechanism," Hardware 7651051, January 26, 2010.
- [55] H Tanaka, K Hoshino, K Matsumoto, and I Shimoyama, "Flight Dynamics of a Butterfly-type Ornithopter," in *International Conference on Intelligent Robots and Systems*, 2005, pp. 2706-2711.
- [56] M Yamamoto and K Isogai, "Measurement of unsteady fluid dynamic forces for a mechanical dragonfly model," *AIAA Journal*, vol. 43, no. 12, 2005.

- [57] A T Conn, S C Burgess, R Hyde, and C S Ling, "From Natural Flyers to the Mechanical Realization of a Flapping Wing Micro Air Vehicle," in *International Conference on Robotics and Biomimetics*, Kunming, China, 2006, pp. 439-444.
- [58] A T Conn, S C Burgess, and C S Ling, "Design of a parallel crank-rocker flapping mechanism for insect-inspired micro air vehicles," *Journal of Mechanical Engineering Science*, vol. 221, pp. 1211-1222, 2007.
- [59] K M Isaac, "Force Measurements on a Flapping and Pitching Wing at Low Reynolds Numbers," in *44th AIAA Aerospace Sciences Meeting*, Reno, NV, 2006, pp. 1-14.
- [60] M Syaifuddin, H C Park, and N S Goo, "Design and evaluation of a LIPCA-actuated flapping device," *Smart Materials and Structures*, vol. 15, pp. 1225-1230, 2006.
- [61] V Q Nguyen et al., "Characteristics of an Insect-mimicking Flapping System Actuated by a Unimorph Piezoceramic Actuator," *Journal of Intelligent Material Systems and Structures*, vol. 00, pp. 1-9, 2008.
- [62] C DiLeo and X Deng, "Experimental Testbed and Prototype Development for a Dragonfly-Inspired Robot," in *Conference on Intelligent Robots and Systems*, San Diego, CA, 2007, pp. 1594-1599.
- [63] Z A Khan and S K Agrawal, "Design and Optimization of a Biologically Inspired Flapping Mechanism for Flapping Wing Micro Air Vehicles," in *IEEE International Conference on Robotics and Automation*, Roma, Italy, 2007, pp. 373-378.
- [64] R J Wood, "Design, fabrication, and analysis of a 3DOF, 3cm flapping-wing MAV," in *IEEE International Conference on Intelligent Robots and Systems*, San Diego, CA, 2007, pp. 1576-1581.
- [65] L J Yang, C K Hsu, J Y Ho, and C K Feng, "Flapping wings with PVDF sensors to modify the aerodynamic forces of a micro air vehicle," *Sensors and Actuators*, vol. 139, pp. 95-103, 2007.
- [66] G Bunget and S Seelecke, "BATMAV: a biologically-inspired micro-air vehicle for flapping flight: kinematics and actuation," in *Proceedings of SPIE*, 2008.
- [67] C Grand, P Martinelli, J B Mouret, and S Doncieux, "Flapping-Wing Mechanism for a Bird-Sized UAVs: Design, Modeling and Control," *Advances in Robot Kinematics: Analysis and Design*, pp. 127-134, 2008.
- [68] D Lentink, F T Muijres, F Donker-Duyvis, and J L van Leeuwen, "Vortex-wake interactions of a flapping foil that models animal swimming and flight," *The Journal of Experimental Biology*, vol. 211, pp. 267-273, 2008.

- [69] J Maglasang, N Goto, and K Isogai, "Development of Bird-like Micro Aerial Vehicle with Flapping and Feathering Wing Motions," *Trans. Japan Soc. Aero. Space Sci.*, vol. 51, no. 171, pp. 8-15, 2008.
- [70] H Nagai, K Isogai, and T Hayase, "Measurement of Unsteady Aerodynamic Forces of 3D Flapping Wing in Hovering to Forward Flight," in *26th International Congress of the Aeronautical Sciences*, 2008, pp. 1-11.
- [71] J H Park and K J Yoon, "Designing a Biomimetic Ornithopter Capable of Sustained and Controlled Flight," *Journal of Bionic Engineering*, vol. 5, no. 1, pp. 39-47, 2008.
- [72] W Bejgerowski, A Ananthanarayanan, D Mueller, and S K Gupta, "Integrated Product and Process Design for a Flapping Wing Drive Mechanism," *Journal of Mechanical Design*, vol. 131, June 2009.
- [73] C T Bolsman, J F L Goosen, and F van Keulen, "Design Overview of a Resonant Wing Actuation Mechanism for Application in Flapping Wing MAVs," *International Journal of Micro Air Vehicles*, vol. 1, no. 4, pp. 263-272, 2009.
- [74] B M Finio, B Eum, C Oland, and R J Wood, "Asymmetric flapping for a robotic fly using a hybrid power-control actuator," in *Proceedings of the 2009 IEEE/RSJ international conference on Intelligent robots and systems*, St. Louis, MO, 2009, pp. 2755--2762.
- [75] T Y Hubel and C Tropea, "Experimental investigation of a flapping wing model," *Experiments in Fluids*, vol. 46, pp. 945-961, 2009.
- [76] R Y Krashanitsa, D Silin, and S V Shkarayev, "Flight Dynamics of a Flapping-Wing Air Vehicle," *International Journal of Micro Air Vehicles*, vol. 1, no. 1, pp. 35-49, 2009.
- [77] K Massey, A Flick, and G Jadhav, "Force Measurements and Flow Visualization for a Flexible Flapping Wing Mechanism," *International Journal of Micro Air Vehicles*, vol. 1, no. 3, pp. 183-202, November 2009.
- [78] B J Tsai and Y C Fu, "Design and aerodynamic analysis of a flapping-wing micro air vehicle," *Aerospace Science and Technology*, vol. 13, pp. 383-392, 2009.
- [79] M A A Fenelon and T Furukawa, "Design of an active flapping wing mechanism and a micro aerial vehicle using a rotary acuator," *Mechanism and Machine Theory*, vol. 45, pp. 137-146, 2010.
- [80] J Han and J W Chang, "Flow Visualization and Force Measurement of an Insect-based Flapping Wing," in *48th AIAA Aerospace Sciences Meeting*, Orlando, FL, 2010, pp. 1-10.

- [81] S Mukherjee and R Ganguli, "Non-linear Dynamic Analysis of a Piezoelectrically Actuated Flapping Wing," *Journal of Intelligent Material Systems and Structures*, vol. 21, pp. 1157-1167, August 2010.
- [82] R B Dryburgh, B G W Peter, and W G Plewes, "Waterproofing Strain Gages on Reinforcing Bars in Concrete Exposed to the Sea," *American Society for Testing and Materials - Materials Research and Standards*, vol. 5, no. 7, pp. 350-351, August 1965.
- [83] H Aono, W Shyy, and H Lui, "Near wake vortex dynamics of a hovering hawkmoth," *Acta Mech Sin*, vol. 25, pp. 23-36, 2009.
- [84] W Shyy et al., "Recent progress in flapping wing aerodynamics and aeroelasticity," *Progress in Aerospace Sciences*, vol. 46, pp. 284-327, 2010.
- [85] J J Craig, *Introduction to Robotics: Mechanics and Control*, 3rd ed.: Prentice Hall, 2004.
- [86] J M Birch and M H Dickinson, "Spanwise flow and the attachment of the leading-edge vortex on insect wings," *Nature*, vol. 412, pp. 729-733, 2001.
- [87] R B George and S L Thomson, "High-Speed, Three-Dimensional Quantification of Ladybug (*Hippodamia convergens*) Flapping Wing Kinematics During Takeoff," in *48th AIAA Aerospace Sciences Meeting*, Orlando, FL, 2010, pp. 1-11.
- [88] B W Tobalske, W L Peacock, and K P Dial, "Kinematics of flap-bounding flight in the zebra finch over a wide range of speeds," *The Journal of Experimental Biology*, vol. 202, pp. 1725-1739, 1999.
- [89] P Higgins, J Peter, and S Cowling, *Handbook of Australian, New Zealand and Antarctic Birds: Volume 7: Boatbills to Starlings*, Peter Higgins, John Peter, and Sid Cowling, Eds. USA: Oxford University Press, 2006.
- [90] G E P Box and D W Behnken, "Some New Three Level Designs for the Study of Quantitative Variables," *Technometrics*, vol. 2, no. 4, pp. 455-475, November 1960.
- [91] S L C Ferreira et al., "Box-Behnken design: An alternative for the optimization of analytical methods," *Analytica Chimica Acta*, vol. 597, pp. 179-186, 2007.
- [92] R H Myers and D C Montgomery, *Response Surface Methodology: Process and Product Optimization Using Designed Experiments*. New York, NY, USA: John Wiley & Sons, Inc., 1995.
- [93] C A Mattson and A Messac, "Concept Selection Using s-Pareto Frontiers," *AIAA Journal*, vol. 41, no. 6, pp. 1190-1198, 2003.

APPENDIX A. LADYBUG DLT FILES - MATLAB

MATLAB was used to analyze and record the flapping wing kinematics of a ladybug during flight. The following are files use for calibration and analysis of video data files.

A.1 Calibration

```
%%%%%%%%%%%%%%%%%%%%%%%%%%%%%%%%%%%%%%%%%%%%%%%%%%%%%%%%%%%%%%%%%%%%%%%%
%
%   Direct Linear Transformation
%   Created By: Ryan B. George
%   January 20, 2009
%   In conjunction with Dr. Scott L. Thomson
%   Flapping Flight Research Group
%
%%%%%%%%%%%%%%%%%%%%%%%%%%%%%%%%%%%%%%%%%%%%%%%%%%%%%%%%%%%%%%%%%%%%%%%%

%% House keeping

clc;
close all;
clear all;

%% Prompt user to specify input mode

%   0 = User Defined Calibration Points
%   1 = Hard Coded Calibration Points

%%Set this parameter to 0 or 1 depending on the desired calibration point
%%input method
method = 1;

%% Scheme to be used for when "method == 0"

if method == 0
    %%Enter number of calibration points
    points = input('Please enter the number of calibration points ');
    if points < 6
        disp('Error! Must have at least 6 calibration points!');
        while points < 6
            points = input('Please enter the number of calibration points
');
        end
    end

    %%Enter "X" direction coordinates of calibration points
    x = input('Please enter the "X" coordinates of the calibration points in
order ');
    if length(x) ~= points
        disp('Error! Must have matching number of "X" coordinates!');
        while length(x) ~= points
            x = input('Please enter the "X" coordinates of the calibration
points in order ');
        end
    end
end
```

```

end

%%%Enter "Y" direction coordinates of calibration points
y = input('Please enter the "Y" coordinates of the calibration points in
order ');
if length(y) ~= points
    disp('Error! Must have matching number of "Y" coordinates!');
    while length(y) ~= points
        y = input('Please enter the "Y" coordinates of the calibration
points in order ');
    end
end

%%%Enter "Z" direction coordinates of calibration points
z = input('Please enter the "Z" coordinates of the calibration points in
order ');
if length(z) ~= points
    disp('Error! Must have matching number of "Z" coordinates!');
    while length(z) ~= points
        z = input('Please enter the "Z" coordinates of the calibration
points in order ');
    end
end

end

end

%% Scheme to be used for when "method == 1"

if method == 1
    %%%Hard code calibration points here. Must be at least 6.
    load calibrate.txt;
    y = calibrate(:,1)';
    x = calibrate(:,2)';
    z = calibrate(:,3)';
    points = length(x);
    x = x*2.54;
    y = y*2.54;
    z = z*2.54;
end

%% Prompt User to pick calibration points on image

mov1=aviread('H:\Ladybugs\19 May 2009\Calibration\Calibration.avi');

A=mov1(10).cdata;

imagesc(A);
axis image;
colormap gray;

%%%Read in left points from calibration image
disp('Read in left points from calibration image. ');
[ul vl] = ginput(points);
Leftpoints = [ul vl];

%%%Read in right points from calibration image

```

```

disp('Read in right points from calibration image. ');
[ur vr] = ginput(points);
Rightpoints = [ur vr];
close;

%% Creation of F and G matrices based on calibration point input

%%F1 and Fr matrix creation

counter = 1;
for i=1:points
    Fl(counter,:) = [ x(i) y(i) z(i) 1 0 0 0 0 -ul(i)*x(i) -ul(i)*y(i) -
ul(i)*z(i) ]';
    Fr(counter,:) = [ x(i) y(i) z(i) 1 0 0 0 0 -ur(i)*x(i) -ur(i)*y(i) -
ur(i)*z(i) ]';
    counter = counter + 1;
    Fl(counter,:) = [ 0 0 0 0 x(i) y(i) z(i) 1 -vl(i)*x(i) -vl(i)*y(i) -
vl(i)*z(i) ]';
    Fr(counter,:) = [ 0 0 0 0 x(i) y(i) z(i) 1 -vr(i)*x(i) -vr(i)*y(i) -
vr(i)*z(i) ]';
    counter = counter + 1;
end

counter = 1;

%%G1 and Gr matrix creation

for i=1:points
    gl(counter) = ul(i);
    gr(counter) = ur(i);
    counter = counter +1;
    gl(counter) = vl(i);
    gr(counter) = vr(i);
    counter = counter +1;
end

%% Calculation of L and R

L = inv(Fl'*Fl)*Fl'*gl';
R = inv(Fr'*Fr)*Fr'*gr';

%% Calculate Goodness of Calibration

ActualCoordinates = [x' y' z'];
CalculatedCoordinates = [];
for i=1:points;
    Q = [[L(1)-L(9)*ul(i) L(2)-L(10)*ul(i) L(3)-L(11)*ul(i) ]
[L(5)-L(9)*vl(i) L(6)-L(10)*vl(i) L(7)-L(11)*vl(i) ]
[R(1)-R(9)*ur(i) R(2)-R(10)*ur(i) R(3)-R(11)*ur(i) ]
[R(5)-R(9)*vr(i) R(6)-R(10)*vr(i) R(7)-R(11)*vr(i)]];

    q = [[ul(i)-L(4)]
[vl(i)-L(8)]]
end

```

```

    [ur(i)-R(4)]
    [vr(i)-R(8)]];

    CalculatedCoordinates = [CalculatedCoordinates; (inv(Q'*Q)*Q'*q)'];
end

%% Calculate Error
AverageError = sum((sum((ActualCoordinates-CalculatedCoordinates)...
    .^2,2)).^(1/2))/(length(CalculatedCoordinates(:,1)))

%% Export Data for Use in Another Matlab File

%save LMatrix.txt L -ASCII -double
%save RMatrix.txt R -ASCII -double
%output=[L R];
%save output.txt output -ascii -double
save points ul vl ur vr L R ActualCoordinates CalculatedCoordinates -double

%% Plot Calibration Data in 3D

xa=ActualCoordinates(:,1);
ya=ActualCoordinates(:,2);
za=ActualCoordinates(:,3);
xc=CalculatedCoordinates(:,1);
yc=CalculatedCoordinates(:,2);
zc=CalculatedCoordinates(:,3);
plot3(xa, ya, za, '.', xc, yc, zc, '+')
grid on

```

A.2 Tracking Analysis

```
%%%%%%%%%%%%%%%%%%%%%%%%%%%%%%%%%%%%%%%%%%%%%%%%%%%%%%%%%%%%%%%%%%%%%%%%
%
% Ladybug Analysis
% Created By: Ryan B. George
% May 29, 2009
% In conjunction with Dr. Scott L. Thomson
% Flapping Flight Research Group
%
%%%%%%%%%%%%%%%%%%%%%%%%%%%%%%%%%%%%%%%%%%%%%%%%%%%%%%%%%%%%%%%%%%%%%%%%

%% House keeping

clc;
close all;
clear all;
%%Points on Ladybug to track
load points_rev04;
points = 1;
start = 330;%was 330
last = 331;%was 510

%% Load video file

mov1=aviread('C:\Users\Ryan Brandon George\Documents\Research - Masters\AIAA
Ladybug Stuff\Ladybug Videos\19 May 2009\Ladybug9\Ladybug9.avi');

BodyData1 = [];
BodyData2 = [];
RWingData = [];
RShellData = [];

%% Get user input graphical points

%for i=start:1:last;
    for i=1:1:(last-start);
        A=mov1(i+start).cdata;
        % Maximize figure in window
        fullscreen = get(0,'ScreenSize');
        % figure('Position',[0 -50 fullscreen(3) fullscreen(4)])
        imagesc(A);
        axis image;
        colormap gray;
        [ul(i) vl(i)] = ginput(points);
    % close;
    end

    for i=1:1:(last-start);
        A=mov1(i+start).cdata;
        % Maximize figure in window
        fullscreen = get(0,'ScreenSize');
        % figure('Position',[0 -50 fullscreen(3) fullscreen(4)])
```

```

    imagesc(A);
    axis image;
    colormap gray;
    [ur(i) vr(i)] = ginput(points);
%     close;
    end

%% Use DLT to find x,y,z coordinates

    for i=1:(last-start);
    Q = [[L(1)-L(9)*ul(i) L(2)-L(10)*ul(i) L(3)-L(11)*ul(i)]
        [L(5)-L(9)*vl(i) L(6)-L(10)*vl(i) L(7)-L(11)*vl(i)]
        [R(1)-R(9)*ur(i) R(2)-R(10)*ur(i) R(3)-R(11)*ur(i)]
        [R(5)-R(9)*vr(i) R(6)-R(10)*vr(i) R(7)-R(11)*vr(i)]];

    q = [[ul(i)-L(4)]
        [vl(i)-L(8)]
        [ur(i)-R(4)]
        [vr(i)-R(8)]];

    RWingData = [RWingData;(inv(Q'*Q)*Q'*q)']; % Store data points into
vector
    end

%% Plot points chosen in 3D

% xa=BodyData(:,1);
% ya=BodyData(:,2);
% za=BodyData(:,3);
xc=RWingData(:,1);
yc=RWingData(:,2);
zc=RWingData(:,3);
plot3(smooth(xc),smooth(yc),smooth(zc))
grid on;

%% Save Point data to .mat file
save RWingData RWingData -double;

```


APPENDIX B. FLAPPING MECHANISM DRAWING PACKAGE

This section contains all necessary drawings and tolerance analysis for the flapping wing mechanism. Bill of materials and part numbers are all also included. All parts are modeled in SolidWorks. The help of Mike Tree in solid modeling and creating drawings is gratefully acknowledged.

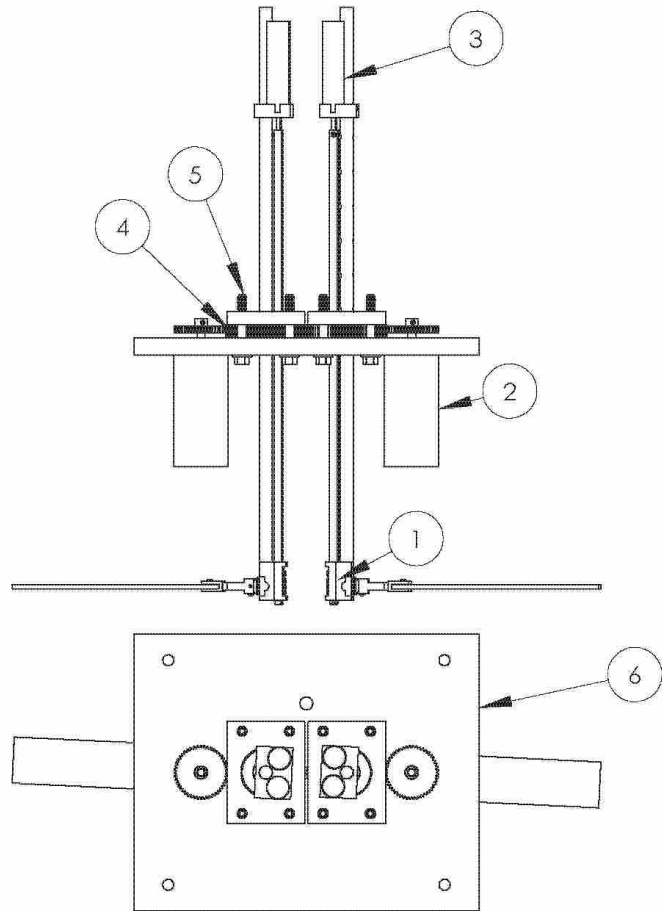
B.1 Drawing Package

Vendor List

Vendor	Item	Description	Quantity
AMC	BE15A8	Analog Servo Drive	6
AMC	BFC10010	Filter Card, Inductive: 250 V, 10A, 200µH Single Phase Load	4
Boston Gear	G1018-13564	Gear, Spur: Bronze, 20 Teeth, 14.5° PA, 48 Diametral Pitch, 0.1875" Bore	4
Boston Gear	HLSH-1-13026	Gear, Worm: Hardened Steel, Single Thread, 1/3" Pitch Diameter, 48 Diametral Pitch, 0.1875" Bore, 0.562" Face	4
Maxon Motor	118899	Motor: EC 40 Ø40 mm, brushless, 120 Watt, CE approved, with Hall sensors	2
Maxon Motor	110516	Encoder: HEDL 5540, 500 CPT, 3 Channels, with Line Driver RS 422	2
Maxon Motor	232241	Motor: EC 16 Ø16 mm, brushless, 40 Watt, with Hall sensors	4
Maxon Motor	201940	Encoder: MR, Typ M, 128 - 512 CPT, 2 / 3 Channels, with Line Driver	4
McMaster-Carr	3759T24	Bearing, Ball: 0.094" ID Double Shielded ABEC 7	4
McMaster-Carr	4262T12	Bearing, Ball: 3/16" Shaft Diameter, Flanged Double Shielded, 1/8" Width, ABEC-7	4
McMaster-Carr	47065T135	Framing: 6 ft, 1.5" aluminum two-slot single corner	2
McMaster-Carr	47065T142	Framing Fasteners: 1" Aluminum t-slotted, 4 Ct.	5
McMaster-Carr	47065T143	Framing Plate: 1.5" Aluminum single two-hole	8
McMaster-Carr	47065T234	Framing Fasteners: 1.5" Aluminum t-slotted, drop-in, with stud	14
McMaster-Carr	5909K39	Bearings, Thrust: Needle-Roller, Steel, 1-3/8" ID, 2-1/16" OD, 4600 lb capacity	4
McMaster-Carr	5909K66	Washer, Bearing: Steel, 0.126" Thick	8
McMaster-Carr	6620K88	Frame, Differential: 304 Stainless Steel, 2"x2"x6", Unpolished Finish	4
McMaster-Carr	89535K22	Shaft, Worm: round Stock: 304 Stainless Steel, D – 1/8", L – 72";	1
McMaster-Carr	89535K23	Shaft, Main Support: round Stock: 304 Stainless Steel, D – 3/8", L – 36";	2
McMaster-Carr	86895K463	Brackets, Wing: bar Stock, 2024 Aluminum: 0.5"x0.5"x36";	1
McMaster-Carr	8975K107	Plate, Base: 6061 Aluminum Bar Stock: 10"x12"x0.5"	1

McMaster-Carr	8984K92	Shaft, Main Differential: Stainless Steel Rod, D – 3/32", L – 6"	1
McMaster-Carr	90145A312	Pin, Dowel: 18-8 Stainless Steel, 1/32" Diameter, 1/4" Length, 100 Ct.	1
McMaster-Carr	91251A543	Screw, Socket, cap: Steel, 1/4"-20, 1-3/8", 10 Ct.	1
McMaster-Carr	91375A160	Screw, Set: Steel, Socket, Cup Point, 6-40x0.125", 100 Ct.	1
McMaster-Carr	91375A190	Screw, Set: Steel, Socket, Cup Point, 8-32x0.25", 100 Ct.	1
McMaster-Carr	91783A063	Screw, Pan Head: 18-8 Stainless Steel, 1-64x0.125"x0.125", 100 Ct.	1
McMaster-Carr	91792A052	Screw, Pan Head: 18-8 Stainless Steel, 0-80x0.125"x0.125", 100 Ct.	1
McMaster-Carr	92000A010	Screw, Pan Head: 18-8 Stainless Steel, M2x0.4x3mm, 50 Ct.	1
McMaster-Carr	92979A134	Screw, Hex Head: 1/4"-20, 1 3/4" Steel, flange, cap	8
McMaster-Carr	96697A500	Washer: 1/4" Steel, wave	1
McMaster-Carr	97135A210	Nut: Hex, 1/4"-20 nylon insert, locking	1
McMaster-Carr	98408A114	Rings, E Style External Retaining: 3/32" Shaft Diam., 0.074" Groove Diam., 0.020" Groove Width, 100 Ct/	1
McMaster-Carr	98555A007	Rings, Low Clearance External Retaining: 3/16" Shaft Diam., 0.165" Groove Diam., 0.020" Groove Width, 100 Ct.	1
NI	9074	cRIO: 9074 8-Slot Integrated 400 MHz Real-Time Controller, 2M Gate FPGA	1
NI	9237	Module, Bridge: C-Series 4-Channel, 25mV/V, 24-Bit simultaneous – strain input	1
NI	9263	Module, Analog Output: 4-Channel, 100 KS/s, 16-bit, 10 V (5 channels per module)	2
NI	9411	Module, Digital Input: 6-Channel, 500 ns, 5 to 24 V; encoder input (2 per module)	3
SDP-SI	S10C8Z-032H072	Gear, Turntable: Hardened Alloy Steel, 32 DP, 72 Teeth, 20° PA	2
SDP-SI	S1084Z-032A048	Gear, Main Shaft Motor Meshing: 32 DP, 48 Teeth, 2024 Aluminum, AGMA Q10, 20° PA, 0.1875" Bore, 0.1875" Face Width, 1.5 Pitch Diameter	2
SDP-SI	S1343Z-72S36S036	Gear, Bevel: Stainless Steel, 36 Teeth, 0.5 Pitch Diameter, 1:1 Ratio, 20° PA, 0.125" Bore, 2 Ct.	3

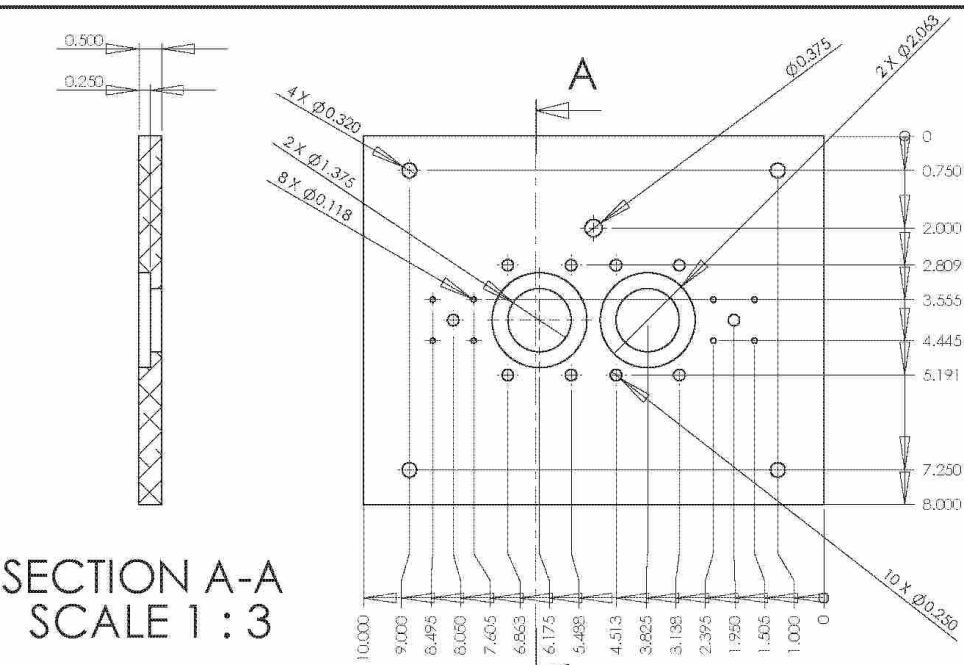
Number	Description	Quantity
1	Differential Assembly	2
2	Main Motion Assembly	2
3	Worm Motion Assembly	2
4	Turn Table Assembly	2
5	1/4-20 Flange Head Bolt	8
6	Base Plate	1



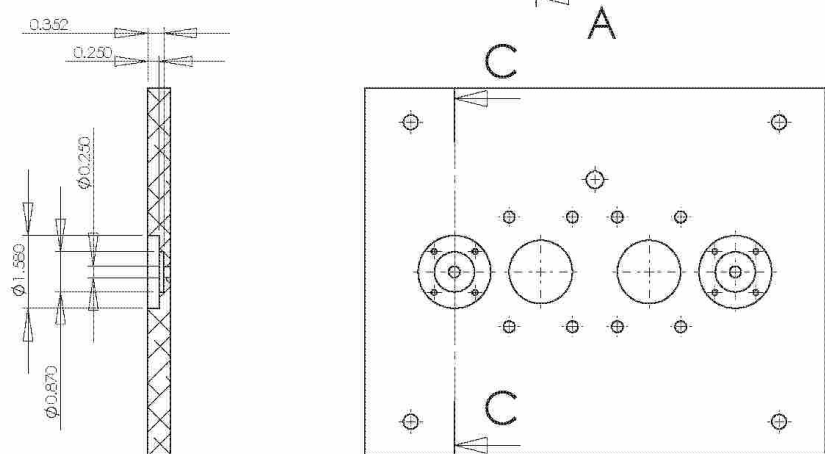
Brigham Young University Flapping Flight

UNLESS OTHERWISE SPECIFIED: DIMENSIONS ARE IN INCHES TOLERANCES: ± 0.005		FINISH:	REVISION	PART NO.	TITLE
		Machined and Sanded		--	Wing System
NAME	SIGNATURE	DATE	MATERIAL:	DWG. NO.	
DRAWN: Mike Tree		3/28/2011	Various	1	A4
CHECKED: Ryan George		6/15/2011			
APPROVED: Dr. Scott Thomson		6/30/2011	WEIGHT:	SCALE: 1:4	SHEET 1 OF 7

SECTION A-A
SCALE 1 : 3

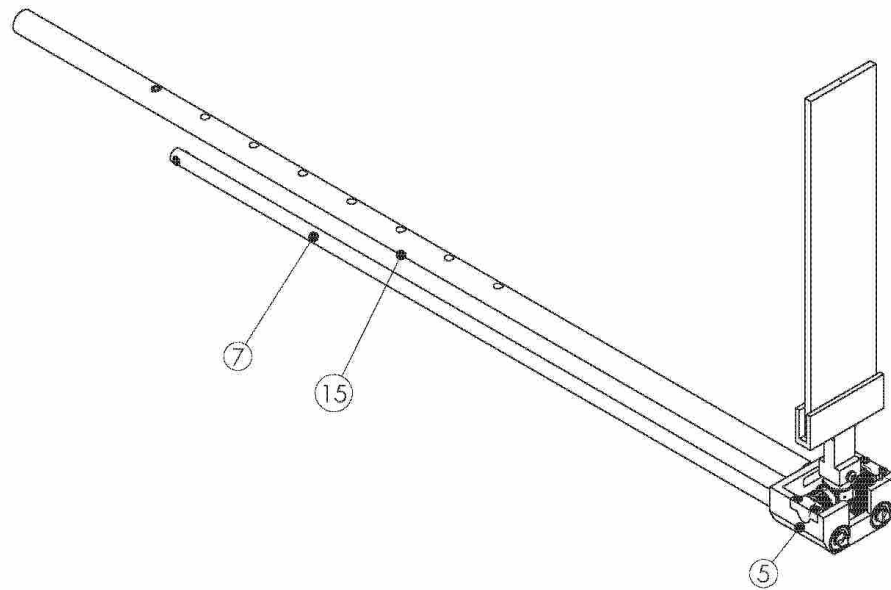


SECTION C-C
SCALE 1 : 3



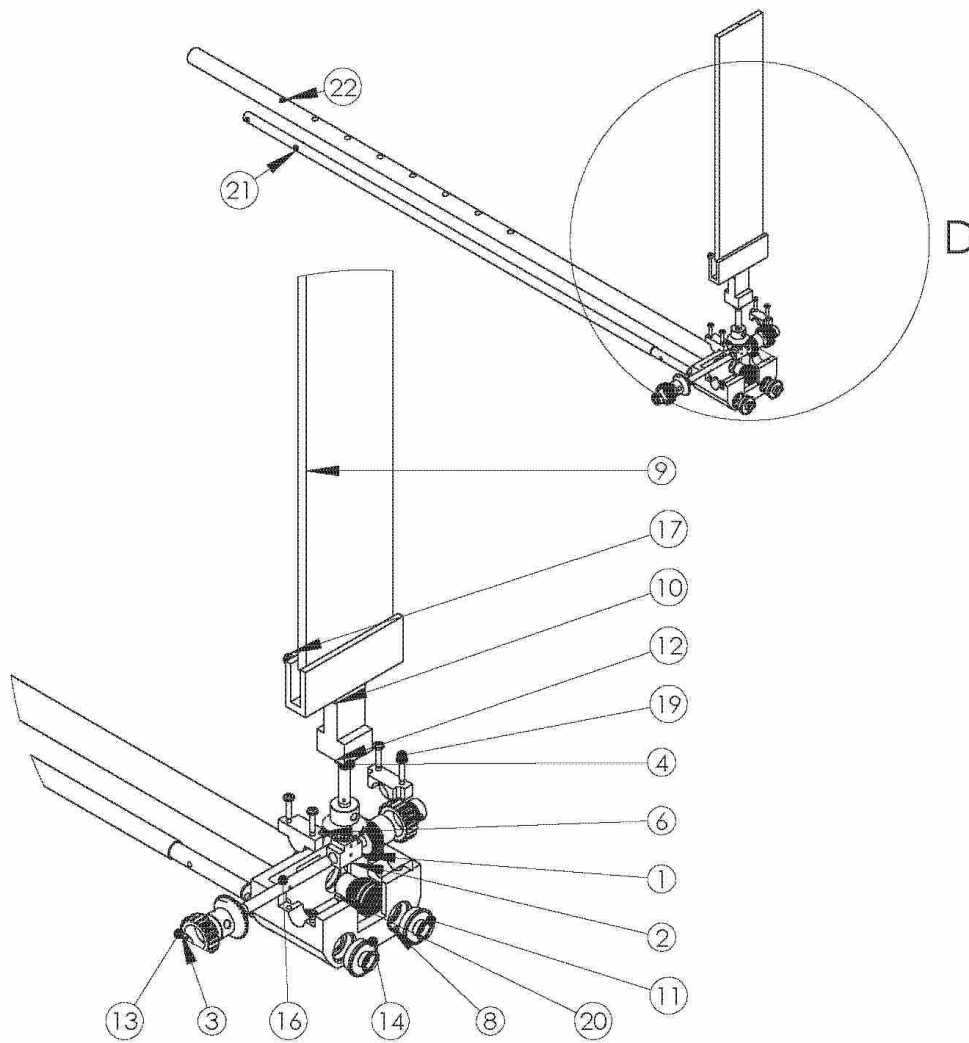
Brigham Young University Flapping Flight

UNLESS OTHERWISE SPECIFIED: DIMENSIONS ARE IN INCHES TOLERANCES: ± 0.005		FINISH: Machined and Sanded	REVISION	PART NO. 6	TITLE Base Plate
NAME	SIGNATURE	DATE	MATERIAL: 1060 Alloy	DWG. NO. 2	A4
DRAWN: Mike Tree		1/5/2011			
CHECKED: Ryan George		6/15/2011			
APPROVED: Dr. Scott Thomson		6/30/2011	WEIGHT:	SCALE: 1:5	SHEET 1 OF 1



Brigham Young University Flapping Flight

UNLESS OTHERWISE SPECIFIED: DIMENSIONS ARE IN INCHES TOLERANCES: ± 0.005		FINISH: Machined and Sanded	REVISION	PART NO. --	TITLE Differential Sub-Assembly
DRAWN: Mike Tree	SIGNATURE	DATE 3/8/2011	MATERIAL: Various		DWG NO. 3
CHECKED: Ryan George	SIGNATURE	DATE 6/15/2011			A4
APPROVED: Dr. Scott Thomson	SIGNATURE	DATE 6/30/2011	WEIGHT:	SCALE: 1:3	SHEET 2 OF 7

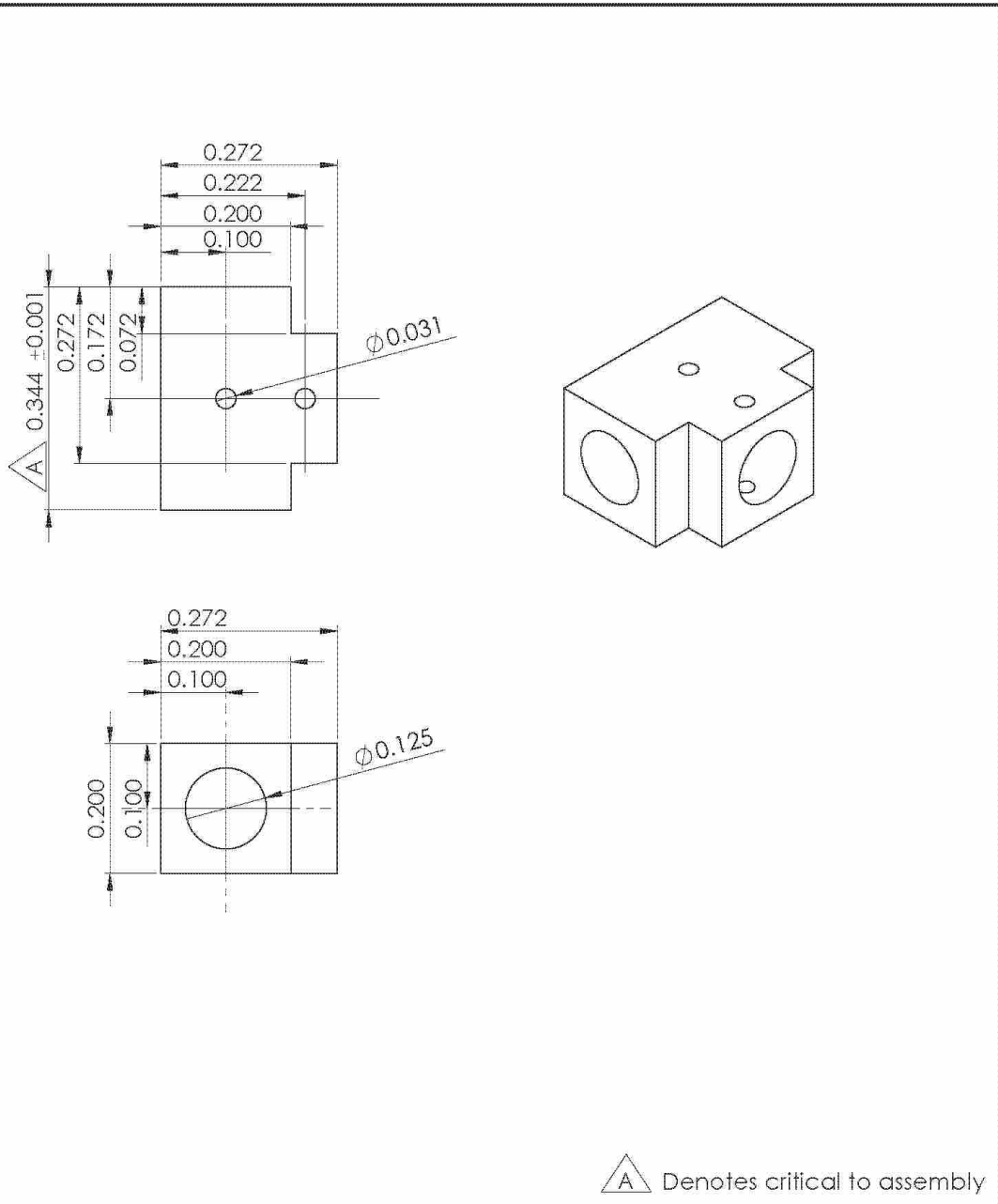


DETAIL D
SCALE 2 : 3

Brigham Young University Flapping Flight

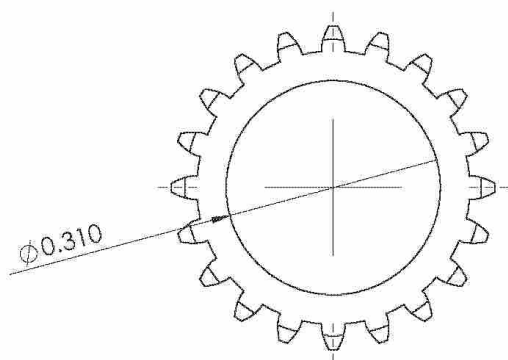
UNLESS OTHERWISE SPECIFIED: DIMENSIONS ARE IN INCHES TOLERANCES: ± 0.005		FINISH: Machined and Sanded	REVISION	PART NO. --	TITLE Differential Sub-Assembly
NAME	SIGNATURE	DATE	MATERIAL: Various	DWG. NO. 3	A4
DRAWN: Mike Tree		3/8/2011			
CHECKED: Ryan George		6/15/2011			
APPROVED: Dr. Scott Thomson		6/30/2011	WEIGHT:	SCALE: 1:3	SHEET 3 OF 7

ITEM NO.	DESCRIPTION	QTY.
1	Gear_Bevel	3
2	Hub_Center	1
3	Gear_Spur	2
4	Shaft_Wing	1
5	Frame	1
6	Bracket_Frame	2
7	shaft_worm	2
8	Gear_Worm	2
9	Wing	1
10	Bracket_Wing	1
11	Clip_C	2
12	Clip_E	1
13	Bearing_Differential	2
14	Bearing_WormShaft	4
15	Shaft_Main_Support	1
16	Shaft_Differential	1
17	SL-PHMS 0.06-80x0.125x0.125-N	2
18	B18.6.7M - M2 x 0.4 x 3 Type I Cross Recessed PHMS -3N	1
19	CR-PHMS 0.06-80x0.25x0.25-N	4
20	SL-PHMS 0.073-64x0.125x0.125-N	2
21	Set Screw #6-40x0.125	4
22	Set Screw #8-32x0.25	1



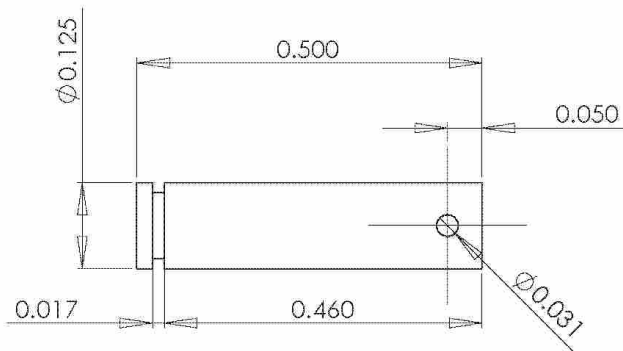
Brigham Young University Flapping Flight

UNLESS OTHERWISE SPECIFIED: DIMENSIONS ARE IN INCHES TOLERANCES: ± 0.005		FINISH: Machined and Sanded	REVISION	PART NO. 2	TITLE Center Hub
DRAWN: Mike Tree	SIGNATURE	DATE 3/8/2011	MATERIAL: 201 Annealed Stainless Steel (63)		DWG. NO. 4
CHECKED: Ryan George	SIGNATURE	DATE 6/15/2011	WEIGHT:		SCALE: 1:1
APPROVED: Dr. Scott Thomson	SIGNATURE	DATE 6/30/2011	WEIGHT:		SHEET 1 OF 1



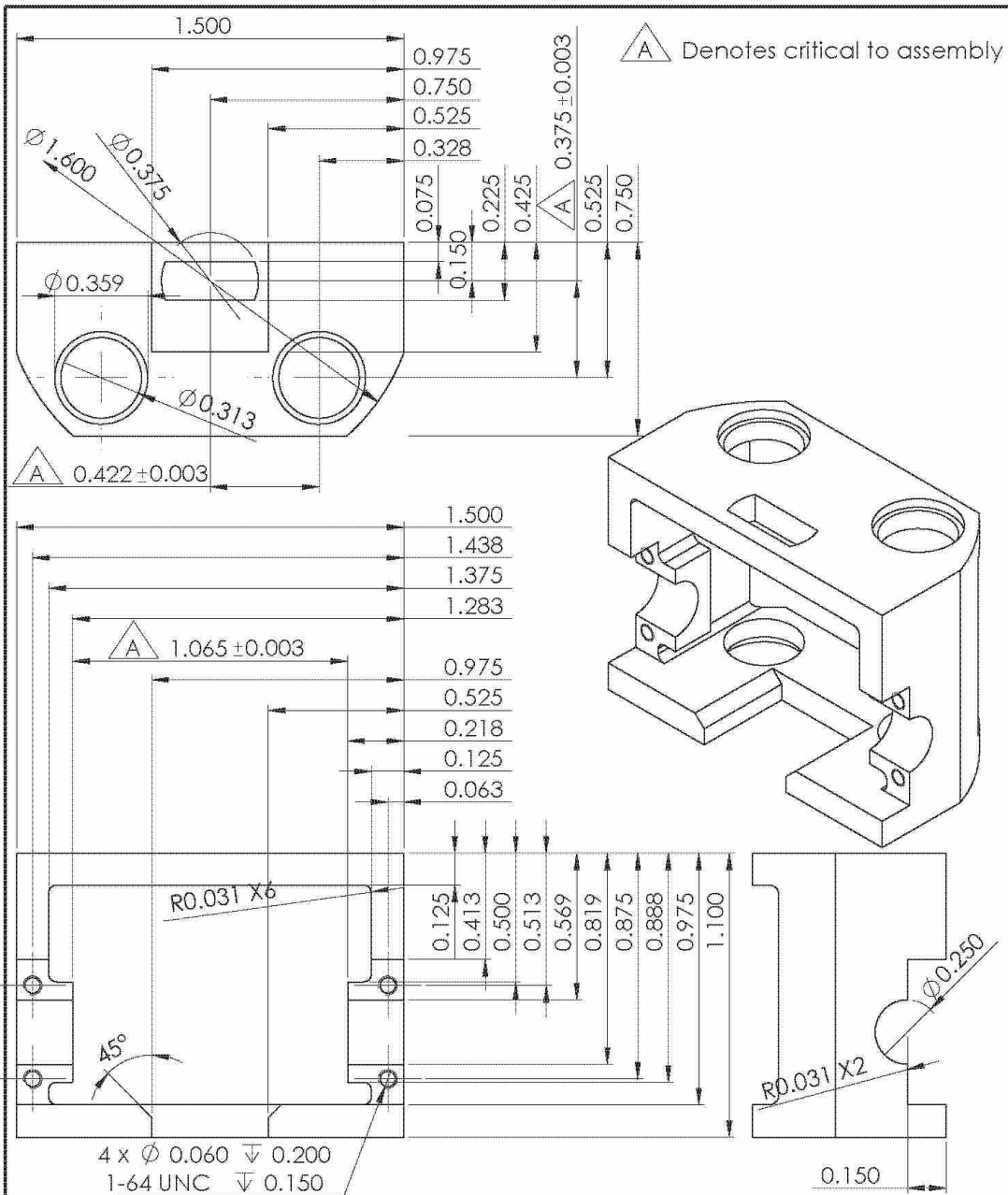
Brigham Young University Flapping Flight

UNLESS OTHERWISE SPECIFIED: DIMENSIONS ARE IN INCHES TOLERANCES: ± 0.005		FINISH: Machined and Sanded	REVISION	PART NO. 3	TITLE Spur Gear
DRAWN: Mike Tree	SIGNATURE	DATE 2/17/2011	MATERIAL: Brass		DWG. NO. 5
CHECKED: Ryan George	SIGNATURE	DATE 6/15/2011	WEIGHT:		SHEET 1 OF 1
APPROVED: Dr. Scott Thomson	SIGNATURE	DATE 6/30/2011	SCALE: 1:1		A4



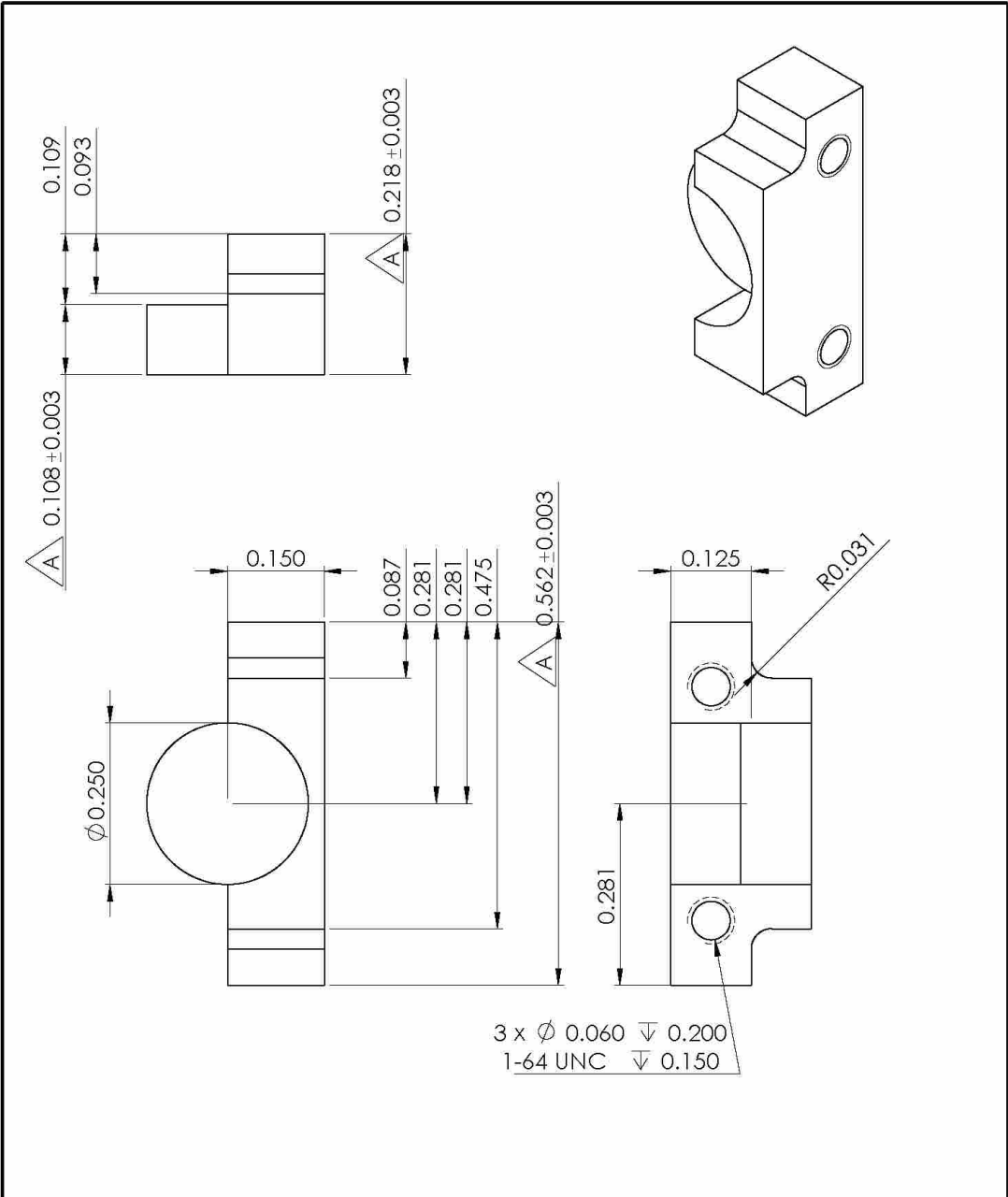
Brigham Young University Flapping Flight

UNLESS OTHERWISE SPECIFIED: DIMENSIONS ARE IN INCHES TOLERANCES: ± 0.005		FINISH: Machined and Sanded	REVISION	PART NO. 4	TITLE Wing Shaft	
DRAWN:	NAME Mike Tree	SIGNATURE	DATE	MATERIAL:	DWG. NO.	SHEET
CHECKED:	Ryan George		3/23/2011	Brass	5	A4
APPROVED:	Dr. Scott Thomson		6/30/2011	WEIGHT:	SCALE:	SHEET 1 OF 1



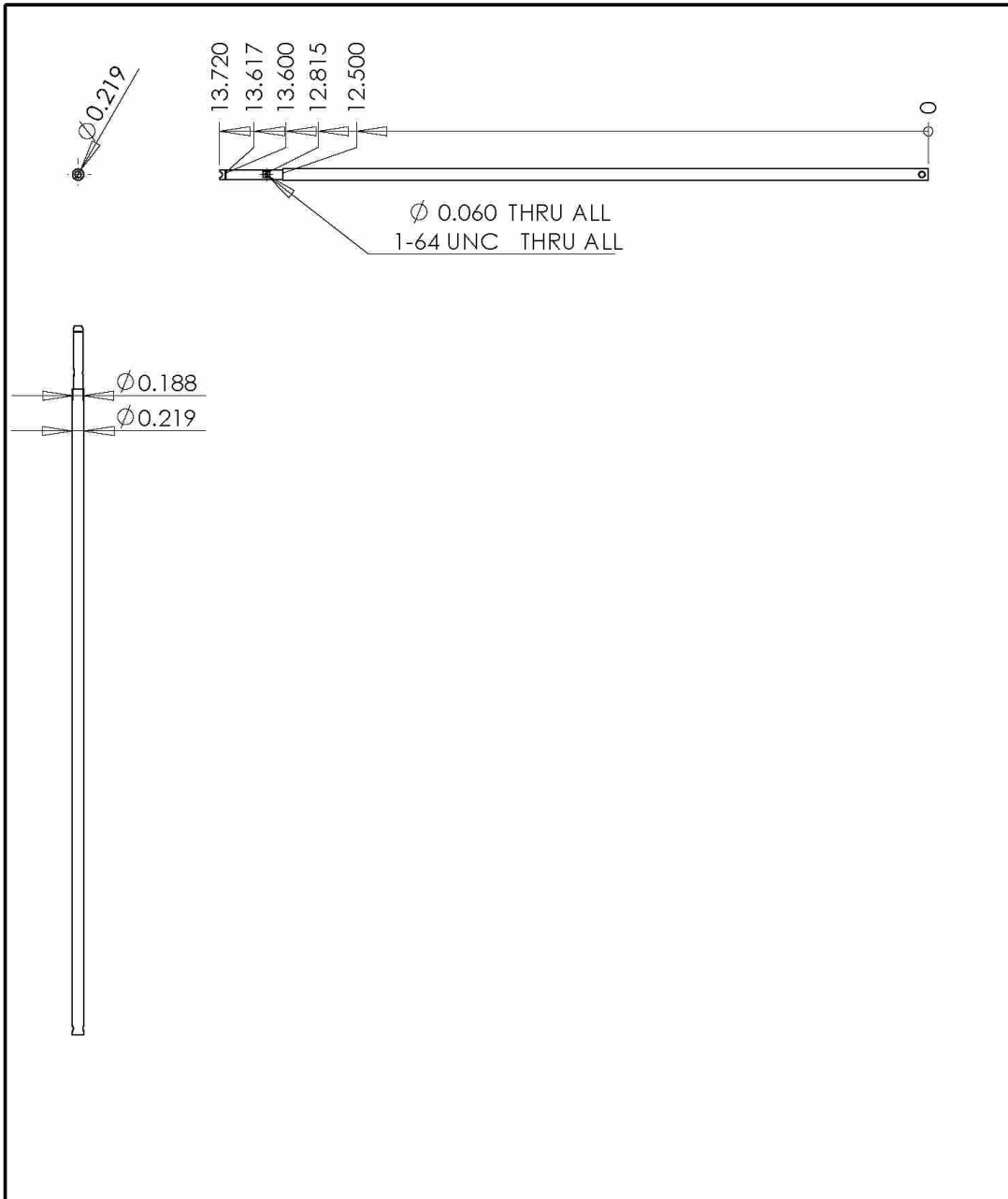
Brigham Young University Flapping Flight

UNLESS OTHERWISE SPECIFIED: DIMENSIONS ARE IN INCHES TOLERANCES: ± 0.005		FINISH: Machined and Sanded	REVISION	PART NO. 5	TITLE Frame
DRAWN: Mike Tree	SIGNATURE	DATE 1/5/2011	MATERIAL: 201 Annealed Stainless Steel (63)	DWG. NO. 6	A4
CHECKED: Ryan George	SIGNATURE	DATE 6/15/2011	WEIGHT:	SCALE: 2:1	SHEET 1 OF 1
APPROVED: Dr. Scott Thomson	SIGNATURE	DATE 6/30/2011	WEIGHT:	SCALE: 2:1	SHEET 1 OF 1



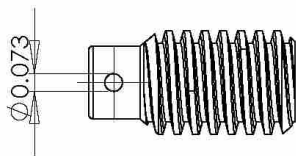
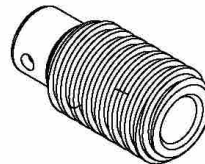
Brigham Young University Flapping Flight

UNLESS OTHERWISE SPECIFIED: DIMENSIONS ARE IN INCHES TOLERANCES: ± 0.005		FINISH: Machined and Sanded	REVISION	PART NO. 6	TITLE Frame Bracket
DRAWN	NAME Mike Tree	SIGNATURE	DATE 1/5/2011	MATERIAL: 201 Annealed Stainless Steel (63)	DWG. NO. 7
CHECK'D	Ryan George		8/15/2011		A4
APPROV'D	Dr. Scott Thomson		6/30/2011	WEIGHT:	SCALE:5T SHEET 1 OF 1



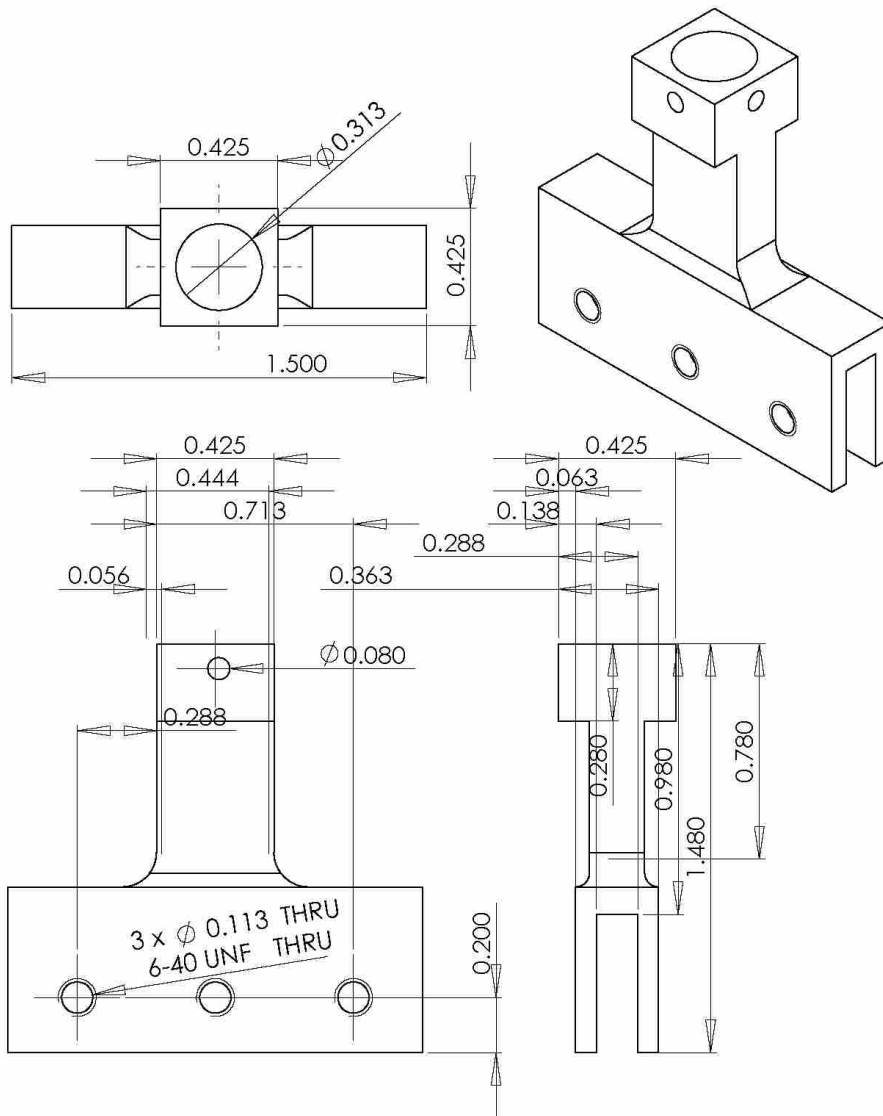
Brigham Young University Flapping Flight

UNLESS OTHERWISE SPECIFIED: DIMENSIONS ARE IN INCHES TOLERANCES: ± 0.005		FINISH: Machined and Sanded	REVISION	PART NO. 7	Worm Shaft
DRAWN: Mike Tree	SIGNATURE	DATE 3/3/2012	MATERIAL: Annealed Stainless Steel (SS)	DWG. NO. 8	A4
CHK'D: Ryan George	SIGNATURE	DATE 6/15/2011	WEIGHT:	SCALE: 1:3	SHEET 1 OF 1
APP'VD: Dr. Scott Thomson	SIGNATURE	DATE 6/30/2011	WEIGHT:	SCALE: 1:3	SHEET 1 OF 1



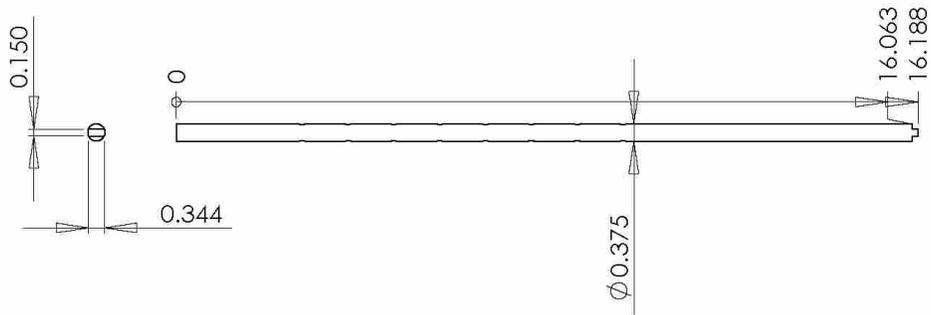
Brigham Young University Flapping Flight

UNLESS OTHERWISE SPECIFIED: DIMENSIONS ARE IN INCHES TOLERANCES: ± 0.005		FINISH: Machined and Sanded	REVISION	PART NO. 8	TITLE Worm Gear	
DRAWN	NAME Mike Tree	SIGNATURE	DATE 3/17/2011	MATERIAL: Plain Carbon Steel	DWG. NO. 9	
CHK'D	NAME Ryan George	SIGNATURE	DATE 6/15/2011			SHEET 1 OF 1
APP'VD	NAME Dr. Scott Thomson	SIGNATURE	DATE 6/30/2011			
				WEIGHT:	SCALE:2:1	



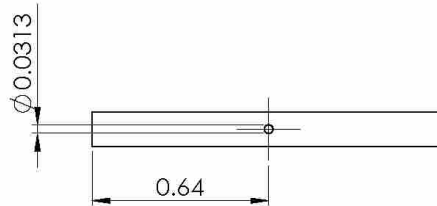
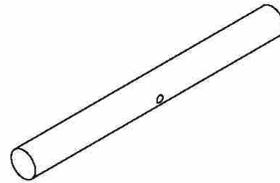
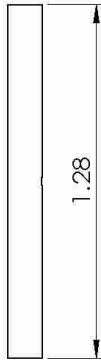
Brigham Young University Flapping Flight

UNLESS OTHERWISE SPECIFIED: DIMENSIONS ARE IN INCHES TOLERANCES: ± 0.005		FINISH: Machined and Sanded	REVISION	PART NO. 10	TITLE Wing Bracket
DRAWN Mike Tree	SIGNATURE	DATE 4/4/2011	MATERIAL: 1060 Alloy		DWG. NO. 10
CHK'D Ryan George	SIGNATURE	DATE 6/15/2011	WEIGHT:		A4
APP'VD Dr. Scott Thomson	SIGNATURE	DATE 6/30/2011	SCALE:2:1		SHEET 1 OF 1



Brigham Young University Flapping Flight

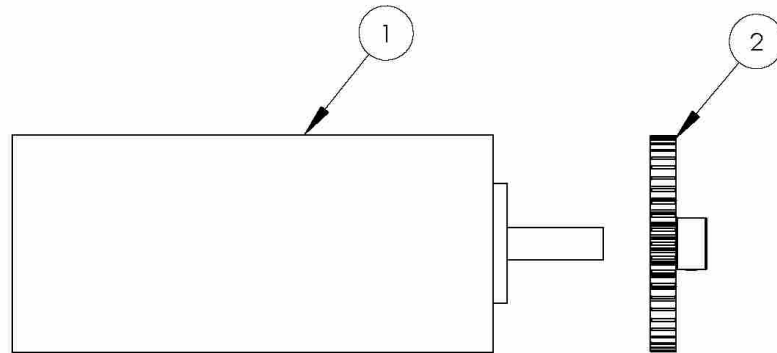
UNLESS OTHERWISE SPECIFIED: DIMENSIONS ARE IN INCHES TOLERANCES: ± 0.005		FINISH: Machined and Sanded	REVISION	PART NO. 15	TITLE Main Support Shaft
DRAWN	NAME Mike Tree	SIGNATURE	DATE 2/24/2011	MATERIAL: 201 Annealed Stainless Steel (SS)	DWG. NO. 11
CHK'D	NAME Ryan George	SIGNATURE	DATE 6/15/2011	WEIGHT:	A4
APP'VD	NAME Dr. Scott Thomson	SIGNATURE	DATE 6/30/2011	SCALE: 1:3	SHEET 1 OF 1



Brigham Young University Flapping Flight

UNLESS OTHERWISE SPECIFIED: DIMENSIONS ARE IN INCHES TOLERANCES: ± 0.005		FINISH: Machined and Sanded	REVISION	PART NO. 16	TITLE Differential Shaft
DRAWN	NAME Mike Tree	SIGNATURE	DATE 3/2/2011	MATERIAL: Brass	DWG. NO. 12
CHK'D	Ryan George	SIGNATURE	DATE 6/15/2011		
APP'VD	Dr. Scott Thomson	SIGNATURE	DATE 6/30/2011		
WEIGHT:				SCALE: 2:1	SHEET 1 OF 1

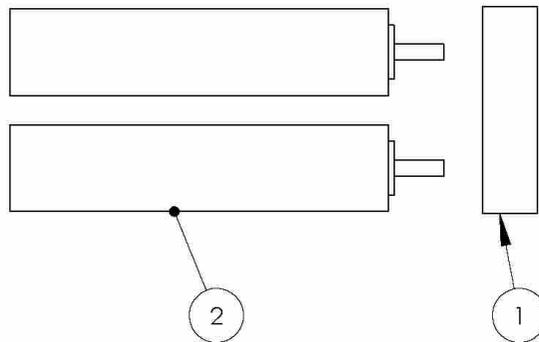
ITEM NO.	DESCRIPTION	QTY.
1	40mm motor	1
2	Meshing Gear	1



Brigham Young University Flapping Flight

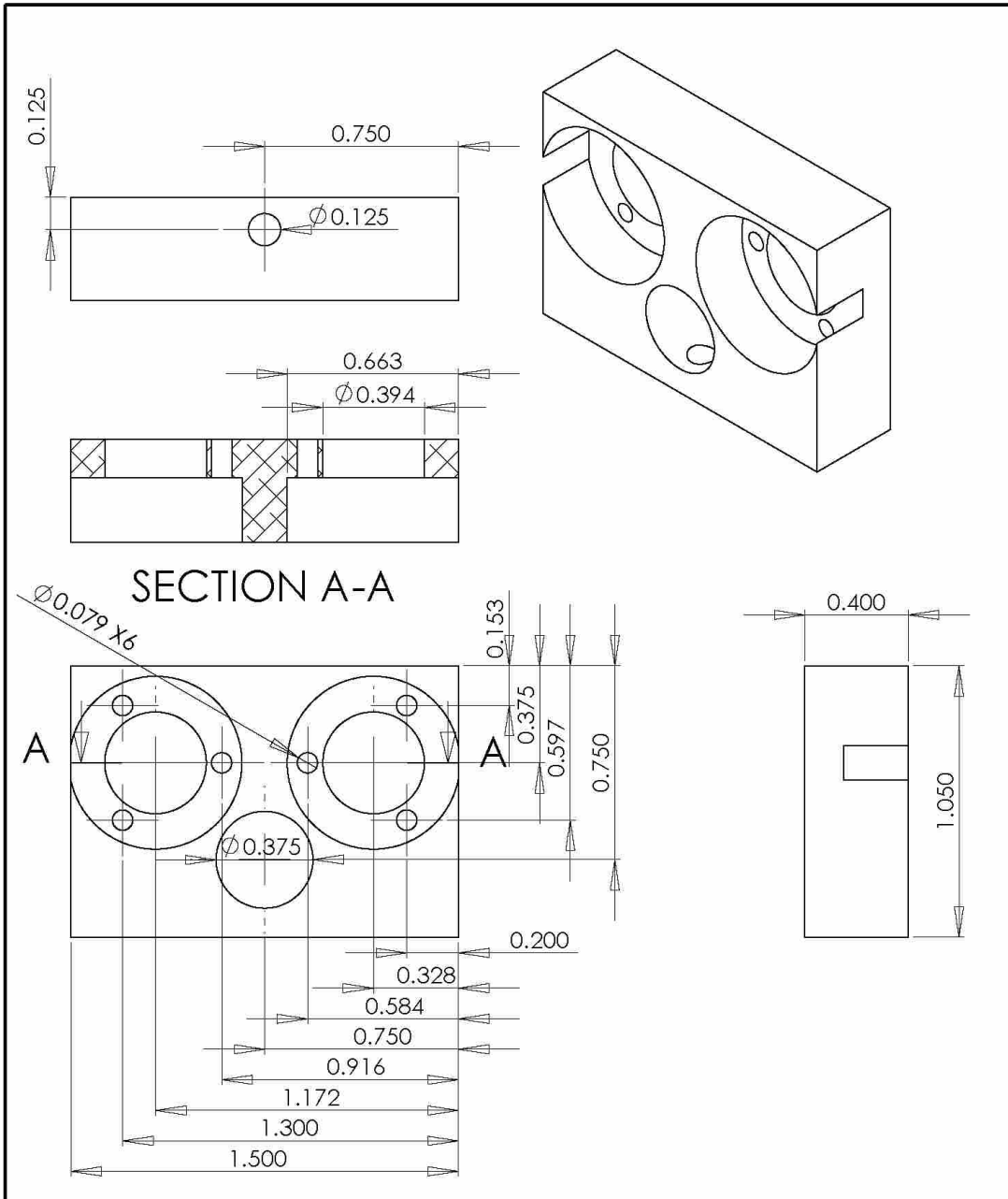
UNLESS OTHERWISE SPECIFIED: DIMENSIONS ARE IN INCHES TOLERANCES: ± 0.005		FINISH:	REVISION	PART NO.	TITLE
		From Manufacturer		--	Main Motion Assembly
NAME	SIGNATURE	DATE	MATERIAL:	DWG. NO.	
DRAWN: Mike Tree		4/14/2011	Various	13	A4
CHECK'D: Ryan George		6/15/2011			
APPROV'D: Dr. Scott Thomson		6/30/2011	WEIGHT:	SCALE: 1:1	SHEET 5 OF 7

ITEM NO.	DESCRIPTION	QTY.
1	Motor Mount	1
2	16mm Motor	2



Brigham Young University Flapping Flight

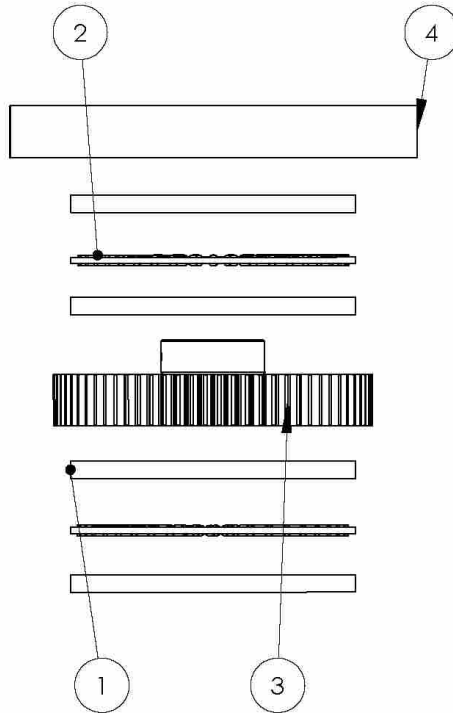
UNLESS OTHERWISE SPECIFIED: DIMENSIONS ARE IN INCHES TOLERANCES: ± 0.005		FINISH: Machined and Sanded	REVISION	PART NO. --	TITLE Worm Motion Assembly	
DRAWN	NAME Mike Tree	SIGNATURE	DATE 4/24/2011	MATERIAL: Various	DWG. NO. 14	
CHK'D	NAME Ryan George	SIGNATURE	DATE 6/15/2011			SHEET 6 OF 7
APP'VD	NAME Dr. Scott Thomson	SIGNATURE	DATE 6/30/2011			WEIGHT:



Brigham Young University Flapping Flight

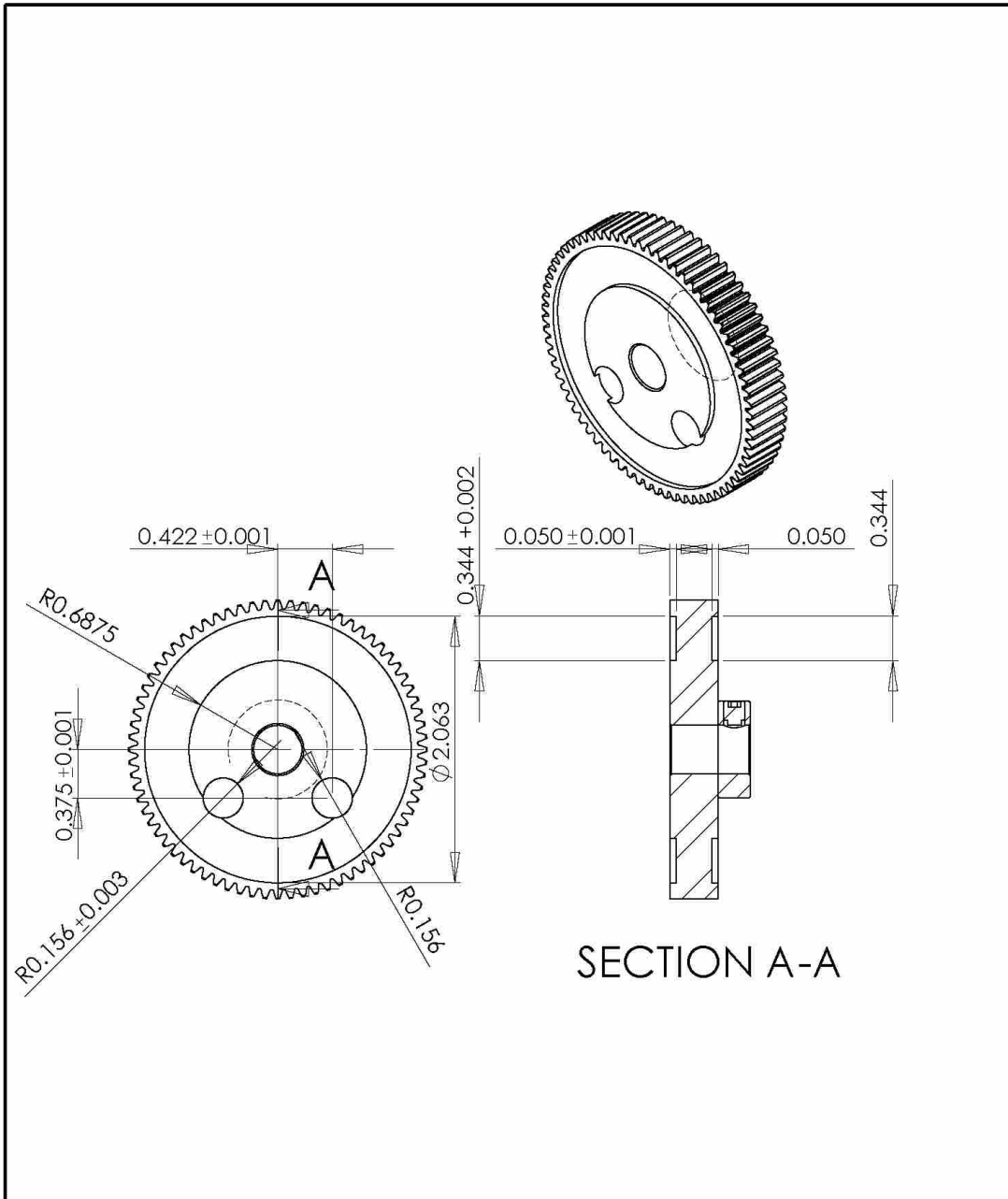
UNLESS OTHERWISE SPECIFIED: DIMENSIONS ARE IN INCHES TOLERANCES: ± 0.005		FINISH: Machined and Sanded	REVISION	PART NO. 1	TITLE Motor Mount
DRAWN	NAME Mike Tree	SIGNATURE	DATE 3/19/2011	MATERIAL: 1060 Alloy	DWG. NO. 15
CHK'D	NAME Ryan George	SIGNATURE	DATE 6/15/2011	WEIGHT:	A4
APPROV'D	NAME Dr. Scott Thomson	SIGNATURE	DATE 6/30/2011	SCALE: 2:1	SHEET 1 OF 1

ITEM NO.	DESCRIPTION	QTY.
1	BearingRace	4
2	NeedleBearing	2
3	Main Gear	1
4	TopGuide	1



Brigham Young University Flapping Flight

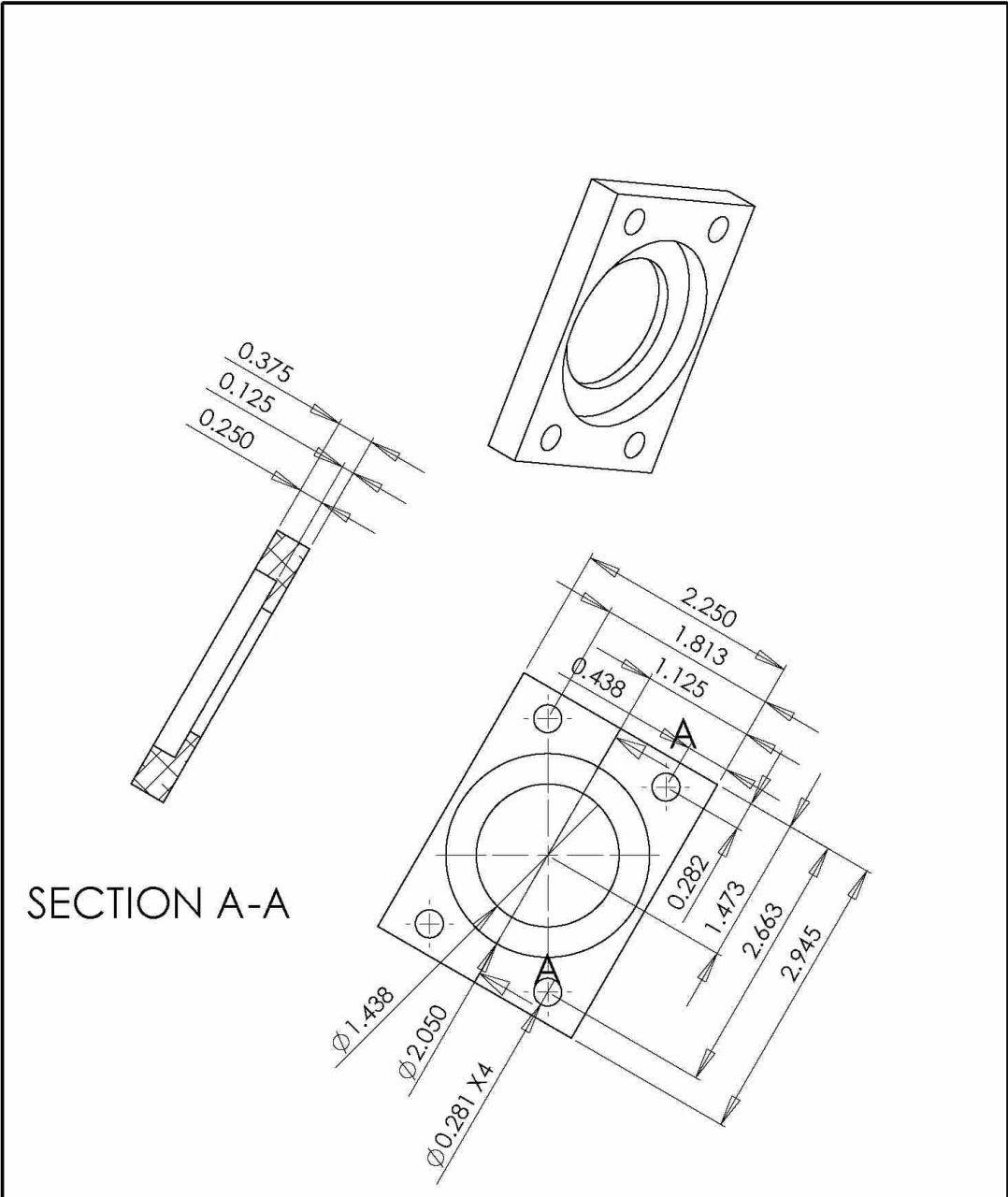
UNLESS OTHERWISE SPECIFIED: DIMENSIONS ARE IN INCHES TOLERANCES: ± 0.005		FINISH:	REVISION	PART NO.	TITLE
		Machined and Sanded		--	Turn Table Assembly
NAME	SIGNATURE	DATE	MATERIAL:	DWG. NO.	
DRAWN: Mike Tree		4/3/2011	Various	16	A4
CHK'D: Ryan George		6/15/2011			
APP'VD: Dr. Scott Thomson		6/30/2011	WEIGHT:	SCALE: 1:1	SHEET 7 OF 7



SECTION A-A

Brigham Young University Flapping Flight

UNLESS OTHERWISE SPECIFIED: DIMENSIONS ARE IN INCHES TOLERANCES: ± 0.005		FINISH: Machined and Sanded	REVISION	PART NO. 3	TITLE Top Main Gear
DRAWN Mike Tree	SIGNATURE	DATE 5/1/2011	MATERIAL: AISI 4340 Steel, annealed	DWG. NO. 17	A4
CHECKED Ryan George		DATE 6/15/2011	WEIGHT:	SCALE: 1:1	SHEET 1 OF 1
APPROVED Dr. Scott Thomson		DATE 6/30/2011			



Brigham Young University Flapping Flight

UNLESS OTHERWISE SPECIFIED: DIMENSIONS ARE IN INCHES TOLERANCES: ± 0.005		FINISH: Machined and Sanded	REVISION	PART NO. 4	TITLE Top Guide	
DRAWN	NAME Mike Tree	SIGNATURE	DATE	MATERIAL:	DWG. NO.	18
CHK'D	Ryan George		3/15/2011	1060 Alloy		
APP'VD	Dr. Scott Thomson		6/30/2011	WEIGHT:	SCALE: 1:1.2	
					SHEET 1 OF 1	A4

B.2 Tolerance Analysis

Assumptions		
Part tolerance Spec:	3 Sigma	
Total (RSS) Tol	6 Sigma	
Mean Shift	1.5 Sigma	

Note on Vec: Linear Dimensions = +-1 effect
 Efects: Circular Dimensions = +-5 (half for the hole, and half for the post - or -5 for the radius from a diameter)
 Surfaces/Fitneses can have +-2 if 2 surfaces are used in the stack.
 Variation in X, Y, and Z dimensions can be calculated with an equation as a vector in the desired direction.
 NOTE: "CTRL+1" BEGINS A CLEARANCE STUDY WHILE "CTRL+H" BEGINS AN INTERFERENCE STUDY.

Sample Part

	Mean	Tolerance	Vector Effect	Nominal W/Efect	RSS Tolerance	WC Tolerance	%WCTol
Envelope	4.974	0.003	1	4.974	0.000009	0.003	21%
Part 1 Width	1.24	0.004	-1	-1.24	0.000016	0.004	29%
Part 2 Width	1.24	0.003	-1	-1.24	0.000009	0.003	21%
Part 3 Width	1.24	0.002	-1	-1.24	0.000004	0.002	14%
Part 4 Width	1.24	0.002	-1	-1.24	0.000004	0.002	14%
Clearance Between Envelope and Eroads #1-4 in X:			Nominal	0.014	± 0.013	± 0.014	STDevs
					Min	0.000	DPPM
					Max	0.027	0.028
							1 Failure Per
							3157497

Main Frame

	Mean	Tolerance	Vector Effect	Nominal W/Efect	RSS Tolerance	WC Tolerance	%WCTol
Inside distance between mounting hubs:	1.065	0.003	1	1.065	0.000009	0.003	80%
Bevel gear length	0.359	0.0005	-1	-0.359	0.0000025	0.0005	10%
Center hub length	0.344	0.001	-1	-0.344	0.000001	0.001	20%
Bevel gear length	0.359	0.0005	-1	-0.359	0.0000025	0.0005	10%
Clearance			Nominal	0.003	± 0.006	± 0.005	STDevs
					Min	-0.003	-0.002
					Max	0.009	0.009
							1 Failure Per
							10

Gears Always Interfere (Interference Study)

	Mean	Tolerance	Vector Effect	Nominal W/Efect	RSS Tolerance	WC Tolerance	%WCTol
Inside distance between mounting hubs:	1.065	0.003	-1	-1.065	0.000009	0.003	17%
Base to pitch diameter location	0.331	0.005	1	0.331	0.000025	0.005	28%
Pitch diameter	0.176	0.005	1	0.176	0.000025	0.005	28%
Base to pitch diameter location	0.331	0.005	1	0.331	0.000025	0.005	28%
Interference			Nominal	-0.227	± 0.018	± 0.018	STDevs
					Min	-0.245	-0.245
					Max	-0.209	-0.209
							1 Failure Per
							INF

Drive Shaft Stack

	Mean	Tolerance	Vector Effect	Nominal W/Efect	RSS Tolerance	WC Tolerance	%WCTol
Shaft step to end of c-clip groove	1.117	0.005	1	1.117	0.000025	0.005	16%
C-clip height	0.015	0.002	-1	-0.015	0.000004	0.002	8%
Bushing lip height	0.05	0.005	-1	-0.05	0.000025	0.005	16%
Stepped shaft bushing bore depth	0.05	0.005	1	0.05	0.000025	0.005	16%
Main frame height	1.1	0.005	-1	-1.1	0.000025	0.005	16%
Stepped shaft bushing bore depth	0.05	0.005	1	0.05	0.000025	0.005	16%
Bushing lip height	0.05	0.005	-1	-0.05	0.000025	0.005	16%
Clearance			Nominal	0.002	± 0.025	± 0.032	STDevs
					Min	-0.023	-0.030
					Max	0.027	0.034
							1 Failure Per
							845305.81

Other Interactions

	Mean	Tolerance	Vector Effect	Nominal W/Efect	RSS Tolerance	WC Tolerance	%WCTol
Wing bracket inside diameter	0.3125	0.0003	1	0.3125	0.0000009	0.0003	8%
Bevel gear outside diameter	0.312	0.005	-1	-0.312	0.000025	0.005	94%
Clearance			Nominal	0.0005	± 0.010	± 0.005	STDevs
					Min	-0.010	-0.005
					Max	0.011	0.008
							1 Failure Per
							885034.87

Main Shaft Stack

	Mean	Tolerance	Vector Effect	Nominal W/Efect	RSS Tolerance	WC Tolerance	%WCTol
Bevel gear inside diameter	0.1248	0.0005	1	0.1248	0.0000025	0.0005	63%
Main shaft diameter	0.1245	0.0005	-1	-0.1245	0.0000009	0.0005	38%
Clearance			Nominal	0.0003	± 0.001	± 0.001	STDevs
					Min	-0.001	-0.001
					Max	0.001	0.001
							1 Failure Per
							452656.56

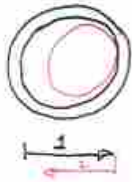
Drive Shaft/Bushing Stack

	Mean	Tolerance	Vector Effect	Nominal W/Efect	RSS Tolerance	WC Tolerance	%WCTol
Bushing inside diameter	0.188	0.003	1	0.188	0.000009	0.003	50%
Drive shaft stepped diameter	0.1875	0.003	-1	-0.1875	0.000009	0.003	50%
Clearance			Nominal	0.0005	± 0.008	± 0.006	STDevs
					Min	-0.008	-0.006
					Max	0.009	0.007
							1 Failure Per
							874194.80

Top Guide/Tumble Gear Stack

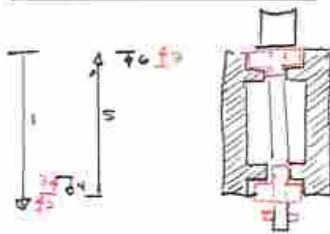
	Mean	Tolerance	Vector Effect	Nominal W/Efect	RSS Tolerance	WC Tolerance	%WCTol
Tumble gear	2.048	0	-1	-2.048	0	0	0%
Top Guide inner diameter	2.05	0.002	1	2.05	0.000004	0.002	100%
Clearance			Nominal	0.002	± 0.004	± 0.002	STDevs
					Min	-0.002	0.000
					Max	0.006	0.004
							1 Failure Per
							56807.20

Main Shaft Stack



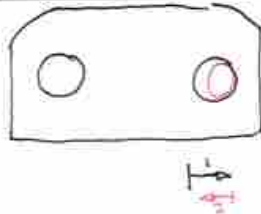
#	Dim Name	Vector
1	Bevel gear inside diameter	+1
2	Main shaft diameter	-1

Drive Shaft Stack



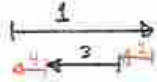
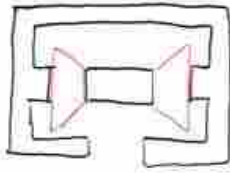
#	Dim Name	Vector
1	Shaft step to end of C-clip groove	+1
2	C-clip height	-1
3	Bushing lip height	-1
4	Stepped shaft bushing bore depth	+1
5	Main frame height	-1
6	Stepped shaft bushing bore depth	+1
7	Bushing lip height	-1

Drive Shaft/^{Bushing}Main Housing Stack



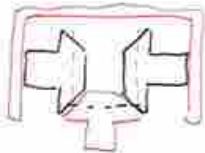
#	Dim Name	Vector
1	Bushing inside diameter	+1
2	Drive shaft stepped dia	-1

Main Housing Gear Stack



#	Dim Name	Vector
1	Inside distance between mounting hubs	+1
2	Bevel gear length	-1
3	Center hub length	-1
4	Bevel gear length	-1

Gears Always Interfere



#	Dim Name	Vector
1	Inside distance between mounting hubs	+1
2	Base to pitch diameter location	-1
3	Pitch diameter	-1
4	Base to pitch diameter location	-1

Gear/Wing Bracket Interface



#	Dim Name	Vector
1	Wing Bracket inside diameter	+1
2	Bevel gear outside diameter	-1

APPENDIX C. FLAPPING MECHANISM FORCE ANALYSIS – MATLAB

MATLAB is the primary tool used for analysis of force data recorded from the flapping wing mechanism. The following files are used to analyze forces, transform them into an inertial frame, and perform gradient based optimization.

C.1 Box-Behnken Analysis

```
%% Box Behnkin Analysis
% This .m file will read in all the data result files from a Box-Behnkin
% run and transform the forces in the the earth X,Y,Z frame. The results
% are plotted thrust vs. lift.

% From there, the user can choose the point for the next Box-Behnkin
% iteration.

% Created by Ryan George and Dr. Mark Colton
% 3 May 2011

%% House keeping

clc;
clear all;
%close all;

%% Declare a few parameters

bbsize = 15; %number of variables
ts = 0.002; %seconds (time step)
ramp_t = 1; %seconds (time to ramp into trajectory (quintic poly))
f_freq = 0.3333; %Hz (flapping frequency)

%% Load data files

for i=1:length(bbdesign(bbsize))

    % Load data from file
    i
    data = load(sprintf('C:\\Users\\Ryan Brandon George\\Documents\\Research
- Masters\\Flapping Flight Mechanism\\Testing
Results\\20110510_bb15\\test%03d.txt',i));
    data(1,:) = [];
    strain = data(:,2);
    motor(:,1) = data(:,3);
    motor(:,2) = data(:,5);
    motor(:,3) = data(:,7);
    setpoint(:,1) = data(:,4);
    setpoint(:,2) = data(:,6);
    setpoint(:,3) = data(:,8);
    time = data(:,1);
    clear data;

    % Determine sample rate and Nyquist frequency.
    % dt = mean(diff(time));
    dt = 0.002;
    fs = 1/dt; % Sampling frequency
    fn = fs/2; % Nyquist frequency
    fc = 5; % Cutoff frequency

    % Filter strain gage data
```

```

[B,A] = butter(3,fc/fn);
strain_f = filtfilt(B,A,strain);

% Remove offset from strain data
offset = mean(strain(1:6));
strain_f = strain_f - offset;

% Cut off Quintic poly and 1st and last flapping cycle
cutoff = floor(((1/f_freq)+ramp_t)/ts);
cutoffend = floor((ramp_t)/ts);

% cutting beginning
motor(1:cutoff,:) = [];
setpoint(1:cutoff,:) = [];
strain_f(1:cutoff) = [];
strain(1:cutoff) = [];
time(1:cutoff) = [];

% cutting end
motor(length(motor)-cutoffend+1:length(motor),:) = [];
setpoint(length(setpoint)-cutoffend+1:length(setpoint),:) = [];
strain_f(length(strain_f)-cutoffend+1:length(strain_f)) = [];
strain(length(strain)-cutoffend+1:length(strain)) = [];
time(length(time)-cutoffend+1:length(time)) = [];

% Convert Motor and Setpoint data into usable kinematics (degrees)
theta(:,1) = (motor(:,1) + motor(:,2))/40;
theta(:,2) = (motor(:,1) - motor(:,2))/40;
theta(:,3) = motor(:,3);

thetaSet(:,1) = (setpoint(:,1) + setpoint(:,2))/40;
thetaSet(:,2) = (setpoint(:,1) - setpoint(:,2))/40;
thetaSet(:,3) = setpoint(:,3);

% Figure out how closely motors tracked actual values
tracking = thetaSet - theta;
track_error(i) = abs(sum(sum(tracking)));

% Also Calculate RMS and Average error
tracking2 = tracking.^2;
RMS(i,:) = sqrt(sum(tracking2,1)/length(tracking2));
AvgErr(i,:) = sum(abs(tracking)/length(tracking),1);

% Transform forces into home X,Y,Z frame
for j=1:length(setpoint)
    f_inertial(j,:) =
transform_forces([0,0,strain_f(j)]',[theta(j,3)*(pi/180),theta(j,1)*(pi/180),
theta(j,2)*(pi/180)]');
end

% Store data for use in choosing next point
force(i,:) = mean(f_inertial);

% Clean up for next iteration
clear motor

```

```

clear setpoint
clear strain
clear strain_f
clear time

end
%% Plot Results

% Plot of Thrust vs Lift
figure;
plot(force(:,2),force(:,3),'.')
hold on

for i=1:length(force)
    text(force(i,2)+.02,force(i,3),num2str(i))
end

xlabel('Thrust (au)');
ylabel('Lift (au)');
grid on;
grid on;
hold on;
plot([0 7],[0 7],'k');
plot([0 17*cos(deg2rad(55))],[0 17*sin(deg2rad(55))],'--k');
plot([0 17*cos(deg2rad(35))],[0 17*sin(deg2rad(35))],'--k');
axis([-12 4 -4 10]);

```

C.2 Mathscript Node for Generating Trajectories

```
% Load in 12 variables from box behnkin

% bb = load('C:\Documents and Settings\Thomson\My Documents\RyanGeorge\cRIO
Flapping Test v1\bbdesign12_2.txt');
%bbb = load('C:\Documents and Settings\Thomson\My Documents\RyanGeorge\cRIO
Flapping Test v1\bbdesign12.txt');
%bb = load('C:\Documents and Settings\Thomson\My Documents\RyanGeorge\cRIO
Flapping Test v1\bbdes.mat');
clc;
clear all;
close all;

i = 1;
f1 = 0.5;
f2 = 0.5;
f3 = 0.5;
bb = bbdesign(12);
A = bb(i, :);

% Define pi
pi = 3.1415926535897932;
ts = 0.002;

% Time vector
t = 0:ts:14;

% Step size
s11 = 10;
s12 = 20;
s13 = 20;
s14 = 10;
s21 = 10;
s22 = 20;
s23 = 20;
s24 = 10;
s31 = 10;
s32 = 20;
s33 = 20;
s34 = 10;

% Initial Amplitude
am11 = 0;
am12 = 30;
am13 = 0;
am14 = 0;
am21 = 0;
am22 = 0;
am23 = -45;
am24 = 0;
am31 = 0;
```

```

am32 = 50;
am33 = 0;
am34 = 0;

% Flapping Trajectory
angle(:,1) = (am11 + (s11*A(1))) + (am12 + (s12*A(2)))*sin(f1*2*pi.*t) +
(am13 + (s13*A(3)))*cos(f1*2*pi.*t) + (am14 + (s14*A(4)))*sin(2*f1*2*pi.*t);
angle(:,2) = (am21 + (s21*A(5))) + (am22 + (s22*A(6)))*sin(f2*2*pi.*t) +
(am23 + (s23*A(7)))*cos(f2*2*pi.*t) + (am24 + (s24*A(8)))*sin(2*f2*2*pi.*t);
angle(:,3) = (am31 + (s31*A(9))) + (am32 + (s32*A(10)))*sin(f3*2*pi.*t) +
(am33 + (s33*A(11)))*cos(f3*2*pi.*t) + (am34 +
(s34*A(12)))*sin(2*f3*2*pi.*t);

% Check to ensure that we have not exceeded our limits
tempsize = length(angle(:,1));

% Specify hi and low values for 3 DOF
hi1 = 70;
low1 = -80;
hi2 = 180;
low2 = -180;
hi3 = 100;
low3 = -100;

% Clip values that have exceeded limits
temp1 = (angle(:,1)).*(angle(1:tempsize,1)<=hi1) +
(hi1.*(angle(1:tempsize,1)>hi1));
temp1 = (temp1).*(angle(1:tempsize,1)>=low1) +
(low1.*(angle(1:tempsize,1)<low1));
temp2 = (angle(:,2)).*(angle(1:tempsize,2)<=hi2) +
(hi2.*(angle(1:tempsize,2)>hi2));
temp2 = (temp2).*(angle(1:tempsize,2)>=low2) +
(low2.*(angle(1:tempsize,2)<low2));
temp3 = (angle(:,3)).*(angle(1:tempsize,3)<=hi3) +
(hi3.*(angle(1:tempsize,3)>hi3));
temp3 = (temp3).*(angle(1:tempsize,3)>=low3) +
(low3.*(angle(1:tempsize,3)<low3));

% Failed attempts below
%temp1 = (angle(:,1)).*(angle(:,1)<=70) + (70.*(angle(:,1)>70));
%temp1(angle(:,1) > 70) = 70;
%temp1((1:tempsize) > 70) = 70
%temp1(temp1 < -80) = -80;
%temp2(temp2 > 180) = 180;
%temp2(temp2 < -180) = -180;
%temp3(temp3 > 90) = 90;
%temp3(temp3 < -90) = -90;

% Replace back into "angle"
angle(:,1) = temp1;
angle(:,2) = temp2;
angle(:,3) = temp3;

% Create Cubic Spline
tcs = 1;

```

```

tc = ts:ts:tcs;

% Create coefficients for start spline
a21 = (3/(tcs^2))*angle(1,1);
a22 = (3/(tcs^2))*angle(1,2);
a23 = (3/(tcs^2))*angle(1,3);
a31 = (-2/(tcs^3))*angle(1,1);
a32 = (-2/(tcs^3))*angle(1,2);
a33 = (-2/(tcs^3))*angle(1,3);

% Create Starting spline
csS1 = a21*tc.^2 + a31*tc.^3;
csS2 = a22*tc.^2 + a32*tc.^3;
csS3 = a23*tc.^2 + a33*tc.^3;

% Create coefficients for end spline
b21 = (3/(tcs^2))*angle(length(t),1);
b22 = (3/(tcs^2))*angle(length(t),2);
b23 = (3/(tcs^2))*angle(length(t),3);
b31 = (-2/(tcs^2))*angle(length(t),1);
b32 = (-2/(tcs^2))*angle(length(t),2);
b33 = (-2/(tcs^2))*angle(length(t),3);

% Create ending spling
csE1 = angle(length(t),1) - b21*tc.^2 - b31*tc.^3;
csE2 = angle(length(t),2) - b22*tc.^2 - b32*tc.^3;
csE3 = angle(length(t),3) - b23*tc.^2 - b33*tc.^3;

% Concatenate Splines into angle setpoints
angleS(:,1) = [csS1'; angle(:,1); csE1'];
angleS(:,2) = [csS2'; angle(:,2); csE2'];
angleS(:,3) = [csS3'; angle(:,3); csE3'];
angleS(:,4) = [csS1'; angle(:,1); csE1'];
angleS(:,5) = [csS2'; angle(:,2); csE2'];
angleS(:,6) = [csS3'; angle(:,3); csE3'];

% Convert Angle command into something useful for motors (since motors are
coupled)
x1(:,1) = 20*angleS(:,1) + 20*angleS(:,2);
x1(:,2) = 20*angleS(:,1) - 20*angleS(:,2);
x1(:,3) = angleS(:,3);
% Set x1 4,5,6 to anything (doesn't matter right now)
x1(:,4) = 20*angleS(:,1) + 20*angleS(:,2);
x1(:,5) = 20*angleS(:,1) - 20*angleS(:,2);
x1(:,6) = angleS(:,3)*(-1);
i = i + 1;

% set loop = 1 when iterations finish
loop = 0;
if i > length(bb)
loop = 1;
end

```

C.3 Transform Forces

```
% TRANSFORM_FORCES      Calculate wing forces in the inertial frame.
%   TRANSFORM_FORCES(F_WING, THETA) calculates the three components of the
%   wing force expressed in the inertial frame.
%
%   F_WING              A 3x1 column vector containing the forces on the wing,
%   expressed in the wing frame.
%
%   F_INERTIAL          A 3x1 column vector containing the forces on the wing,
%   expressed in the inertial frame.
%
%   THETA               A 3x1 column vector of angles (in rad) describing the
%   orientation of the wing frame relative to the inertial frame

function F_inertial = transform_forces(F_wing, theta)

% Extract individual angles from the angle vector.
th1 = theta(1); % Rotation of outer housing about vertical shaft
th2 = theta(2); % Rotation of differential housing about horizontal shaft
th3 = theta(3); % Rotation of wing about wing shaft

% Compute individual transformation matrices.
R1 = [cos(th1) sin(th1) 0; -sin(th1) cos(th1) 0; 0 0 1];
R2 = [cos(th2) 0 sin(th2); 0 1 0; -sin(th2) 0 cos(th2)];
R3 = [1 0 0; 0 cos(th3) -sin(th3); 0 sin(th3) cos(th3)];

% Compose overall transformation matrix that allows computation of
% quantities in the wing frame, given quantities in the inertial frame.
R = R3*R2*R1;

% Calculate the wing force in the inertial frame, given the wing force in
% the wing frame. Note the transpose of the rotation matrix to allow us to
% calculate inertial force given the wing force, and not the other way
% around.
F_inertial = R'*F_wing;
```

C.4 Response Surface Optimization

```
%% Optimization Using Hypersurface
% Created by: Ryan George & Dr. Christopher Mattson
% 1 June 2011

%% House keeping

clc;
clear all;
close all;

global phi X0 SS

%% Declare initial parameters

SS = [24 32 32 32 32 24 32 32 32 32 24 32 32 32 32]';
X0 = [-20 40 0 0 0 0 0 45 0 0 0 50 0 0 0]';

LB = X0 - SS;
UB = X0 + SS;

i = 1;

X1 = [-20 40 0 0 0 0 0 45 0 0 24 50 0 0 0]';

%% Optimization Setup

% Optimization Algorithm Settings
MFE = 1000000; % maximum function evaluations
MI = 1000000; % maximum number of iterations
MSQPI = 1000000; % maximum number of sequential
quadratic programming iterations
FT = 1e-3; % Tolerance on function convergence
CT = 1e-2; % Tolerance on constraint convergence
MinVarChange = 1; % Minimum Change in Variables (In
Degrees)
DiffMaxChange = 30;

OPTIONS =
optimset('Display','final','LargeScale','off','MaxSQPIter',MSQPI,'MaxFunEvals',
'MFE','MaxIter',MI,'TolFun',FT,'TolCon',CT,'DiffMinChange',MinVarChange,
'DiffMaxChange', DiffMaxChange);
% OPTIONS = optimset('Display','final','LargeScale','off');
% OPTIONS =
optimset('Display','final','LargeScale','off','MaxFunEvals',MFE,'MaxIter',MI,
'DiffMinChange',MinVarChange, 'DiffMaxChange', DiffMaxChange);

%% Call Optimization Routine

for phi=0:0.01:1
i
```

```
[Xopt, FVAL, FLAG, OUTPUT] =  
fmincon(@fitness, X1, [], [], [], [], LB, UB, @constraints, OPTIONS);  
  
Xval(:, i) = Xopt;  
FuncVal(1, i) = FVAL;  
Flag(1, i) = FLAG;  
  
i = i + 1;  
end
```

C.5 Response Surface Constraints

```
function [C,Ceq] = constraints(x)

global X0 SS

A11 = x(1);
A12 = x(2);
A13 = x(3);
A14 = x(4);
A15 = x(5);
A21 = x(6);
A22 = x(7);
A23 = x(8);
A24 = x(9);
A25 = x(10);
A31 = x(11);
A32 = x(12);
A33 = x(13);
A34 = x(14);
A35 = x(15);

% Time
ts = 0.002;
tf = 18;
t = 0:ts:tf;

% frequency
f1 = 0.3333;
f2 = 0.3333;
f3 = 0.3333;

% Radius Constraint
radmax = 2; % = R^2
rad = sum(abs(x-X0)./SS); % = R^2

radmax = radmax*100;
rad = rad*100;

% Flapping Trajectory
theta1 = A11 + A12*sin(f1*2*pi.*t) + A13*cos(f1*2*pi.*t) +
A14*sin(2*f1*2*pi.*t) + A15*cos(2*f1*2*pi.*t);
theta2 = A21 + A22*sin(f1*2*pi.*t) + A23*cos(f1*2*pi.*t) +
A24*sin(2*f1*2*pi.*t) + A25*cos(2*f1*2*pi.*t);
theta3 = A31 + A32*sin(f1*2*pi.*t) + A33*cos(f1*2*pi.*t) +
A34*sin(2*f1*2*pi.*t) + A35*cos(2*f1*2*pi.*t);

%Calculate the maximum and minimum predicted values of the thetas
theta1max = max(theta1);
theta2max = max(theta2);
theta3max = max(theta3);
theta1min = min(theta1);
theta2min = min(theta2);
theta3min = min(theta3);
```

```
%Assign absolute max and min positions for the thetas
theta1limitpos = 55;
theta2limitpos = 180;
theta3limitpos = 90;
theta1limitneg = -105;
theta2limitneg = -180;
theta3limitneg = -90;

C(1) = theta1max - theta1limitpos;
C(2) = theta2max - theta2limitpos;
C(3) = theta3max - theta3limitpos;

C(4) = theta1limitneg - theta1min;
C(5) = theta2limitneg - theta2min;
C(6) = theta3limitneg - theta3min;

C(7) = rad - radmax;

Ceq = [];
```

C.6 Response Surface Fitness Function

```
% This file defines the fitness function
function f = fitness(x)

    global phi

    load lift_z4_it3
    load thrust_z4_it3

    N = 1;

    % Define lift hypersurface
    fl = AA1 + BB1*x + x'*CC1*x;
    fl = -fl; % So we can minimize

    % Define thrust hypersurface
    ft = AA2 + BB2*x + x'*CC2*x;
    ft = -ft; % So we can minimize

    f = (phi^N)*fl + ((1-phi)^N)*ft;

end
```

C.6 Response Surface Creation

```
%% Hypersurface Fitting
% Ryan George
% 31 May 2011

%% House keeping

clc;
clear all;
close all;

%% Declare initial parameters

% Define the center points of each variable
A11 = 0;
A12 = 8;
A13 = 0;
A14 = 26;
A15 = 0;
A21 = -9;
A22 = 0;
A23 = 0;
A24 = 0;
A25 = 23;
A31 = 0;
A32 = 0;
A33 = 0;
A34 = -20;
A35 = 1;

% Define how much each variable will vary
s11 = -6;
s12 = -8;
s13 = -8;
s14 = -8;
s15 = -8;
s21 = -6;
s22 = -8;
s23 = -8;
s24 = -8;
s25 = -8;
s31 = 6;
s32 = 8;
s33 = 8;
s34 = 8;
s35 = 8;

numVars = 15;
bb = length(bbdesign(numVars));
A = bbdesign(numVars);

%% Load data from BB15
```

```

load force_z4_it3
% load force_z_it1_check
% load twofreqterm
% load ErrorIt1
% load AvgErrIt1

mean_force = force_z4_it3(:,2);

%% Create a hypersurface using the data above

% Create a matrix with all the Box-Behnken parameters used
A_all = zeros(bb,numVars);
for i = 1:bb
    A_all(i,1) = (A11+(s11*A(i,1)));
    A_all(i,2) = (A12+(s12*A(i,2)));
    A_all(i,3) = (A13+(s13*A(i,3)));
    A_all(i,4) = (A14+(s14*A(i,4)));
    A_all(i,5) = (A15+(s15*A(i,5)));

    A_all(i,6) = (A21+(s21*A(i,6)));
    A_all(i,7) = (A22+(s22*A(i,7)));
    A_all(i,8) = (A23+(s23*A(i,8)));
    A_all(i,9) = (A24+(s24*A(i,9)));
    A_all(i,10) = (A25+(s25*A(i,10)));

    A_all(i,11) = (A31+(s31*A(i,11)));
    A_all(i,12) = (A32+(s32*A(i,12)));
    A_all(i,13) = (A33+(s33*A(i,13)));
    A_all(i,14) = (A34+(s34*A(i,14)));
    A_all(i,15) = (A35+(s35*A(i,15)));
end

%% Remove Points from BB that exceeded boundaries

for i=length(check_z4_it3):-1:1
    if check_z4_it3(i) == 1
        A_all(i,:) = [];
        mean_force(i) = [];
        A(i,:) = [];
    end
end

%% Remove points that did not track well

% thresh = 10; % Set threshold for cutoff (degrees)
% for N = 1:3 % DOF
%
% for i=length(AvgErr):-1:1
%     if AvgErr(i,N) > thresh
%         A_all(i,:) = [0 0 0 0 0 0 0 0 0 0 0 0 0 0 0];
%         mean_force(i) = 0;
%         twofreqterm(i) = [];
%         A(i,:) = [];
%     end
%

```

```

% end
% end

%% Add a point at Zero

A_all(size(A_all,1)+1,:) = [0 0 0 0 0 0 0 0 0 0 0 0 0 0 0];
mean_force(size(mean_force,1)+1,:) = 0;

%% Create a quadratic model of the parameters in A_all and the mean_force
% resulting from each of those sets of parameters.

% m = 2;
% n = 2;
% randmat = zeros(size(A_all));
% randmat(2:2,4) = ones(1,1);
% A_temp = A_all + randmat;
% A_all = [A_all; A_all + 1];
% A_all = [A_all; A_temp(m:n,:)];
% mean_force = [mean_force; mean_force(m:n)];

stats =
regstats(mean_force,A_all,'quadratic',{'beta','rsquare','yhat','tstat'});
b = stats.beta; % Model coefficients
rsquare = stats.rsquare;
yhat = stats.yhat;
tstat = stats.tstat;

count = 1; % counter to keep track of our place in b
Intercept = b(count);
count = count + 1;

% Extract the linear terms
Linear = zeros(1,numVars);
for i = 1:numVars
    Linear(1,i) = b(count);
    count = count + 1;
end

% Extract the interaction terms
Interactions = zeros(numVars);
for i = 1:numVars
    for j = (i+1):numVars
        Interactions(i,j) = b(count);
        % Note, each interaction term must be divided by two because it
        % appears in two places in the Hessian, symmetrically about the
        % diagonal.
        count = count + 1;
    end
end
%
% Interactions = Interactions + Interactions';

% Extract the squared terms
Squared = zeros(numVars);

```

```

for i = 1:numVars
    Squared(i,i) = b(count);
    count = count+1;
end

AA = Intercept;
BB = Linear;
CC = Interactions + Squared;

%% Test Surface Points with Calibrated Values

x = A_all;
f = zeros(1,length(x));
for i = 1:length(x)
    f(i) = AA + BB*x(i,:) + x(i,)*CC*x(i,);
end

TestResults_vs_2ndOrderModel = [mean_force f']

mean(abs(mean_force-f'))

rsquare

BB

% max1(k)=max(abs(BB));
% max2(k)=max(max(abs(CC)));
%
% bigcoef(k)=BB(4);

```